Numerical studies of multi-orbital Hubbard models

A Dissertation Presented for the

Doctor of Philosophy

Degree

The University of Tennessee, Knoxville

Nitin Kaushal

August 2020

To my family

Acknowledgments

I would like to express my gratitude to my advisor, Prof. Elbio Dagotto for his continuous guidance and patience. He has also persistently supported me throughout the last six years. I would like to thank the members of my committee, Prof. Adriana Moreo, Prof. Cristian Batista, and Prof. David Mandrus for their time and helpful suggestions. I would also like to thank Dr. Steven Johnston for the collaboration and suggestions in the research.

I am grateful to all my collaborators, Dr. Gonzalo Alvarez, Dr. Shaozhi Li, Dr. Guangkun, Dr. Umesh Kumar, Rahul Soni, Dr. Christopher B Bishop. I am also thankful to Dr. Anamitra Mukherjee, Dr. Alberto Nocera, Dr. Nirav Patel and Dr. Jacek Herbrych for the collaborations and nearly regular discussions on our research which enlarged my perspective on condensed matter physics. I would like to give special mention to Prof. Amit Ghosal, Dr. Anamitra Mukherjee, Prof. Elbio Dagotto and Rahul Soni for supporting me in very unfortunate period from January-2019 to January-2020, when I was stuck in India due to visa issues.

I would like to show my gratitude to Priyanka Singh, who truly has been a constant friend, supporting system, and source of balance in my life. Lastly I would like to express my everlasting thanks to my parents who have supported me to pursue my dreams.

Abstract

This thesis examines the emergence of exotic phases in multi-orbital Hubbard models due to competition between Coulomb interaction, spin-orbit coupling and kinetic energy. Exact diagonalization and numerically accurate density matrix renormalization group methods are used to study small clusters and one dimensional chains. Two dimensional lattices are solved using unrestricted real-space Hartree-Fock approximation. Novel excitonic insulators, due to condensation of spin-orbit excitons, are found in the spin-orbit coupling vs Coulomb interation phase diagrams of t_{2g}^n systems for $n = 4$ and 3.5. Moreover, the presence of a BCS-BEC crossover in the t_{2g}^4 excitonic insulator is predicted. Finally, interesting features in the dynamical spin structure factor calculated using the three-orbital Hubbard model relevant for $BaFe_2Se_3$ are discussed in detail.

Table of Contents

List of Figures

Chapter 1

Introduction

The deceptively simple looking one-orbital Hubbard model [7] has been studied by the Condensed Matter community, at a very large scale and for many years, to understand the transport and magnetic properties of the materials associated to these type of models. Both analytical and numerical technniques have been used. The study of this model received a considerable boost specially after the discovery of high temperature superconductivity in cuprates [8]. Still many ingredients are still neglected in this model but they are present in real materials such as electron-phonon and phonon-phonon interactions, etc. Remarkably, several fairly complicated properties of quasi 2D-cuprates, such as antiferromagnetism, charge stripe order, superconductivity and strange metallic behaviour are believed to emerge from the two-dimensional one-orbital Hubbard model [9] or from its closely related derivatives like the $t-J$ [10] and spin-fermion models [11, 12]. Even for the quasi two-leg ladder compounds, this model was useful because the presence of a spin-gap and superconductivity was theoretically predicted by numerical studies [13, 14] and then later superconductivity was found experimentally in the Cu-based ladder compound $Sr_xCa_{14-x}Cu_{24}O_{41}$ [15]. This is an excellent case showing how theory can arrive to correct conclusions before the experiments. It also highlights the presence of exotic properties, such as quasi d-wave superconductivity, in low-dimensional compounds. Superconductivity is usually studied in the context of two or three dimensional models.

In parallel to the struggle to understand the properties of one-orbital Hubbard models and related compounds, many transition metal oxides have shown the necessity of using multiple

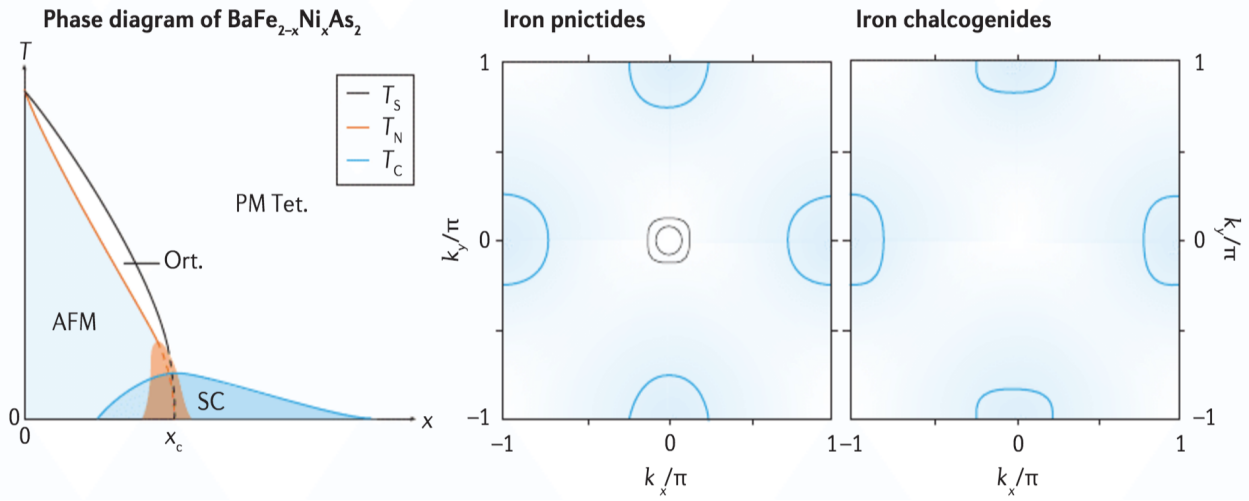

Figure 1.1: Left panel : Schematic phase diagram of $BaFe_2NiAs_2$ in the temperature (T) and chemical-substitution (x) plane. Right panel : Schematic Fermi surfaces of the iron pnictides and those of several iron-chalcogenides. These plots are reproduced from Ref. [1].

orbitals to investigate their properties, with iron-based superconductors [16, 17, 18] being a prominent example. In Fig. 1.1 the temperature vs chemical substitution phase diagram corresponding to the compound $BaFe_{2-x}Ni_xAs_2$ is shown, presenting very similar features as in the cuprates, such as the appearence of a superconducting dome by suppresing magnetism, even though the iron-based superconductors have multiple orbitals present at the Fermi level. It must be noted that even for the cuprates, to capture the charge-transfer properties properly, the p-orbitals of oxygen must be included in the theoretical calculations [19, 20].

One of the recent breakthroughs in high-Tc superconductivity is the synthesis of low dimensional iron chalcogenides (quasi two-leg ladders), such as $BaFe_2S_3$ and $BaFe_2Se_3$. Both materials are insulators at ambient conditions and have shown superconductivity under high pressure [2, 21, 22, 3]. This behavior is unusual since, unlike the cuprates, the parent compounds of iron-based superconductors are typically bad metals. It will be a reasonable assumption to consider both of these materials as a new class of iron-based superconductors. The parent compound (i.e. at ambient pressure) of $BaFe_2S_3$ has $(\pi, 0)$ magnetic order, namely spin ferromagnetic (FM) order along rungs and antiferromagnetic order (AFM) along the legs. This magnetic order resembles the generic collinear antiferromagnetic magnetic

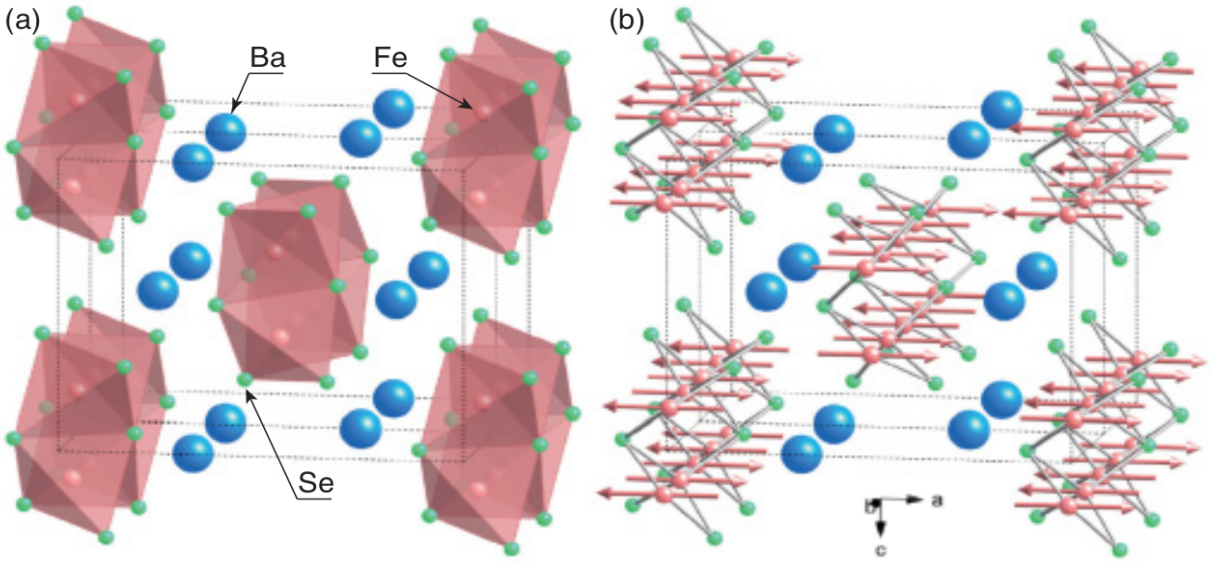

Figure 1.2: Panel (a) shows the crystal structure of $BaFe_2Se_3$. The unsual magnetic ordering is shown in panel (b) at $T = 5K$. These figures are reproduced from Ref. [2].

order present in other 2D-layered metallic iron pnictide superconductors. However, neutron scattering experiments on $BaFe_2Se_3$ have shown an even more exotic *block* magnetic ordering with 2×2 FM clusters alinged antiferromagnetically to each other. In the next section we will discuss the properties of $BaFe_2Se_3$ in detail.

1.1 Fe-ladder compound $BaFe_2Se_3$

As discussed earlier, $BaFe_2Se_3$ is a two-leg ladder compound, and its crystal structure is shown in Fig. 1.2(a). Each unit cell has two iron atoms, arranged in a two-leg ladder structure along the b direction connected by edge-sharing $FeSe_4$ tetrahedrons. The local magnetic moments on each Fe ion is $\approx 2.8\mu_B$ and they are arranged in a long-range block magnetic order as shown Fig. 1.2(b) with $T_N = 250K$. Recently, pressure induced superconductivity was observed experimentally in $BaFe_2Se_3$ [3]. The temperature vs pressure phase diagram

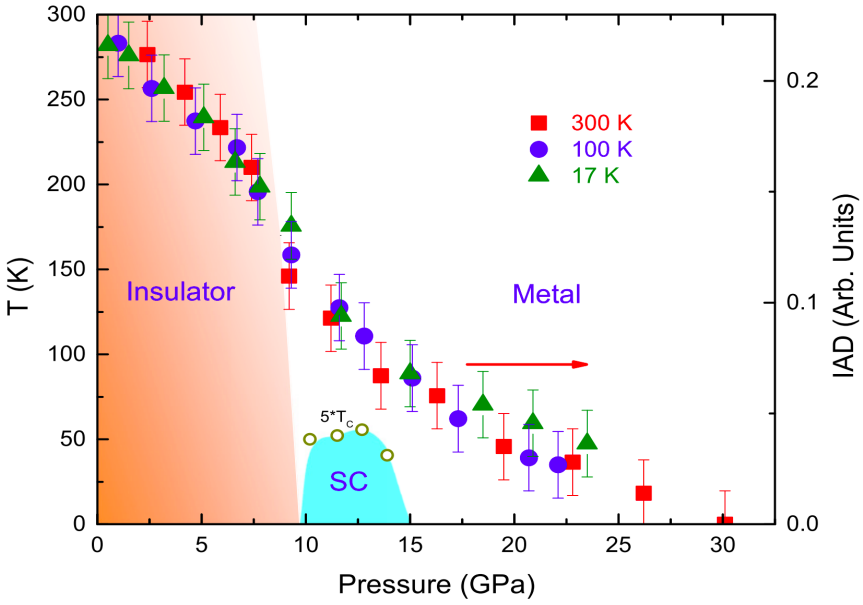

Figure 1.3: Temperature vs pressure phase dagram corresponding to $BaFe_2Se_3$. This figure is reproduced from Ref. [3].

was also mapped out, shown in Fig. 1.3. It was noticed that the local moments reduces to $\approx 1\mu_B$ as the system reaches to the superconducting state.

First-principles calculations [23] have also shown the dominance of the block magnetic state found experimentally. The band structure calculation in this magnetic state produces a gap of 0.24 eV [23]. With regards to model Hamiltonians, calculations using the five-orbital Hubbard model in the Hartree-Fock approximation have been performed [24]. By varying the Hubbard U and Hund coupling J_H, it was found that the block magnetic phase is stable in a robust portion of the phase diagram. This includes the regime with the ratio $J_H/U = 0.25$ widely believed to be realistic for these compounds. In addition, other phases not yet observed experimentally were also found to be stable upon varying the couplings, suggesting that many states are close in energy and likely competing.

It is interesting to note that DMRG studies of one-dimensional multiorbital Hubbard models relevant for $BaFe_2Se_3$ have also shown the presence of a block magnetic ordered

state, accompanied by *orbital-selective Mott phase* (OSMP) [5, 25, 26, 27]. Both Hartree-Fock and DMRG results indicates that $BaFe_2Se_3$ is in the intermediate coupling regime, instead of weak or strong coupling, where OSMP develops. Features of the orbital-selective Mott phase can be investigated experimentally by probing charge and orbital dynamics using techniques like angle-resolved photo emission spectroscopy ARPES and Resonant inelastic X-Ray scattering (RIXS). For both techniques, testable predictions have been already made using DMRG calculations [28]. Recently, inelastic neutron scattering experiments have been performed to study spin excitations on powder samples of $BaFe_2Se_3$ [4], which shows the presence of a low-energy acoustic mode and multiple high-energy optical modes, as shown in Fig. 1.4.

To examine the spin-excitations theoretically, we calculated the dynamical spin structure factor $S(q, \omega)$ (via Dynamical-DMRG technique) using our microscopic multiorbital Hubbard model in the block magnetic ordered state OSMP regime. The results are discussed in detail in Chapter 5. The main advantage of studying ladders is that the quasi-one dimensionality of these systems allows for theoretical calculations more accurate than those routinely performed for two-dimensional systems, specially because of steady growth in computational resources. This improves the back-and-forth iterative process between theory and experiments needed to understand these materials, as well as to rationalize the mechanism for the superconductivity in these multi-orbital systems [29]. However, the understanding of ladder iron selenides is still at its early stages and more work should be carried out in this context in the future.

1.2 Atomic spin-orbit coupling

In this section, we will discuss the motivation and details of spin-orbit coupling in multi-orbital Hubbard models. The presence of multiple active orbitals naturally opens a path for spin-orbit coupling to move materials into relatively new and exotic physics, especially for $4d/5d$ transition metal oxides. This is because as we move down in the periodic table the strength of the spin-orbit coupling (SOC) increases as Z^4, with Z as the atomic number, and

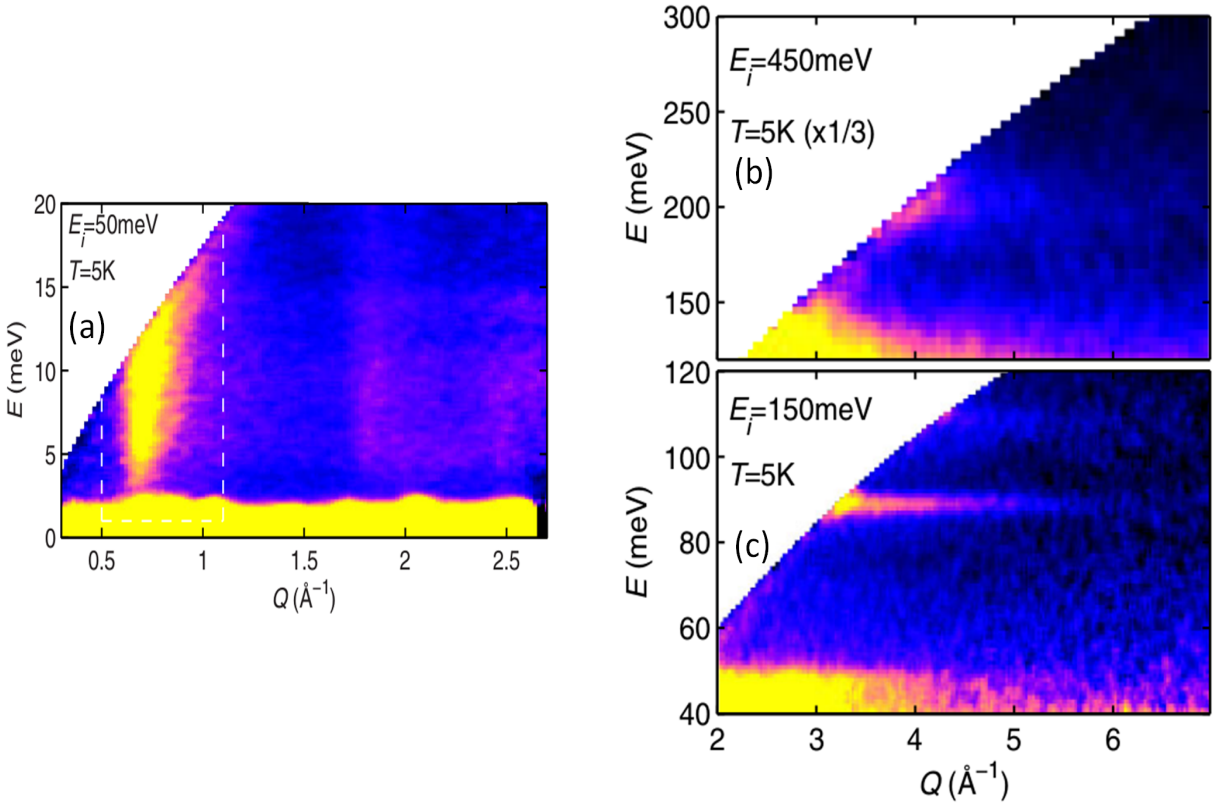

Figure 1.4: Panel (a) shows the inelastic neutron scattering low-energy spectrum for a powder sample of $BaFe_2Se_3$ at $T = 5K$. Panels (b,c) show the high-energy spectrum at the same temperature. These figures are reproduced from Ref. [4].

it can become of order 0.4 eV for some $4d$ or $5d$ materials [30]. The study of transition metal compounds, especially iridates, has attracted considerable attention in the last decade. In layered materials such as Sr_2IrO_4 and Ca_2IrO_4, involving $5d$ electrons, the Hubbard repulsion is moderate as compared to $3d$ electrons because the size of the associated wave functions is larger for the $5d$ sector [31, 32, 33, 34, 35, 36, 37, 38]. As a consequence, iridates provide an interesting playground where the Hubbard repulsion and SOC are of similar magnitudes [30].

The atomic spin-orbit coupling can be written in second quantization as follows:

$$H_{SOC} = \lambda \sum_{i,\gamma,\gamma',\sigma,\sigma'} \langle \gamma\sigma | \mathbf{L}_i \cdot \mathbf{S}_i | \gamma'\sigma' \rangle c^\dagger_{i\gamma\sigma} c_{i\gamma'\sigma'}. \tag{1.1}$$

The matrix elements $\langle\gamma\sigma|\mathbf{L}_i\cdot\mathbf{S}_i|\gamma'\sigma'\rangle$ for the d orbital (i.e. the case of transition metal oxides) can be calculated using $|xz\rangle = \frac{1}{\sqrt{2}}(-|1\rangle + |-1\rangle)$, $|yz\rangle = \frac{-i}{\sqrt{2}}(-|1\rangle - |-1\rangle)$, $|xy\rangle = \frac{-i}{\sqrt{2}}(-|-2\rangle + |2\rangle)$, $|x^2-y^2\rangle = \frac{1}{\sqrt{2}}(|-2\rangle + |2\rangle)$ and $|z^2\rangle = |0\rangle$, which leads to following values in the t_{2g} sector:

$$\langle xz,\alpha|\mathbf{L}_i\cdot\mathbf{S}_i|xy,\beta\rangle = \frac{i\lambda}{2}\sigma^x_{\alpha\beta} \tag{1.2}$$

$$\langle xy,\alpha|\mathbf{L}_i\cdot\mathbf{S}_i|yz,\beta\rangle = \frac{i\lambda}{2}\sigma^y_{\alpha\beta} \tag{1.3}$$

$$\langle yz,\alpha|\mathbf{L}_i\cdot\mathbf{S}_i|xz,\beta\rangle = \frac{i\lambda}{2}\sigma^z_{\alpha\beta} \tag{1.4}$$

It must be noted that the spin-orbit coupling and orbital angular momentum both are quenched in the e_g sector. We add Eq. 1.1 to the three-orbital Hubbard models to investigate the effect of spin-orbit coupling and Hubbard interaction at equal footing in our numerical calculations.

In the weak electron-electron correlation limit, the t_{2g} orbitals split into a total angular momentum doublet $j_{\text{eff}} = 1/2$ and a quartet $j_{\text{eff}} = 3/2$ [39] (see Appendix B.1). This simple picture, which in principle is valid only in the $j-j$ coupling limit namely when $\lambda/U >> 1$, can help to understand the physics in some real materials. For example, Sr_2IrO_4, with Ir^{4+} ions and filling $n = 5$ electrons (t_{2g}^5), due to strong spin-orbit coupling has nearly fully-filled $j_{\text{eff}} = 3/2$ and half-filled $j_{\text{eff}} = 1/2$ bands. This is a celebrated material due to the presence of long-range antiferromagnetic ordering in quasi two-dimensional layers, as in the superconducting cuprates [39]. Recent resonant inelastic X-ray scattering (RIXS) experiments on Sr_2IrO_4 have reported excitons as an excitation at approximately $0.5-0.6$ eV [40, 41, 42]. RIXS experiments on one-dimensional stripes of Sr_2IrO_4 also indicated excitons at nearly the same energy [43]. These excitons are present in spin-orbit entangled states, hence known as *spin-orbit excitons*.

More recently, interest also developed in other transition metal oxides having $(t_{2g})^4$ ions with octahedron or distorted octahedron crystal-field splittings [39, 44, 45, 46, 47, 48, 49, 50, 51, 52, 53, 54, 55, 56, 57]. When the Hubbard U and Hund J_H couplings are large, it is expected that the system develops $S = 1$ states, while increasing the SOC λ should lead to states with an effective angular momentum zero (see Appendix B.1). Thus, the next obvious

step is to understand the phases in these systems in the presence of hopping, namely with the full Hamiltonian. Experiments on these materials have shown contrasting results thus far. For example, the magnetic properties of Sr_2YIrO_6 [52] suggest exotic antiferromagnetic (AFM) ordering coming from excitonic condensation, while other experiments [55] favor a nonmagnetic ground state. Double perovskites such as Ba_2YIrO_6 are also challenging to study [53, 54]. This situation demands a comprehensive and accurate theoretical study of the combined effects of U and λ in the $(t_{2g})^4$ sector. In Chapters 2 and 3, we will discuss the t_{2g}^4 case in detail. In Chapter 4, we will also show the first numerical evidence of a novel excitonic condensate phase accompanied with block magnetic ordering, driven by atomic spin-orbit coupling in the fractionaly filled three-orbital Hubbard model.

Alongside the iridates, progress has been made on iron-based superconductors in recent years [58, 59, 60]. While initially the expectation was that weak coupling approximations and Fermi surface nesting between hole and electron pockets could be sufficient to understand these compounds, recent efforts have highlighted the importance of Hubbard interactions of at least intermediate value between weak and strong coupling [18]. For example, there are materials that do not have hole pockets, yet they still superconduct [61]. Moreover, via angle-resolved photoemission spectroscopy (ARPES) it has been argued [62] that a SOC of order 20 meV, much smaller than in iridates, may still influence the features of the Fermi level and thus affect superconducting properties.

In summary, in this PhD thesis we will focus on the study of multiorbital Hubbard models, with and without spin-orbit coupling. We will study a variety of exotic magnetic new states, particularly those of the block variety. With spin-orbit coupling included a excitonic condensate phase will be studied, with concomitant magnetic order. All these new developments are possible by using reliable computational techniques that go well beyond crude mean field or diagrammatic approximations, and allow us to trust the results, focusing primarily on the properties of the new states and possible realizations in real materials.

Chapter 2

Density matrix renormalization group study of a three-orbital Hubbard model with spin-orbit coupling in one dimension

2.1 Introduction

In this Chapter we employed numerically exact computational techniques to study a model of interacting electrons in the simultaneous presence of nonzero U, λ, and J_H. In particular, we will analyze a multiorbital model defined on a one dimensional geometry.

Our study is conceptually generic but for simplicity will focus on a previously used three-orbital Hubbard model with bands that resemble layered iron superconductors, containing hole and electron pockets. In the absence of spin-orbit coupling, this model was studied before via the Density Matrix Renormalization Group (DMRG) technique and a rich phase diagram was observed, including an orbital-selective Mott phase (OSMP), where two orbitals are partially filled and thus they are metallic, while the other orbital is half-filled and behaves like a Mott insulator [5, 25, 26, 27]. Our main focus is to analyze how this phase diagram

is modified after including atomic spin-orbit effects. The generic analysis reported here is important for three reasons:

(i) By constructing the phase diagram in one dimension including the combined effects of the Hubbard interaction U as well as the spin-orbit coupling λ with a robust computational technique, we can address the accuracy of previous approximate studies performed in higher dimensions. For example, recently Dynamical Mean Field Theory (DMFT) calculations were performed [63, 64, 65] on a three-orbital Hubbard model with degenerate t_{2g} orbitals and four electrons per site. Their analysis showed the presence in the phase diagram of an interesting excitonic condensate (to be described below) and a non-magnetic insulator with zero effective total angular momentum. Our accurate numerical results on chains using non-cubic t_{2g} bands confirm most of the DMFT predictions, including the existence of an excitonic condensate, thus suggesting that studies in different dimensions may lead to qualitatively similar results.

(ii) There are real materials with quasi-one dimensional characteristics where spin-orbit effects are expected to be important. For example, recently, single-crystals of $Ba_5AlIr_2O_{11}$ that contain dimer chains were experimentally studied [66]. This is a Mott insulator with a subtle structural transition at $T_S = 210$ K and a magnetic transition at much lower temperatures. A novel and intriguing magnetic state was reported, that is neither $S = 3/2$ nor $J = 1/2$ but instead intermediate between them. Other examples of spin-chain $4d$- and $5d$-based compounds are $Sr_5Rh_4O_{12}$, $Ca_5Ir_3O_{12}$, and Ca_4IrO_6 [67]. These are insulators characterized by partial AFM order at low temperatures. Sr_3CuIrO_6 is also a quasi-one dimensional material where IrO_6 octahedra are linked by spin-1/2 Cu ions along one direction [68]. In this compound intersite hopping is suppressed by the geometry of the system locating Sr_3CuIrO_6 in the strongly localized regime, with a noncubic crystal-field comparable in strength to the spin-orbit coupling. Other examples of interesting one dimensional systems where our results may be of relevance are $BaIrO_3$ [69, 70], $CaIrO_3$ [71], Sr_3MIrO_6 (M = Ni, Cu, Zn) [72], lead iodides [73], and alkaline-earth palladates [74].

(iii) As already explained, recent ARPES measurements reported a sizable spin-orbit splitting in all the main members of the iron-based superconductors family [62]. This spin-orbit coupling affects the low-energy electronic structure and, thus, may have implications for superconductivity. While the magnitude of λ for iron pnictides and chalcogenides is

substantially smaller than for iridates, it is conceptually interesting to investigate what phases could be found if members of the iron superconductors family would have a larger λ.

Spin-orbit effects are often discarded in the literature, usually by hand waving arguments, and the models are largely simplified as a result. But realistic detailed studies involving spin-orbit couplings comparable to other small energies of interest (such as the magnetic superexchange J) are lacking. Moreover, it is experimentally challenging to determine the precise magnitude of spin-orbit contributions. On the *ab-initio* side of theory, often these spin-orbit contributions are not considered if expected to be smaller than systematic errors in the approach, typically of order 0.5 eV. As a consequence, an evaluation of the effects of spin-orbit corrections on the results of specific models could determine if refined *ab-initio* or measurements are required.

The organization of this chapter is as follows. In Sec. 2.2, the model used and the computational methodology are presented. In Sec. 2.3, the main results, particularly the phase diagram varying U and λ, are shown. In particular, we address three regimes: weak, intermediate, and strong Hubbard interaction U. In Sec. 2.4, we discuss the results and present our conclusions.

2.2 Model and Method

In this study we have used a one dimensional three-orbital Hubbard model. The Hamiltonian contains a tight-binding term, an on-site Hubbard interaction, and a spin-orbit coupling: $H = H_K + H_{\rm int} + H_{SOC}$. The electronic kinetic energy component is

$$H_K = -\sum_{i,\sigma,\gamma,\gamma'} t_{\gamma\gamma'}(c^{\dagger}_{i\sigma\gamma}c_{i+1\sigma\gamma'} + \text{h.c.}) + \sum_{i,\sigma,\gamma}\Delta_{\gamma}n_{i\sigma\gamma}. \tag{2.1}$$

The hopping amplitudes $t_{\gamma\gamma'}$ are defined in orbital space and they connect the nearest-neighbor lattice sites i and $i+1$, with the specific values (in eV units) $t_{00} = t_{11} = -0.5$, $t_{22} = -0.15$, and $t_{\gamma\gamma'} = 0$ if $\gamma \neq \gamma^{'}$. The total bandwidth is $W = 4.33\,|t_{00}|$. The above mentioned 0, 1, and 2 orbitals can be visualized as representing the canonical d_{yz}, d_{xz}, and d_{xy} orbitals, respectively. The orbital-dependent crystal-field splitting is denoted by Δ_{γ}, with

$\Delta_0 = -0.05$, $\Delta_1 = -0.05$, and $\Delta_2 = 0.8$ (also in eV units). The band structure of this model qualitatively resembles that of iron-based superconductors, i.e., hole and electron pockets centered at wavevectors $q = 0$ and π, respectively. A very similar band structure was used in our previous studies for a three-orbital Hubbard model [5, 25, 26, 27], where OSMP was analyzed. This previous work was carried out in the absence of spin-orbit interactions, and our main focus is to analyze the effects of this additional term in the model. The Hubbard portion of the Hamiltonian includes the following onsite components in the standard notation

$$H_{\text{int}} = U \sum_{i,\gamma} n_{i\uparrow\gamma} n_{i\downarrow\gamma} + (U' - J_H/2) \sum_{i,\gamma<\gamma'} n_{i\gamma} n_{i\gamma'} - 2J_H \sum_{i,\gamma<\gamma'} \mathbf{S}_{i\gamma} \cdot \mathbf{S}_{i\gamma'} + J_H \sum_{i,\gamma<\gamma'} \left(P^\dagger_{i\gamma} P_{i\gamma'} + \text{h.c.} \right). \quad (2.2)$$

In this expression the operator $\mathbf{S}_{i\gamma} = \frac{1}{2} \sum_{\alpha,\beta} c^\dagger_{i\alpha\gamma} \boldsymbol{\sigma}_{\alpha\beta} c_{i\beta\gamma}$ is the total spin at orbital γ and lattice site i, and $n_{i\gamma}$ is the electronic density at each orbital. The first two terms describe the intra- and inter-orbital electronic repulsion, respectively. The third term contains the Hund coupling that favors the ferromagnetic alignment of the spins at different orbitals; the fourth term is the pair hopping with $P_{i\gamma} = c_{i\downarrow\gamma} c_{i\uparrow\gamma}$ as the pair operator. We use the standard relation $U' = U - 2J_H$ based on rotational invariance, and we fix $J_H = U/4$ because this value is widely accepted in iron superconductors to be realistic [18]. For these reasons, only U and λ are free parameters in our study. Future work can analyze in more detail the influence of varying the Hund coupling as well as other parameters in the model.

The SOC term is

$$H_{\text{SOC}} = \lambda \sum_{i,\gamma,\gamma',\sigma,\sigma'} \langle \gamma | \mathbf{L}_i | \gamma' \rangle \cdot \langle \sigma | \mathbf{S}_i | \sigma' \rangle c^\dagger_{i\sigma\gamma} c_{i\sigma'\gamma'} \,, \quad (2.3)$$

where λ is the SOC coupling strength, as already explained. Because of the presence of the SOC term the total spin along the z-axis, S_z, is no longer a good quantum number; hence, we cannot target specific S_z sectors in our numerical DMRG calculation. To reduce the computational cost, we have instead selected the parameters contained in H_K such that $[H, J_z^{eff}] = 0$ where $\mathbf{J}^{eff} = \sum_i (\mathbf{S}_i - \mathbf{L}_i)$. Note that for arbitrary values of the hopping

amplitudes and crystal-fields, J_z^{eff} is also not a good quantum number as discussed in the Appendix A.1. We then target subspaces with a fixed total $J_z^{eff} = \sum_i (J_z^{eff})_i$ for the system. The SOC term is diagonalized in the j^{eff} basis, where j^{eff} is the quantum number associated with $\mathbf{J}^{eff}$ (to avoid complications in the notation, as when j^{eff} should appear as subindex, sometimes this quantum number will be denoted simply by j). m is the projection along the z-axis namely the quantum number of J_z^{eff} . The fact that the good quantum numbers for the SOC term are associated with the effective angular momentum, instead of the total angular momentum ($\mathbf{J} = \mathbf{S} + \mathbf{L}$), is a consequence of the "$t_{2g} - p$" equivalence discussed in [75]. The "t_{2g} subspace" of the d-orbitals ($l = 2$ for a complete d orbital set) has $\langle \mathbf{L}^2 \rangle$=2 for a single electron, hence "t_{2g}" is isomorphic to the $l = 1$ space (i.e., the p-orbitals) under the following mapping: $|1\rangle_p \equiv -i|-1\rangle_d$, $|-1\rangle_p \equiv i|1\rangle_d$, $|0\rangle_p \equiv |xy\rangle_d$, and $\mathbf{L}^{l=1} \equiv$ -$\mathbf{L}^{t_{2g}}$.

The transformation between the t_{2g} orbitals and the j^{eff} basis is given by (dropping site i index)

$$\begin{bmatrix} a_{\frac{3}{2},\frac{3s}{2}} \\ a_{\frac{3}{2},-\frac{s}{2}} \\ a_{\frac{1}{2},-\frac{s}{2}} \end{bmatrix} = \begin{bmatrix} \frac{is}{\sqrt{2}} & \frac{1}{\sqrt{2}} & 0 \\ \frac{s}{\sqrt{6}} & \frac{i}{\sqrt{6}} & \frac{2}{\sqrt{6}} \\ \frac{-s}{\sqrt{3}} & \frac{-i}{\sqrt{3}} & \frac{1}{\sqrt{3}} \end{bmatrix} \begin{bmatrix} c_{\sigma yz} \\ c_{\sigma xz} \\ c_{\bar{\sigma} xy} \end{bmatrix}, \tag{2.4}$$

where s is $1(-1)$ when σ is $\uparrow$ ($\downarrow$) and $\bar{\sigma} = -\sigma$. The H_{SOC} term in the j^{eff} basis becomes

$$\begin{aligned} H_{\text{SOC}} &= \sum_i \frac{\lambda}{2} (-a^\dagger_{i,\frac{3}{2},\frac{3}{2}} a_{i,\frac{3}{2},\frac{3}{2}} - a^\dagger_{i,\frac{3}{2},-\frac{1}{2}} a_{i,\frac{3}{2},-\frac{1}{2}} \\ &- a^\dagger_{i,\frac{3}{2},-\frac{3}{2}} a_{i,\frac{3}{2},-\frac{3}{2}} - a^\dagger_{i,\frac{3}{2},\frac{1}{2}} a_{i,\frac{3}{2},\frac{1}{2}} \\ &+ 2a^\dagger_{i,\frac{1}{2},\frac{1}{2}} a_{i,\frac{1}{2},\frac{1}{2}} + 2a^\dagger_{i,\frac{1}{2},-\frac{1}{2}} a_{i,\frac{1}{2},-\frac{1}{2}}) . \end{aligned} \tag{2.5}$$

The SOC component commutes with $(\mathbf{J}^{eff})^2$. As a consequence, in the H_{SOC} term there is four(two)-fold degeneracy in the $j^{eff} = 3/2$ ($1/2$) bands. However, the four-fold degeneracy of the $j^{eff} = 3/2$ sector breaks into a pair of two-fold Kramer degeneracies due to the presence of the non-cubic t_{2g}-band structure used in our model. This can be understood by analyzing

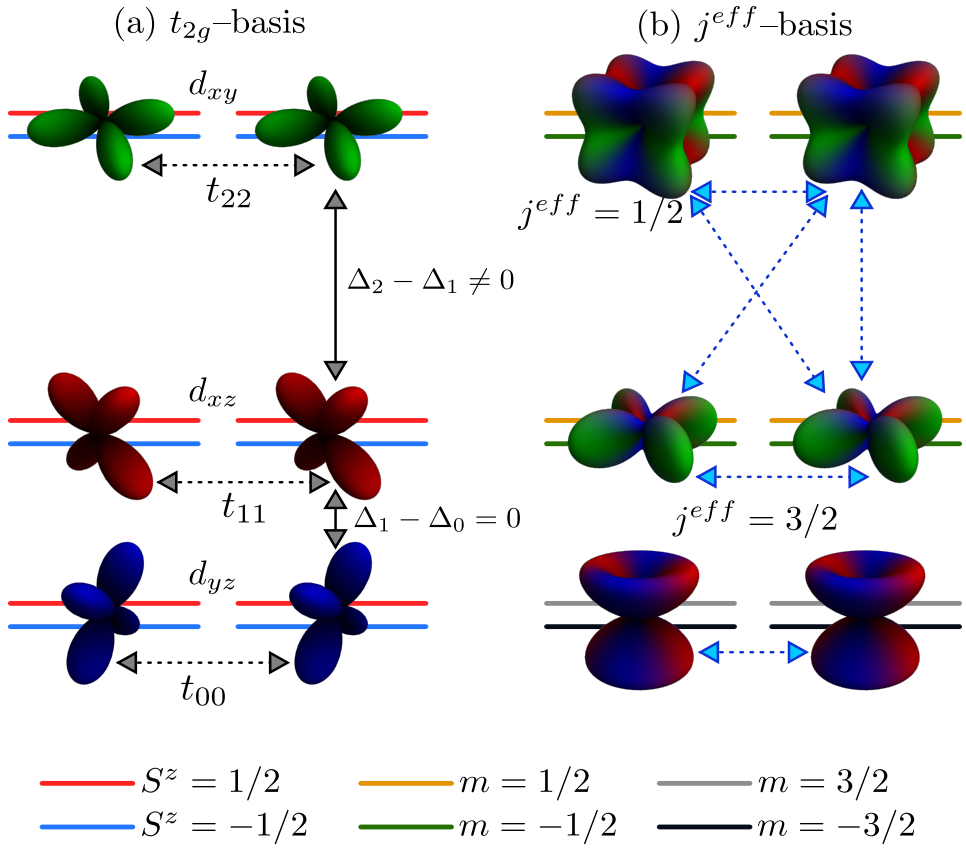

Figure 2.1: In panel (a) we show the connections between t_{2g} orbitals using dashed lines, while in panel (b) the dashed lines represent the non-zero connections present in the (j^{eff}, m) basis if we use the proper hopping and crystal-field parameters satisfying the constraints described in the Appendix A.1.

the H_K term in the (j^{eff}, m) basis. In Fig. 2.1 we show explicitly the connections contained in H_K between the t_{2g} states and the corresponding connections between (j^{eff}, m) states, after imposing the constraints on the hopping and crystal-field parameters (see Appendix A.1). We have noticed that the non-cubic nature of the t_{2g} states (i.e., the non-degeneracy of the d_{xy} with the $\{d_{xz}, d_{yz}\}$ states, consequence of the tetragonal type t_{2g} bands) leads to hybridization between $(j^{eff} = 1/2, m = \pm 1/2)$ and $(j^{eff} = 3/2, m = \pm 1/2)$ states. This hybridization breaks the four-fold degeneracy of the $j^{eff} = 3/2$ states and also leads to the formation of new bands in which $H_K + H_{SOC}$ is diagonalized.

After using the inverse transformation of Eq. (2.4) in the tight-binding term, we diagonalized the $H_K + H_{SOC}$ together to obtain the following bands

$$H_K + H_{SOC} = \sum_{k,\alpha,s} E_\alpha(k) \tilde{a}^\dagger_{k,\alpha,s} \tilde{a}_{k,\alpha,s} \,, \tag{2.6}$$

where $s \in \{1, -1\}$ and $\alpha \in \{0, 1, 2\}$. Here α is the band index, and the relation between $\tilde{a}^\dagger_{k,\alpha,s}$ and $a_{k,j,m}$ is shown in the Appendix A.2. The dispersion relations for the bands are $E_0(k) = \epsilon_0(k) - \frac{\lambda}{2}$, and $E_\alpha(k) = \frac{1}{2}[\epsilon_2(k) + \epsilon_1(k) + \frac{\lambda}{2} + (-1)^\alpha \sqrt{(\epsilon_2(k) - \epsilon_1(k) - \frac{\lambda}{2})^2 + 2\lambda^2}]$ for $\alpha \in \{1, 2\}$; where $\epsilon_\alpha(k) = -2t_{\alpha\alpha}\cos(k) + \Delta_\alpha$ for $\alpha \in \{0, 1, 2\}$. At $\lambda = 0$, the bands 0, 1, and 2 reduce to the standard bands of the d_{yz}, d_{xz}, and d_{xy} orbitals, respectively. For $\lambda/W \gg 1$, the bands 1 and 2 reduce to the $(j^{eff} = 1/2, m = \pm 1/2)$ and $(3/2, \pm 1/2)$ states, respectively, and $n_{3/2,\pm 3/2} = \tilde{n}_{0\pm 1}$ for any λ. The above described non-interacting portion of the Hamiltonian is useful to understand the effect of spin-orbit coupling in the small U/W region of the phase diagram, as discussed below.

Our many-body calculations are performed using the DMRG technique [76, 77, 78] applied to one dimensional chains of various lengths, such as $L = 8$, 16, 24, and 32 sites. We used up to 600 states for the DMRG process and have maintained a truncation error below 10^{-14} throughout the finite algorithm sweeps. In the latter, we performed 10 to 15 full sweeps to gain convergence depending on the system size. We studied the presence of various phases by calculating expectation values of $n_{i\alpha}$, n_{ijm}, $\mathbf{S}_i^2$, $\mathbf{L}_i^2$, $(\mathbf{J}^{eff})_i^2$, the canonical spin structure factor $S(q)$, and the exciton pair-pair correlation $\langle \Delta^{\dagger\tilde{jm}}_{jm}(i) \Delta^{\tilde{jm}}_{jm}(i') \rangle$ (defined in III.B).

2.3 Results

The main result of this work, presented in Fig. 2.2, is the phase diagram of the three-orbital Hubbard model analyzed here, varying U and λ in units of the bandwidth W at a fixed electronic density of four electrons per site on average. In the following subsections, details are provided for the three special cases of weak, intermediate, and strong Hubbard

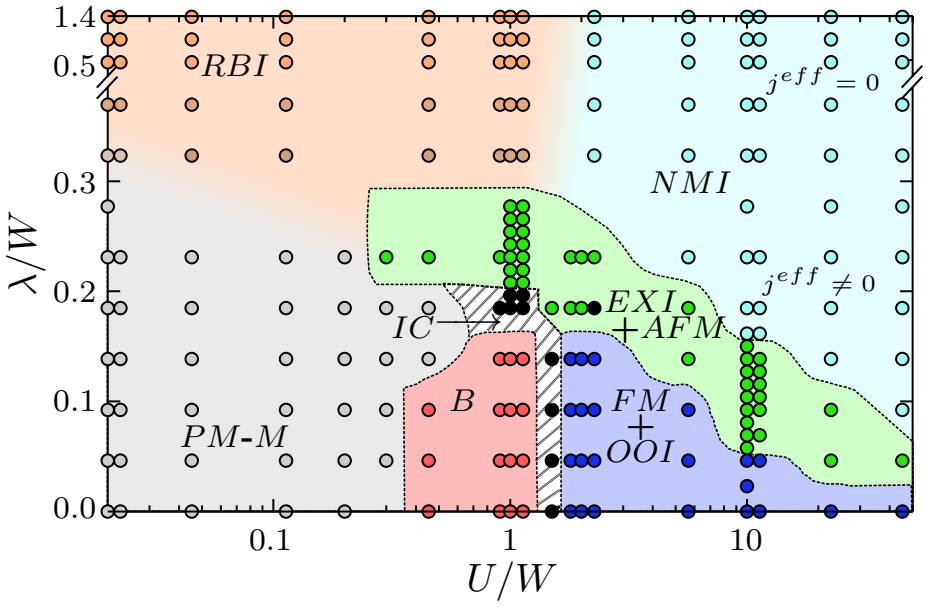

Figure 2.2: λ-U phase diagram (note the log scale in U/W-axis). RBI, PM-M, B, FM, OO, IC, EXI, AFM, and NMI stands for relativistic band insulator, paramagnetic metal, block phase, ferromagnetic, orbital ordering, incommensurate, excitonic insulator, antiferromagnetic, and nonmagnetic insulator, respectively. Lines separating phases are guides to the eyes. The actual small circles indicate specific values of data points that were investigated with DMRG. Their high density indicates that this effort has been computationally demanding.

U coupling. Also note that our study is in one dimension and for this reason when we write that at some values of U and λ we are at a phase with some particular characteristics, this has to be interpreted in the sense of dominant power-law decaying correlations as opposed to true long-range order.

2.3.1 Paramagnetic Metal and Relativistic Band Insulator (Weak Coupling)

First, we will briefly discuss the small U region, i.e., the weak coupling limit. This regime can be understood by analyzing the non-interacting limit using Eq. (2.6). Varying the strength of the spin-orbit coupling λ at $U/W = 0$ the exact band structure is shown in Fig. 2.3(a,b,c). From this analysis we expect the presence of a trivial paramagnetic metal (PM-M) at small

λ which transforms into the relativistic band insulator (RBI) regime by increasing λ. At $U = 0$, for four electrons per site, we can use the condition $E_2(k = \pi) = E_1(0)$ to calculate analytically the critical spin-orbit coupling strength λ_c for which a gap opens:

$$\lambda_c(U=0) = \frac{2t_{11}t_{22}(\Delta_2 - \Delta_1) + 2(t_{11}+t_{22})\sqrt{t_{11}t_{22}(4t_{11}t_{22} + 8(t_{11}+t_{22})^2 - 2(\Delta_2-\Delta_1)^2)}}{2(t_{11}+t_{22})^2 + t_{11}t_{22}}. \tag{2.7}$$

The value of λ_c/W for our specific hopping parameters and crystal-field splittings is $\simeq 0.33$. The state $(j^{eff} = 3/2, m = \pm 3/2)$ moves below the Fermi level before λ approaches λ_c as $(j^{eff} = 3/2, m = \pm 3/2)$ does not hybridize with any other state. For the $U \neq 0$ case, but still small, λ_c can be different from $\lambda_c(U = 0)$. We suspect λ_c decreases monotonically as U increases because at intermediate U the excitonic insulator regime develops (see Sec. III.B) for λ lower than $\lambda_c(U = 0)$, and this Bardeen-Cooper-Schrieffer (BCS) limit of the excitonic insulator (EXI) regime (discussed in next Section) at intermediate U should be present near the semimetal-semiconductor transition as discussed before [79, 80, 81]. The decrease in λ_c is a result of renormalization of bands due to correlation effects, which enhances the effect of spin-orbit coupling, as discussed in [82]. In Fig. 2.3(d), we show the occupation of the (j^{eff}, m) bands (n_{jm} are the respective densities) varying λ/W at a fixed $U/W = 0.02$, displaying a smooth crossover from paramagnetic metal to band insulator. At large λ the $j^{eff} = 3/2$ bands are completely filled, while the j^{eff}=1/2 band is nearly empty at $\lambda/W =$ 1.0 and its population continues decreasing as λ is further increased.

In contrast to previous DMFT studies performed for three degenerate bands [63, 64], the four-fold degeneracy of the $j^{eff} = 3/2$ bands is here explicitly broken due to the hybridization between the $(3/2, \pm 1/2)$ and $(1/2, \pm 1/2)$ states. This is a consequence of a non-cubic crystal-field splitting and specific hopping parameters to resemble iron-based superconductors, as explained before. We also observed the above mentioned splitting in the intermediate and strong Hubbard coupling limits, thus, this effect propagates into the interacting region. It is important to mention here that due to the hybridization of our model, in the RBI regime the $j^{eff} = 1/2$ state can have a non-zero occupation because it can have non-zero weight

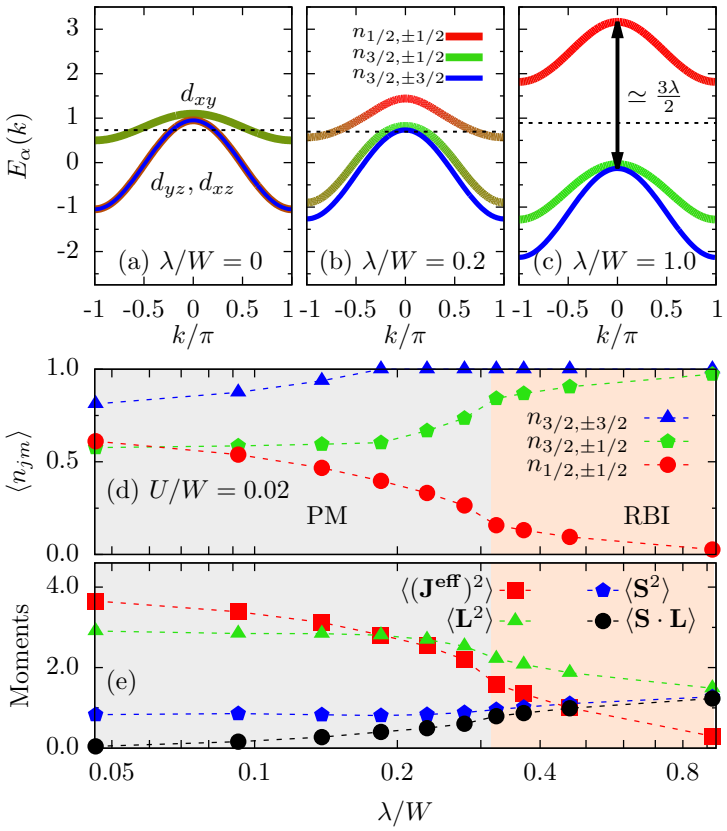

Figure 2.3: Panel (a) shows the non-interacting bands of our model at $\lambda/W = 0.0$. As explained in the text, the almost fully populated bands are degenerate and superimposed. In (b) and (c), we show the bands at $\lambda/W = 0.2$ and 1.0, respectively. Panel (c) displays a clear opening of a gap, i.e., the system becomes a band insulator. Colors are decided depending on the relative contributions from the three (j^{eff}, m) bands, with the pure cases shown in the legend of panel (c). Panel (d) contains the occupation numbers in the (j^{eff}, m) basis, while panel (e) has the local magnetic moments strengths (see legend) as well as $\langle \mathbf{S} \cdot \mathbf{L} \rangle$, all at $U/W = 0.02$. Calculations for panels (d) and (e) were performed with DMRG using a $L = 16$ chain, while panels (a,b,c) are from exact analytical formulas.

in the band below the Fermi surface. In other words, due to the hybridization between the $(3/2, \pm 1/2)$ and $(1/2, \pm 1/2)$ states, the basis where $H_K + H_{SOC}$ is diagonalized corresponds to $\tilde{a}_{k,\alpha,s}$, not $a_{k,j,m}$. As a consequence, in the lower portion of the RBI region in the phase diagram we have a finite occupation of the $(1/2, \pm 1/2)$ states coexisting with a sharp band insulator gap at the Fermi level. Only as the spin-orbit coupling continues increasing is

that $\tilde{a}_{k,\alpha,s}$ reduces asymptotically to $a_{k,j,m}$, and we reach zero occupation of the $(1/2, \pm 1/2)$ states.

Note that a similar splitting between the $j^{eff} = 3/2$, $m = \pm 1/2$ and $j^{eff} = 3/2$, m=$\pm 3/2$ bands of nearly 0.7 eV has also been observed in the $(t_{2g})^5$ perovskite $CaIrO_3$ [71] as a result of the presence of a non-cubic crystal-field, although our study is not directly related to this material.

Figure 2.3(e) shows the local moments $\langle (\mathbf{J}^{eff})^2 \rangle$, $\langle \mathbf{L}^2 \rangle$, and $\langle \mathbf{S}^2 \rangle$, as well as $\langle \mathbf{S} \cdot \mathbf{L} \rangle$. Similarly to the non-interacting case, at U/W=0.02, the moments $\langle \mathbf{L}^2 \rangle$, $\langle \mathbf{S}^2 \rangle$, and $\langle \mathbf{S} \cdot \mathbf{L} \rangle$ converge to 4/3 while $\langle (\mathbf{J}^{eff})^2 \rangle$ tends to 0 for large spin-orbit coupling (this can be checked by using the atomic state $a^\dagger_{\frac{3}{2},\frac{3}{2}} a^\dagger_{\frac{3}{2},-\frac{3}{2}} a^\dagger_{\frac{3}{2},\frac{1}{2}} a^\dagger_{\frac{3}{2},-\frac{1}{2}} |0\rangle$, which is the ground state of the H_{SOC} term).

2.3.2 Excitonic Insulator and Orbital Selective Mott Phase (Intermediate Coupling)

In this subsection we will discuss the results obtained at intermediate Hubbard interaction. This region is difficult and it cannot be treated perturbatively, thus numerical exact studies via the DMRG method are important. In this regime we have found several interesting phases such as the OSMP, EXI, incommensurate phase, and at large λ/W we again found the RBI of weak coupling. In Fig. 2.4, we present results obtained at $U/W = 1.0$. At small λ, we reproduced the OSMP regime with a magnetic Block arrangement of the spins (↑↑↓↓↑↑) [5, 25, 26, 27]. The presence of OSMP features is confirmed by measuring the occupation of the t_{2g} states: in this regime the d_{xy} orbital has occupation very close to 1, while $d_{xz(yz)}$ has occupation nearly 1.5 (see Appendix A.3). The spin structure factor $S(q)$ and the real-space spin-spin correlations are shown in Fig. 2.5(a,c) at λ/W=0.046 providing evidence for the Block magnetic order.

Figure 2.4(a) shows the occupation number in the (j^{eff}, m) states corresponding to U/W=1.0 at different λ's. As in the case of weak coupling, here the system also converges to a band insulator at sufficiently large spin-orbit coupling as the $j^{eff} = 3/2$ state is completely filled and $j^{eff} = 1/2$ becomes empty. In the strength of the magnetic moments

we have noticed a clear difference between the intermediate and weak coupling regimes, as shown Fig. 2.4(c). We found $\langle \mathbf{S}^2 \rangle = 2$ in the OSMP and in the incommensurate phase. However, this quantity is reduced after entering in the EXI phase, and at the same time $\langle \mathbf{L}^2 \rangle$ increases. We also noticed that for any Hubbard interaction in the limit of sufficiently large λ, $\langle \mathbf{S}^2 \rangle = \langle \mathbf{L}^2 \rangle = \langle \mathbf{S} \cdot \mathbf{L} \rangle$ which means $\mathbf{S}$ and $\mathbf{L}$ become parallel to each other. As a consequence, $\langle (\mathbf{J}^{eff})^2 \rangle = \langle \mathbf{S}^2 \rangle + \langle \mathbf{L}^2 \rangle - 2\langle \mathbf{S} \cdot \mathbf{L} \rangle$ converges to 0.

To identify the EXI phase, we calculated a pair-pair correlation function (note, here "pair" denotes an *electron-hole* pair), i.e., $\langle \Delta^{\dagger \tilde{j}m}_{jm}(i) \Delta^{\tilde{j}m}_{jm}(i') \rangle$, where $\Delta^{\tilde{j}m}_{jm}(i) = a^{\dagger}_{i\tilde{j}m} a_{ijm}$ (here we fixed $j = 1/2$ and $\tilde{j} = 3/2$). This operator was already introduced in previous literature [63, 64]. In our DMRG calculations, and in agreement with [63], we noticed that in the EXI phase the correlation $\langle \Delta^{\dagger \tilde{j}m}_{jm}(i) \Delta^{\tilde{j}m}_{jm}(i') \rangle$ develops staggered ordering, justifying the staggered sign used below. In Fig. 2.4(b), we show the associated correlations summed over all distances (with $j = 1/2$ and $\tilde{j} = 3/2$),

$$\Delta_m = \frac{1}{L^2} \sum_{|i-i'|>0} (-1)^{|i-i'|} \langle \Delta^{\dagger \tilde{j}m}_{jm}(i) \Delta^{\tilde{j}m}_{jm}(i') \rangle \, . \tag{2.8}$$

Then Δ_m is a measure of the staggered pair-pair correlations associated with the EXI state.

Intuitively, in the EXI phase we have hole-electron pairs involving the $(j^{eff} = 3/2, \pm 1/2)$ and $(1/2, \pm 1/2)$ manifolds. In the absence of direct hopping between the bands, there is a conservation of the number of electrons in each band. A nonzero expectation value for $\Delta^{\tilde{j}m}_{jm}(i)$ (which becomes an order parameter for this case) amounts to a spontaneous symmetry breaking of the $U(1)$ symmetry that corresponds to the relative phase of the bands in which the electron-hole pair forms [83]. However, because we are using non-cubic bands with a crystal-field splitting, this symmetry is explicitly broken in our Hamiltonian, namely in the tight-binding term transformed to the "a" basis there is a direct hopping between the $(3/2, \pm 1/2)$ and $(1/2, \pm 1/2)$ bands. Thus, it is somewhat surprising that the expectation values used in our work (like Δ_m) still behave in practice similarly as the true

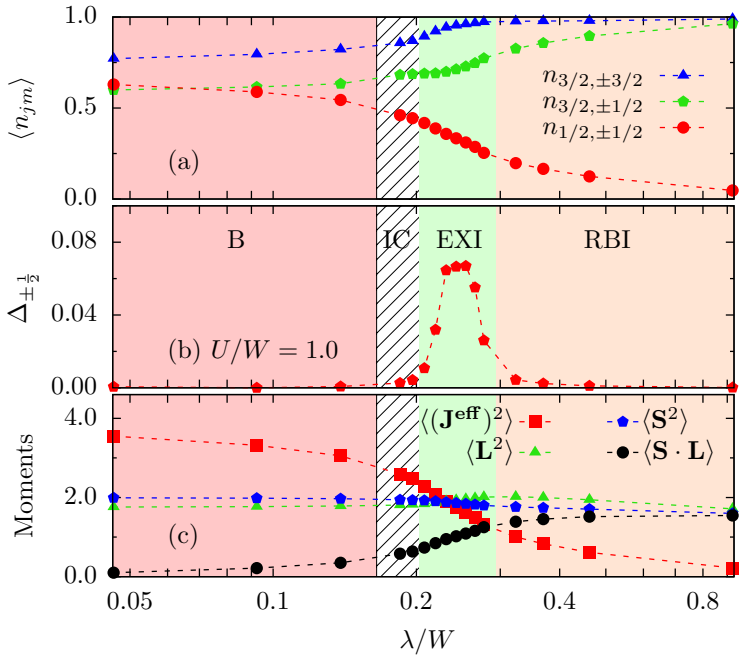

Figure 2.4: DMRG results obtained at $U/W = 1$ (intermediate coupling) and using a $L = 16$ system. Panel (a) shows occupation number in the (j^{eff}, m) bands while (b) shows the excitonic parameter Δ_m defined in Eq.(8) varying λ/W. Panel (c) shows the three local moment strengths as well as $\langle \mathbf{S.L} \rangle$.

order parameter used in [63, 64], namely it is robust in the EXI phase and very small in other phases [see Fig. 2.4(b)].

We also found that the staggered excitonic condensate is always present in combination with AFM spin ordering, as deduced from the spin structure factor $S(q)$ and the real-space spin-spin correlations presented in Fig. 2.5(b,d) at $\lambda/W = 0.23$. We also carried out finite-size scaling of $S(q)$ for system sizes $L = 8$, 16 , 24, and 32 at $\lambda/W = 0.046$ and 0.23. We noticed a fast growth in the peak value at $q = \pi$ for $\lambda/W = 0.23$, indicating that spin antiferromagnetism and excitonic order are linked together. This aspect of stabilizing antiferromagnetism in an EXI phase due to robust Hund's coupling, as used by us, was discussed before in [84]. Exploring the effects of varying the Hund's coupling in our model can be carried out in future work.

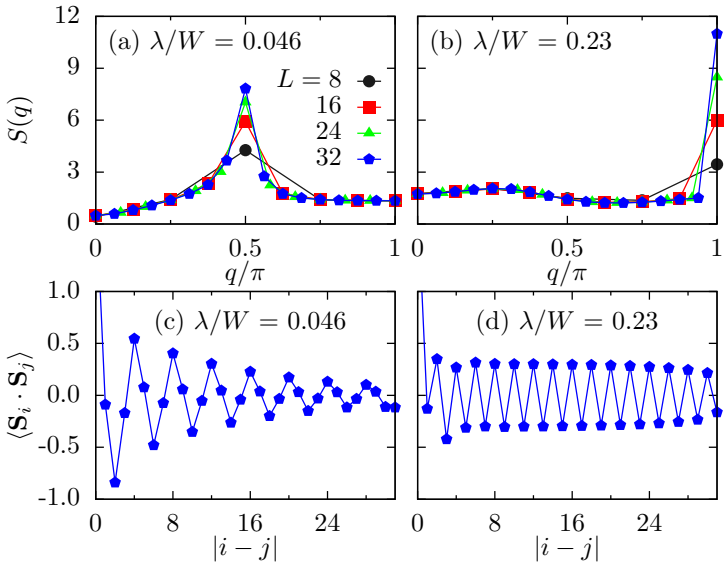

Figure 2.5: DMRG resuls obtained at $U/W = 1$. Panels (a) and (b) contain the spin structure factor in the block phase and in the EXI phase, respectively, for various number of sites $L = 8$ (black), 16 (red), 24 (green), and 32 (blue). Panels (c) and (d) display the real-space spin-correlations at $L = 32$ corresponding to the block and EXI phases, respectively, for the λ/W's indicated.

2.3.3 Strong Coupling

Consider now the large U/W limit. In Fig. 2.6(a-e) we present some results obtained at U/W=10. At small λ/W, we found a robust ferromagnetic (FM) spin order as shown in Fig. 2.6(d) via the spin structure factor. We also noticed that this FM spin ordering is always accompanied by orbital ordering, as discussed in previous investigations in the absence of spin-orbit coupling [27]. To clarify the nature of the orbital order, we show $\langle \tau_z(i)\tau_z(j)\rangle$ in Fig. 2.6(e), where $\tau_z(i) = n_{iyz} - n_{ixz}$ is the z component of the pseudospin operator in orbital space. This orbital ordering leads to the opening of a gap in the system rendering the state an orbital-ordered insulator (OOI), as discussed in [27] via determinant Quantum Monte Carlo and DMRG calculations without spin-orbit coupling.

By increasing λ/W, we have observed a transition from FM to the AFM spin ordering shown in Fig. 2.7(a,b). As in Sec. III.B, this AFM ordering is accompanied by staggering in the exciton pair-pair correlation as shown in Fig. 2.7(c,d). Similar phases were noticed

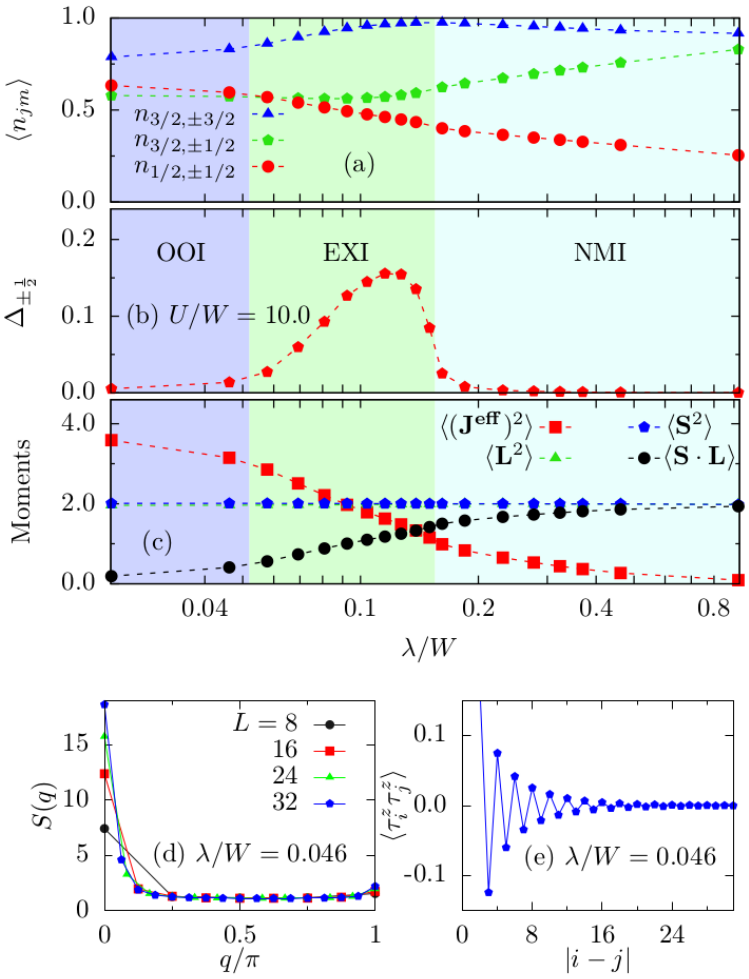

Figure 2.6: DMRG results obtained at $U/W = 10$ (strong coupling regime). Panel (a) shows the occupation number in the (j^{eff}, m) bands, while panel (b) displays the excitonic order parameter dependence on λ/W. Panel (c) displays the local moment strengths and also $\langle\mathbf{S.L}\rangle$. Panel (d) contains the spin structure factor for a number of sites L equal to 8 (black), 16 (red) , 24 (green), and 32 (blue). Panel (e) shows $\langle\tau_z(i)\tau_z(j)\rangle$ for L=32. Both (d) and (e) are in the ferromagnetic and orbitally ordered phase at $\lambda/W = 0.046$.

in a study of the low-energy effective Hamiltonian for the $(t_{2g})^4$ sector in [57]. Note that at $U/W = 10$ the excitonic condensate starts at smaller λ/W than those needed at intermediate value of U/W [Fig. 2.6(b)]. Interestingly, in the EXI phase we noticed that $\langle n_{3/2,\pm 3/2}\rangle$ converges to ≈ 1 (to be precise 0.98) and then reverses the trend and starts decreasing in the region identified as a non-magnetic insulator (see below). This is different from the

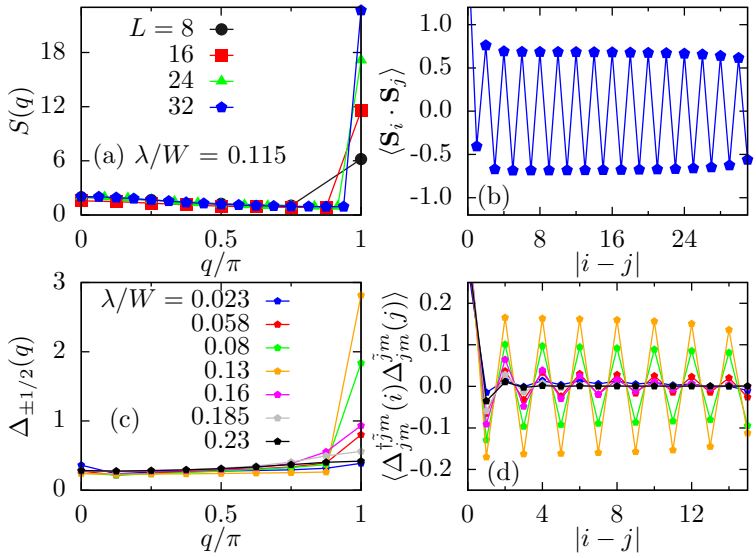

Figure 2.7: DMRG results obtained at U/W=10. Panel (a) depicts the spin structure factor in the EXI phase at λ/W=0.115, for a number of sites L equal to 8 (black), 16 (red), 24 (green), and 32 (blue). Panel (b) shows the real-space averaged spin-spin correlations for λ/W=0.115. In (c) and (d), we present the pair-pair correlation in momentum and real space, respectively, for $L = 16$. In panel (d) $j = 1/2$, $\tilde{j} = 3/2$, and $m = \pm 1/2$ were used.

properties of the EXI phase at intermediate U/W where $\langle n_{3/2,\pm 3/2} \rangle < 1$ and then slowly converged to 1 as the system evolves to become a band insulator increasing λ/W further.

At U/W=10, and at any λ/W, we also noticed that $\langle \mathbf{S}^2 \rangle = 2$ and $\langle \mathbf{L}^2 \rangle = 2$ [Fig. 2.6(c)]. These vector operators become parallel only for large λ/W, namely where $\langle \mathbf{S} \cdot \mathbf{L} \rangle$=2 and $\langle (\mathbf{J}^{eff})^2 \rangle$=0. In Fig. 2.7(d) we show the pair-pair excitonic correlation as a function of distance, involving the operator $\Delta^{\tilde{j},m}_{j,m}(i) = a^{\dagger}_{i\tilde{j}m} a_{ijm}$. In all points studied inside the EXI phase we observed a staggering in the pair-pair correlation. In Fig. 2.7(c), we show $\Delta_m(q) = \frac{1}{L} \sum_{i,j} e^{q(i-j)} \langle \Delta^{\dagger \tilde{j}m}_{jm}(i) \Delta^{\tilde{j}m}_{jm}(j) \rangle$ for various λ's at strong U, where q is the momentum.

In Fig. 2.8 we present $(\langle n_l^2 \rangle - \langle n_l \rangle^2) = \frac{1}{L} \sum_i \langle n_{i,l}^2 \rangle - \langle n_{i,l} \rangle^2$, where the index l takes the values indicated in the legend of panel (a), namely $j^{eff} = 1/2$, $(j^{eff}, |m|) = (3/2, 1/2)$, $(j^{eff}, |m|) = (3/2, 3/2)$, and $Total$ ($n_{Total} = \sum_{i,j,m} n_{ijm}$). Interestingly, we noticed that in the EXI phase the charge fluctuations increase for $j^{eff} = 1/2$ and $(j^{eff}, |m|) = (3/2, 1/2)$: these are the bands where excitons are located, and this feature is common for both intermediate and

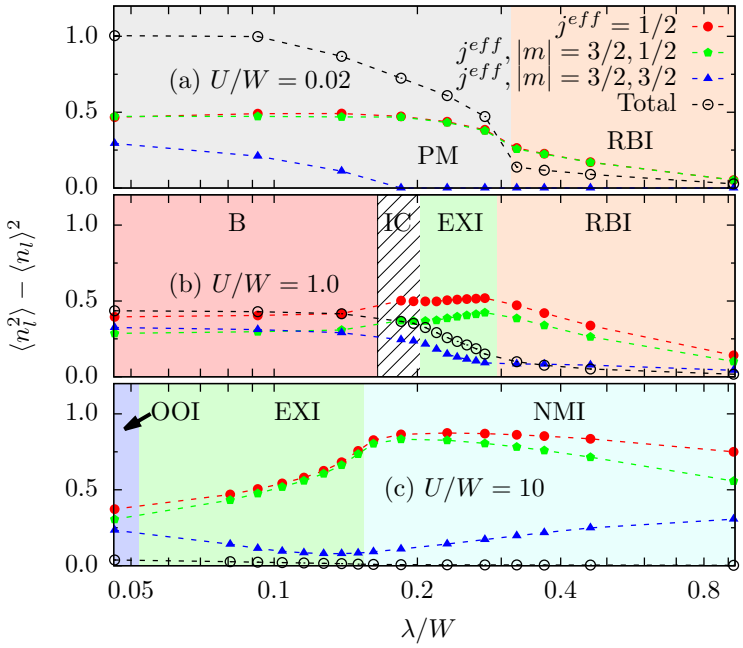

Figure 2.8: Averaged local charge fluctuations of the (j^{eff}, m) states (as indicated in the upper panel legend) corresponding to (a) $U/W = 0.02$ (weak coupling), (b) $U/W = 1$ (intermediate coupling), and (c) $U/W = 10$ (strong coupling).

strong coupling EXI regimes. However, we have identified some differences within the EXI region between the intermediate and strong Hubbard coupling regions. In strong coupling [Fig. 2.8(c)] we noticed that in the EXI regime the local charge fluctuations per site are nearly zero, suggesting that electrons are almost localized. However, at intermediate coupling [$U/W = 1$, Fig. 2.8(b)] and still within the EXI regime, the total charge fluctuations are nonzero. Nonzero local charge fluctuations in the EXI phase hints towards exciton pairs that are extended in size, namely the BCS type limit of excitonic phases. In the other extreme, namely the Bose-Einstein condensation (BEC) limit, the excitonic phase should have small charge fluctuations because the exciton pairs are considerably smaller and of atomic-scale size. A more detailed study of the BCS-BEC crossover within the excitonic phase when moving from intermediate to strong coupling U/W is discussed in Chapter 3.

In the strong coupling region of focus here and in the neighborhood of the EXI phase we have found a non-magnetic insulator (NMI) with $\langle(\mathbf{J}^{eff})^2\rangle \neq 0$. Let us contrast the NMI and RBI regions. To identify the NMI regime we focused on two aspects: *(i)* the system should have localized electrons due to strong correlations; *(ii)* there is no magnetic ordering. The first condition was checked by calculating local charge fluctuations, as shown in Fig. 2.8, where we observed that the local charge fluctuations are zero throughout this region [Fig. 2.8(c)]. This is merely a strong correlation effect different from the case of the small U/W and large λ/W regime (RBI) where electrons are primarily in extended states but still having zero local charge fluctuations because of having nearly full and empty bands. As depicted in Fig. 2.8(a,b), in the RBI region the local charge fluctuations separately in each (j^{eff}, m) state as well as $Total$ are small or nearly zero. On the other hand, in the NMI region only $Total$ is zero but charge fluctuations separately for each (j^{eff}, m) are large [shown in Fig. 2.8(c)]. This suggests that in the case of NMI the electrons are not locked just as the consequence of having a fully filled band or an empty band like in RBI, but as a consequence of strong correlations.

In recent work using DMFT [64] for a cubic $(t_{2g})^4$ system, a $\langle(\mathbf{J}^{eff})^2\rangle$=0 NMI state was also found in the vicinity of the excitonic condensate and it was identified as a Van Vleck-type Mott insulator, as discussed earlier in [85]. Our finding of a NMI state with $\langle(\mathbf{J}^{eff})^2\rangle \neq 0$ near the excitonic condensate seems in contrast with those previous studies, but it is merely a consequence of using a non-cubic band structure. Interestingly, this breakdown of the $\langle(\mathbf{J}^{eff})^2\rangle$=0 state was also recently noticed in first-principle calculations [86, 51] applied to the $(t_{2g})^4$ iridate Sr_2YIrO_6. In our results, and to the best of our accuracy, the $\langle(\mathbf{J}^{eff})^2\rangle \neq 0$ NMI region is smoothly connected to the $\langle(\mathbf{J}^{eff})^2\rangle$=0 region.

2.4 Conclusions

In this Chapter, using an accurate computational technique we have studied the phase diagram of an electronic model simultaneously with Hubbard, Hund, and spin-orbit couplings. The hopping amplitudes were fixed to those used in a previous study at $\lambda = 0$, since that effort already unveiled a variety of interesting phases such as the OSMP regime.

In the present analysis our main result is shown in Fig. 2.2. The previously identified Block and FM-OO phases were followed increasing λ. Eventually, over a broad range of U/W an excitonic condensate phase was identified, in qualitative agreement with previous DMFT studies. The large λ regime is also interesting, with a variety of insulating regions.

Conceptually, our analysis provides an avenue to study quasi-one dimensional materials with robust spin-orbit coupling. We provide a tentative partial list of materials of this class in the introduction and throughout the text. In combination with *ab-initio* techniques, needed for the hopping amplitudes, our many-body procedure can unveil properties of these systems in reduced dimensionality with good precision to guide experiments. We hope our work triggers the cross-fertilization between theory and experiments needed to develop the novel field of quasi-one dimensional iridates, or other related low-dimensional materials with robust spin-orbit coupling.

The presence of the novel phase, with antiferromagnetic ordering and excitonic condensation, is exciting because real materials with 4d/5d ions have smaller values of U in comparison to 3d transition metal oxides. Properties of this phase is further investigated in the next chapter, using a simpler model having degenerate orbitals.

Chapter 3

BCS-BEC crossover in a $(t_{2g})^4$ Excitonic Magnet

3.1 Introduction

The concept of excitonic condensation has attracted considerable attention since its early theoretical prediction [79, 80, 81]. An exciton is a bound state of an electron-hole pair. This composite particle resembles the Cooper pair of superconductors and follows hard-core bosonic statistics. Early work involving semiconductors showed that in the weak-coupling limit (small U), near the semimetal to semiconductor transition, the system can become unstable against the formation of multiple excitons [87, 88]. This can lead to a condensation into a BCS-like macroscopic state called excitonic insulator. The associated BCS wavefunction can smoothly transform into a BEC state when the gap between bands increases at fixed Hubbard repulsion U. In strongly correlated systems, a BEC-like excitonic insulator can also occur in the strong coupling limit (large U). This regime attracted theoretical investigations [83, 89, 90] and was studied using large U perturbation theory, where the hopping amplitude t is the small parameter.

The extended Falicov-Kimball model has often been used as a minimal theoretical model to address excitonic condensation [91, 92, 93]. Only recently, more realistic, and more difficult, three-orbital Hubbard models were explored to study this state [64, 65, 94, 95]. On the experimental side there have been studies showing reliable signatures of the excitonic

condensate in real materials, such as in transition metal dichalcogenides [96], Ta_2NiSe_5 [97], and in bilayer systems [98, 99]. To better understand excitonic insulators it is important to find additional candidate materials and additional theoretical models where this state occurs and can be studied in detail. Excitonic condensation induced by spin-orbit coupling in the t_{2g}^4 case is also an promising avenue, as discussed in last chapter and is focus of the present chapter. Theoretically, it was predicted that the three-orbital Hubbard model with a degenerate t_{2g} space and in the LS coupling limit ($U \gg t, \lambda$) leads to the BEC state of triplons (singlet-triplet excitations) [85, 56, 57]. We will show that these triplon excitations are low-energy manifestations of spin-orbit excitons. Dynamical Mean Field Theory (DMFT) calculations also supported similar findings [64, 65], although it is difficult to distinguish between BCS and BEC states using this technique. The study of the ground state of a one-dimensional spin-orbit coupled three-orbital Hubbard model in a non-degenerate (tetragonal) t_{2g} space in Chapter 2 also showed a phase with staggered spin-orbit excitonic correlations [94]. All the above mentioned studies revealed an antiferromagnetic ordering accompanying the excitonic condensate. The t_{2g}^4 case is relevant for materials with Ir^{5+} ions and other $4d/5d$ transition metal oxides with the same doping $n = 4$. The presence of triplon condensation was initially discussed for double perovskite materials, such as Sr_2YIrO_6 and Ba_2YIrO_6 with a $5d^4$ configuration [52, 54, 55, 53, 100, 101], but RIXS experiments showed that the triplon excitations bandwidth is not sufficiently large compared to λ to develop condensation [102]. Note that recent RIXS experiments on Ca_2RuO_4 suggests that this could be a candidate material for excitonic magnetism [103], and *ab-initio* calculations have reached the same conclusion [104].

To investigate the spin-orbit excitonic condensation, in this chapter we use a simple degenerate three-orbital Hubbard model. Using numerically exact DMRG simulations on one-dimensional chains, we show that an excitonic condensation is induced accompanied by antiferromagnetic ordering even in the intermediate Hubbard regime ($U/W \approx 1$). This regime is stabilized by increasing sufficiently λ starting at the $\lambda = 0$ incommensurate spin-density wave metallic phase. These results cannot be understood using large U perturbation theories. Moreover, by using the Hartree-Fock approximation (HFA) in two-dimensional ($2d$) lattices, we also found a similar excitonic insulator phase, both in the weak and intermediate

U/W regimes. As our main result, we show that there is a BCS-BEC crossover inside the excitonic condensate phase, both in $1d$ and $2d$ lattices. The BCS limit of the excitonic insulator occurs at intermediate U/W (and also for weak U/W in $2d$), and by increasing λ (at fixed U/W) the BEC state is reached. The previously known large U/W BEC state, due to triplon condensation, appears smoothly connected to the BCS excitonic insulator of intermediate U. We also provide the full λ vs U phase diagrams for $1d$ and $2d$ lattices using the many-body techniques discussed above.

The organization of this chapter is as follows. In Sec. 3.2, the model and the computational methodology used are presented. In Sections 3.3 and 3.4, the main results are shown. In particular, in Sec. 3.3, the results on $1d$ lattices using the DMRG technique are presented. In Sec. 3.4, the results on $2d$ lattices using HFA further support our main proposal of a BCS-BEC crossover in the model studied. In Sec. 3.5, we discuss the overall results and present our conclusions.

3.2 Model and Method

For our study, we use a degenerate three-orbital Hubbard model. The Hamiltonian has three primary terms: the tight-binding kinetic energy, the standard on-site multiorbital Hubbard interaction, and the on-site spin-orbit coupling (SOC): $H = H_K + H_{\rm int} + H_{SOC}$. The tight-binding term is

$$H_K = \sum_{\langle i,j\rangle,\sigma,\gamma,\gamma'} t_{\gamma\gamma'}(c^\dagger_{i\sigma\gamma}c_{j\sigma\gamma'} + \text{H.c.}). \tag{3.1}$$

The hopping amplitudes $t_{\gamma\gamma'}$ connect only nearest-neighbor lattice sites (in both the $1d$ chain and $2d$ square lattices). As discussed earlier, here we use degenerate orbitals, i.e. $t_{\gamma\gamma'} = \delta_{\gamma\gamma'}t$. We fixed $t = 0.5$ and all of our results are presented in terms of dimensionless ratios, such as U/W and λ/W. The total bandwidth is $W = 4.0|t|$ and $8.0|t|$ for the $1d$ and $2d$ lattices, respectively. The orbitals used – labeled as 0, 1, and 2 – could be associated respectively to the d_{yz}, d_{xz}, and d_{xy} orbitals, namely the t_{2g} sector. In real materials, the above hoppings can be much more complex [105], but nonetheless this simple model is useful to gain conceptual

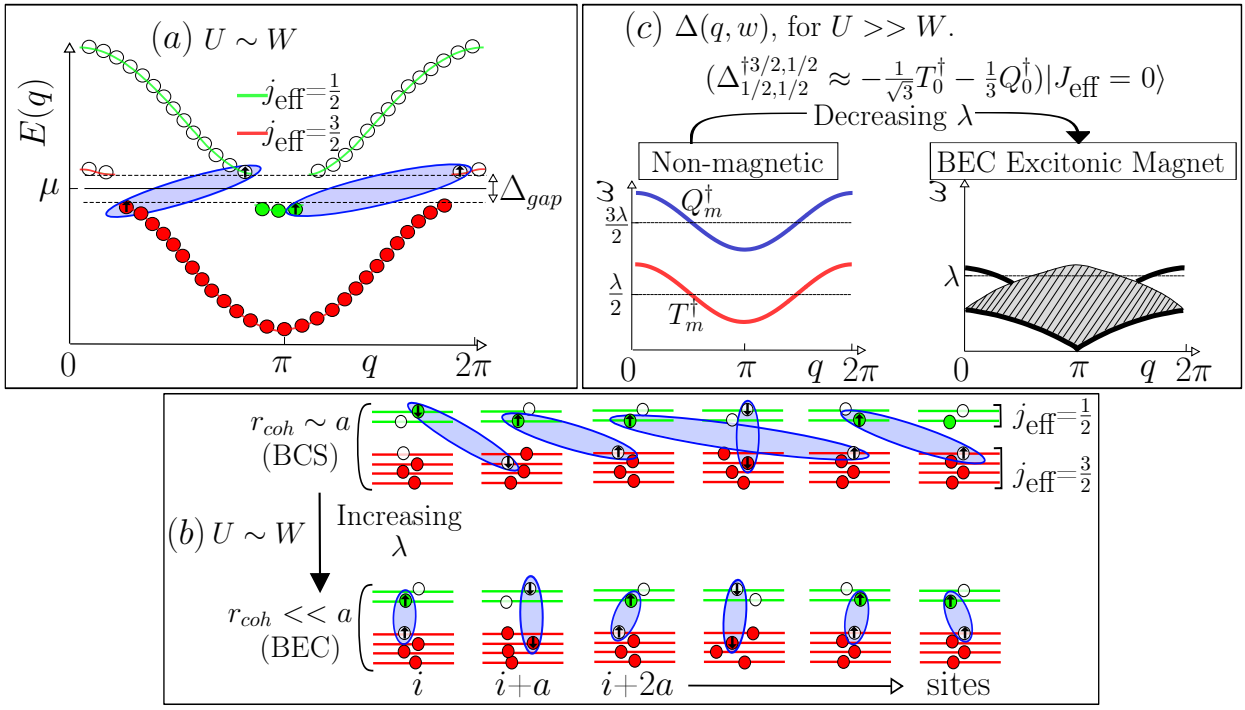

Figure 3.1: Visual representation of our main results, all supported by actual DMRG and Hartree Fock calculations. In (a), the single-particle excitations of the $j_{\text{eff}} = 3/2$ and $j_{\text{eff}} = 1/2$ bands are shown at intermediate U, where near the chemical potential a gap opens due to the formation of excitons (note electron and hole have the same m). The $j_{\text{eff}} = 3/2$ and $j_{\text{eff}} = 1/2$ bands open gaps near momentum $q \approx 0$ and $q \approx \pi$, respectively. In (b), the real-space perspective of the excitonic state (at intermediate U) is shown, where the exciton's mean radius (characterized by the coherence length) decreases by increasing λ. In (c), the excitonic condensation in strong coupling is depicted. The local exciton creation operator leads to the creation of both a triplon and a quintuplon when acting on $|J_{\text{eff}} = 0\rangle$. Including kinetic energy, i.e. the tight-binding term, the triplon and quintuplon excitations gain bandwidths, and decreasing λ leads to the BEC of the triplon component.

understanding. The on-site multiorbital Hubbard interaction term and the SOC term are same as used in the previous chapter.

Using the model described above, we performed calculations on one-dimensional chains employing the DMRG [76, 77] for various system lengths $L = 16$, 24, and 32 sites. We kept up to 1600 states for the DMRG process and maintained a truncation error below 10^{-8} throughout the finite algorithm sweeps. We used the corrected single-site DMRG

algorithm [78] with correction $a = 0.001$-0.008, and performed 35 to 40 finite sweeps to gain proper convergence depending on the system size. After this convergence, we calculated the spin-structure factor $S(q)$, orbital-structure factor $L(q)$, excitonic momentum distribution function $\Delta_{m=1/2}(q)$, and coherence length r_{coh}. From all these observables, we constructed the phase diagram. To calculate spectral functions with the DMRG, we used the correction vector method [106], with the Krylov-space approach [107]. We obtain the single-particle spectral function $A(q,\omega)$ and the excitonic pair-pair susceptibility $\Delta_{m=1/2}(q,\omega)$. These frequency-dependent observables require considerable computational time, and multiple compute nodes. In our DMRG, we target the total J^z_{eff} of the system to reduce the computational cost [94]. Details of the Hartree-Fock calculations are in the Appendix B.5.

3.3 DMRG results in one dimension

Consider first the DMRG numerical results for one-dimensional chains. Figure 3.1 visually summarizes our conclusions. Within our numerical accuracy, we observed that the excitonic condensation starts at intermediate Hubbard $U \approx \mathcal{O}(W)$. This exciton condensation opens a gap in the $j_{\text{eff}} = 3/2$ and $j_{\text{eff}} = 1/2$ bands at momentum $q = 0$ and $q = \pi$, respectively, see Fig. 3.1(a). A similar perspective for the gap opening near the Fermi level was discussed in early research for semimetals [79, 80, 81]. At intermediate U, we noticed the excitons condense at finite momentum π and in the triplet channel (see Appendix B.3). We also noticed that increasing λ decreases the coherence length (r_{coh}) of electron-hole pairs from approximately one lattice spacing (a) to a much smaller number $r_{coh} << a$, resembling the BCS-BEC crossover. Although at extreme BCS r_{coh} can be as large as hundreds of lattice spacings, in our finite and one dimensional system we only found a robust indication for a maximum r_{coh} of approximately $1.0a$ which definitely is different from the atomic BEC limit. Confirming that indeed we found a BCS-BEC crossover at intermediate U, we performed mean-field calculations on $2d$ lattices (Sec. IV), where we found r_{coh} as large as $\mathcal{O}(10a)$ in the BCS limit.

We also found clear differences between the momentum distribution functions of the local excitations in the BCS and BEC limits in one dimension. The excitonic operator $\Delta^{\dagger 3/2,m'}_{1/2,m} =$

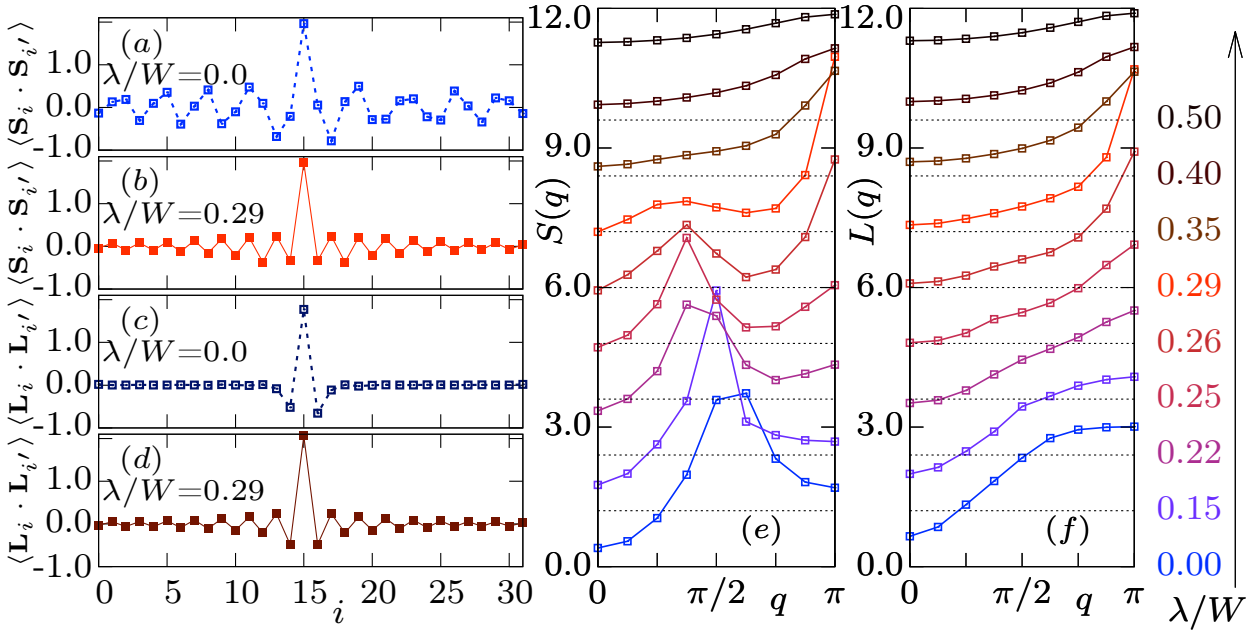

Figure 3.2: DMRG results at $U/W = 2$. (a) and (b) show the real-space spin-spin correlations at $\lambda/W = 0$ and $\lambda/W = 0.29$, repectively. In (c) and (d), the real-space orbital-orbital correlations are shown at $\lambda/W = 0.0$ and $\lambda/W = 0.29$, respectively. The spin structure factor $S(q)$ and orbital structure factors $L(q)$ are in (e) and (f), respectively, for various λs. In (a,b,c,d) the system size was $L = 32$ and one site is fixed at the center i.e. $i' = 15$. A system size $L = 16$ is used for (e,f).

$a^\dagger_{1/2,m} a_{3/2,m'}$ in the single-atom LS coupling limit can be written using triplon and quintuplon excitations (see Appendix B.2), corresponding, respectively, to $\mathbf{T}^\dagger_n |J^z_{\rm eff} = 0, J_{\rm eff} = 0\rangle = |n, 1\rangle$, and $\mathbf{Q}^\dagger_l |J^z_{\rm eff} = 0, J_{\rm eff} = 0\rangle = |l, 2\rangle$, where $n \in \{\pm 1, 0\}$ and $l \in \{\pm 2, \pm 1, 0\}$. Calculating the pair-pair susceptibity of excitons $\Delta(q, \omega)$ for chains, in the strong-coupling non-magnetic phase, we found bands of triplon and quintuplon excitations, with minima at $q = \pi$ but both bands are gapped. Decreasing λ drives the system to the BEC state, where $\Delta(q, \omega)$ has gapped triplon and quintuplon excitations only near $q = 0$ but mainly a continuum of excitations at other momenta above the Goldstone-like modes emerging from $q = \pi$, as sketched in Fig. 3.1(c).

3.3.1 Magnetic properties and staggered excitonic correlations

Now consider the results for magnetism in one-dimensional chains. We choose $U/W = 2.0$ and $U/W = 10.0$ as representative points for the intermediate and strong coupling regions, respectively. First, consider the intermediate coupling region where at $\lambda = 0$ we found an incommensurate spin-density wave (IC-SDW) via the spin-spin correlation $\langle \mathbf{S}_i \cdot \mathbf{S}_{i'} \rangle$ together with an exponential fast decay in the orbital-orbital correlation $\langle \mathbf{L}_i \cdot \mathbf{L}_{i'} \rangle$, as shown in Figs. 3.2(a,c). Block magnetic states as in previous DMRG studies [94, 108, 109, 110], do not appear in our model at $\lambda = 0$. Increasing λ drives the system towards antiferromagnetism with staggered spin-spin and orbital-orbital correlations, see Figs. 3.2(b,d). For additional confirmation, we show the spin structure factor $S(q) = (1/L) \sum_{j,m} e^{\iota q(j-m)} \langle \mathbf{S}_j \cdot \mathbf{S}_m \rangle$, and the orbital structure factor $L(q) = (1/L) \sum_{j,m} e^{\iota q(j-m)} \langle \mathbf{L}_j \cdot \mathbf{L}_m \rangle$ for various λ values. As λ increases, the incommensurate peak in $S(q)$ in Fig. 3.2(e) shifts to lower q values. The antiferromagnetic tendencies, shown by the $q = \pi$ peak, starts only near $\lambda = 0.22W$, and on further increasing λ the $q = \pi$ peak grows and the incommensurate peak is reduced. At larger λ's, the $S(q = \pi)$ peak decreases as the system transitions into the non-magnetic state. The orbital structure factor $L(q)$ displays similar behaviour at $q = \pi$. $L(q)$ starts with a flat plateaux near $q = \pi$, then grows when increasing λ, and eventually the $L(q = \pi)$ peak vanishes for very large λ, see Fig. 3.2(f).

In strong coupling and at $\lambda = 0$, the spins align ferromagnetically and orbital-orbital correlations show a "$+--+--$" pattern, with peaks at momentum $q = 0$ and near $q = 2\pi/3$ in $S(q)$ and $L(q)$, respectively (Fig. 3.3). Recent DMRG calculations on the low-energy S=1 and L=1 model showed similar results in the orbital correlations [111] at $\lambda = 0$. As λ increases, the system enters into the phase where orbital ordering becomes staggered, as shown by a peak at $q = \pi$ for $\lambda = 0.05W$ in Fig. 3.3(a). However, the spin ordering is dominantly ferromagnetic with secondary antiferromagnetic tendencies leading to a small peak at $q = \pi$ [Fig. 3.3(b) for $\lambda = 0.05W$]. Further increasing λ, both $L(q = \pi)$ and $S(q = \pi)$ grow while $S(q = 0)$ decreases, and ultimately $L(q = \pi)$ and $S(q = \pi)$ also start decreasing when the system enters into the non-magnetic phase with exponentially decaying spin and orbital correlations.

In our DMRG calculations, the development of antiferromagnetic correlations in the spin and orbital channels is always accompanied by staggering in the exciton-exciton correlations,

both at intermediate and strong coupling. We estimate the amount of staggering in excitonic correlation for our chains using:

$$\Delta_m = \frac{1}{L^2} \sum_{|i-i'|>0} (-1)^{|i-i'|} \langle \Delta^{\dagger 3/2,m}_{1/2,m}(i) \Delta^{3/2,m}_{1/2,m}(i') \rangle, \tag{3.2}$$

where $m \in \{\pm 1/2\}$. In Fig. 3.3(c), the evolution of $\Delta_{1/2}$ is shown when changing λ, where each panel belongs to a different U/W. We found that smaller λ's are needed as U/W increases to obtain staggered excitonic correlations. A finite range of λ where the excitonic correlations are staggered is present for U/W as low as 1.5, although the magnitude of $\Delta_{1/2}$ decreases as U/W decreases, and for $U/W \lessapprox 1.0$ we were unable to identify – within our numerical accuracy – the region with staggered excitonic correlations. Nonetheless, it is interesting that we find staggered excitonic correlations at intermediate U, where small λ shows IC-SDW metal (for evidence of metallicity see Sec. 3.3.2). Perturbation theories at $U \gg t, \lambda$ cannot explain these results.

3.3.2 BCS-BEC crossover, and IC-SDW metal to BCS-Excitonic insulator transition

Now we will discuss the main result of this chapter, where we present the numerical evidence for the BCS-BEC crossover in the excitonic condensate. At intermediate U/W – the value $U/W = 1.75$ is chosen merely for simplicity – there is a finite range of $\lambda/W \in \{0.28, 0.4\}$ where staggering in excitonic, spin, and orbital correlations is present. We calculate the coherence length $r_{coh}(m)$ using the widely-employed formula [83, 112, 84]

$$r_{coh}(m) = \sqrt{\frac{\sum_{ij} |i-j|^2 \langle a^\dagger_{i\frac{1}{2}\frac{m}{2}} a_{j\frac{3}{2}\frac{m}{2}} \rangle}{\sum_{ij} \langle a^\dagger_{i\frac{1}{2}\frac{m}{2}} a_{j\frac{3}{2}\frac{m}{2}} \rangle}}, \tag{3.3}$$

where $m \in \{\pm 1/2\}$, for the points lying inside the excitonic condensate region at fixed $U/W = 1.75$, namely the Path-1 shown in Fig. 3.6. Note that $r_{coh}(1/2) = r_{coh}(-1/2)$.

Interestingly, we found that as λ increases, r_{coh} decreases from nearly one lattice spacing $\approx a$ to $\approx 0.2a$, see Fig. 3.4(c). This reduction in the coherence length

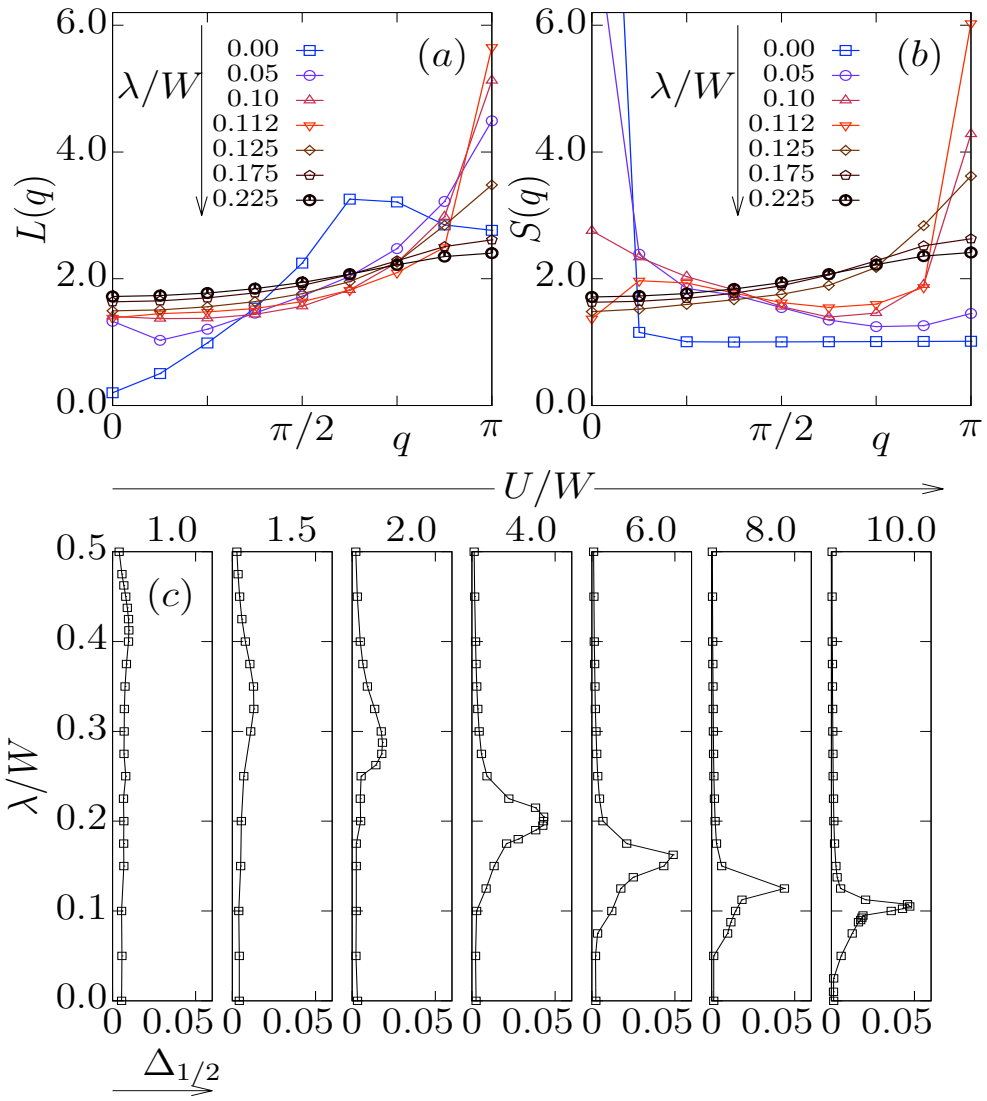

Figure 3.3: Results calculated using DMRG for a one-dimensional chain of $L = 16$ sites. In (a) and (b), the orbital structure factor $L(q)$ and spin structure factor $S(q)$ are shown, respectively, at $U/W = 10$ and various λ/W's. Panel (c) shows the measure of staggering in excitonic correlations $\Delta_{1/2}$ for various values of λ and U.

of electron-hole pairs resembles the BCS-BEC crossover already discussed in semiconductors near the semi-metal to semiconductor transition [79, 80, 81, 87, 88]. We also calculate r_{coh} for various values of λ and U when transitioning from the intermediate to the strong coupling limits, while being still inside the excitonic condensate, which we call Path-2 (see Fig. 3.6), as shown in Fig. 3.4(d). Here again we found that r_{coh} decreases from $\mathcal{O}(a)$ to

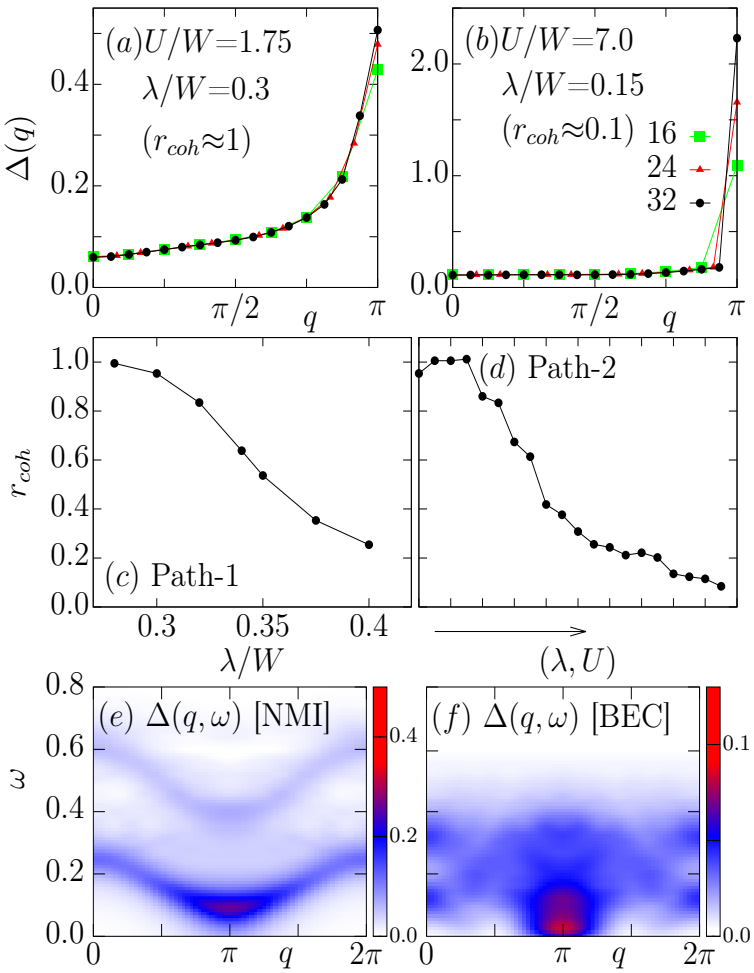

Figure 3.4: Panels (a) and (b) show the momentum distribution function of excitons $\Delta(q)$ for system sizes $L = 16, 24, 32$ at two representative points of the BCS and BEC regions, respectively. Panels (c) and (d) show the coherence length for two paths inside the excitonic condensate regime, shown in the phase diagram Fig. 3.6. The pair-pair susceptibilities $\Delta(q, \omega)$ are in panel (e) at $U/W = 10$ and $\lambda/W = 0.2$ i.e. in the non-magnetic insulator (NMI) region, and in panel (f) at $U/W = 10$ and $\lambda/W = 0.11$ i.e. in the BEC region. All the calculations used DMRG.

$\mathcal{O}(0.1a)$. The ordered $(\lambda/W, U/W)$ points choosen for Path-2 are $\{(0.3, 1.75)$, $(0.29, 2.0)$, $(0.29, 2.25)$, $(0.287, 2.3)$, $(0.285, 2.35)$, $(0.283, 2.4)$, $(0.28, 2.5)$, $(0.279, 2.525)$, $(0.277, 2.55)$, $(0.275, 2.6)$, $(0.27, 2.65)$, $(0.25, 2.8)$, $(0.24, 3.0)$, $(0.23, 3.5)$, $(0.21, 4.0)$, $(0.2, 4.5)$, $(0.17, 6.0)$, $(0.15, 7.0)$, $(0.13, 9.0)$, $(0.11, 10.0)\}$. Note that for $U/W \gtrapprox 2.75$, the coherence length is small as expected because at these values of U, the system is already in strong coupling for $\lambda = 0$.

In Fig. 3.4(a,b) we show the excitonic momentum distribution function $\Delta(q) = (1/L)\sum_{i,j}\langle e^{\iota q(i-j)}\Delta^{\dagger 3/2,m}_{1/2,m}(i)\Delta^{3/2,m}_{1/2,m}(j)\rangle$ for two points ($\lambda/W = 0.3$, $U/W = 1.75$) and ($\lambda/W = 0.15$, $U/W = 7.0$), at the intermediate U BCS and strong U BEC regions. In the BCS limit, $\Delta(q = \pi)$ grows very slightly with system size L. However, in the BEC region we found nearly linearly increasing $\Delta(q = \pi)$ with L, implying either a very slow power-law decay or even true long-range order. Such a true long-range order in our one dimension is allowed as the $U(1)$ symmetry related to the excitonic condensation is explicitly broken by a finite Hund coupling [95]. The analysis above also clearly implies that as we increase the system size and hence increase the number of excitons, these excitons can condense also at momentum $q \neq \pi$ in the BCS limit, whereas in the BEC limit excitons condense only at $q = \pi$. For completeness, note that a similar BCS-BEC crossover has also been reported in the extended Falicov-Kimball model in one-dimensional chains [91].

As discussed before, the exciton creation (i.e. electron-hole pair excitation) becomes the triplon and quintuplon excitation in the atomic LS limit. We calculated the excitonic pair-pair susceptibility

$$\Delta(q,\omega) = \langle\Psi_0|\Delta^{\dagger 3/2,1/2}_{1/2,1/2}(q)\frac{1}{\omega + i\eta - H + E_0}\Delta^{3/2,1/2}_{1/2,1/2}(q)|\Psi_0\rangle \tag{3.4}$$

at large $U/W = 10.0$ on one-dimensional chains to study the effect of the kinetic energy. The broadening η was 0.05eV. We choose two values $\lambda/W = 0.20$ and $\lambda/W = 0.11$ in the non-magnetic insulator and BEC regions, respectively [Figs. 3.4(e,f)]. For the non-magnetic state, we found the pair-pair susceptibility shows two cosine-like bands with minima at $q = \pi$, where the lower band belongs to $\Delta J_{\text{eff}} = 1$ (triplon) and the upper band represent $\Delta J_{\text{eff}} = 2$ excitations, as in previous analytical studies [57]. The BEC is expected to occur by reducing λ, when the lower band of triplons becomes gapless. In our BEC state, $\Delta(q,\omega)$ shows features very different from those in the non-magnetic state: after removing the elastic peak we found that two gapped bands appear only near $q = 0$, and the spectrum at $q = \pi$ is now gapless with emerging Goldstone-like modes. We also found continuum-like features for $q \in \{-\frac{\pi}{4}, \frac{7\pi}{4}\}$.

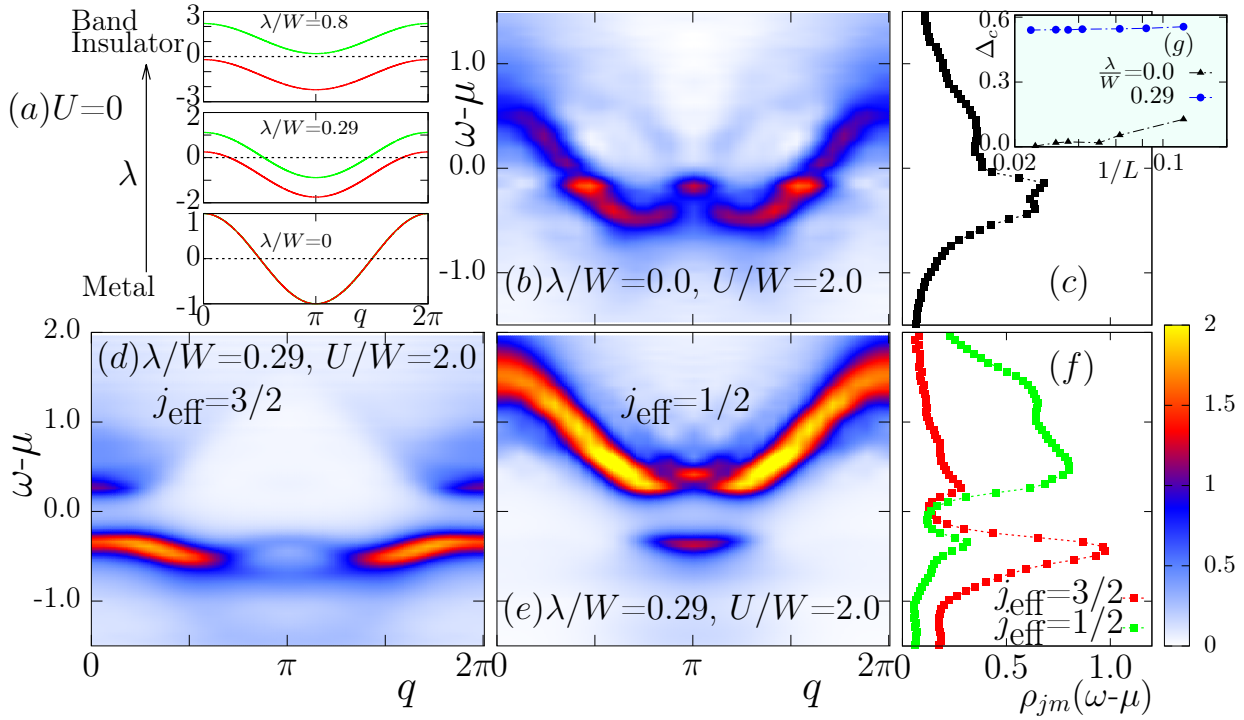

Figure 3.5: The single-particle spectral function calculated using DMRG. The non-interacting band structure is shown in panel (a). Panel (b) contains $A_{jm}(q,\omega)$ for $\lambda = 0$ and $U/W = 2.0$, in the IC-SDW metallic phase. In panels (d,e) $A_{jm}(q,\omega)$ at $\lambda/W = 0.29$ and $U/W = 2.0$ is shown inside the excitonic insulator phase ($r_{coh} = 1.019$). Panels (c) and (f) show the single-particle DOS ($\rho_{jm}(\omega)$) at $\lambda = 0.0$ and $\lambda = 0.29$, respectively. The scaling of the charge gap is in inset (g) for $(U/W = 2, \lambda/W = 0)$ and $(U/W = 2, \lambda/W = 0.29)$.

In the non-interacting limit, λ only splits the $j_{\text{eff}} = 3/2$ and $j_{\text{eff}} = 1/2$ bands, see Fig. 3.5(a), driving a metal to band-insulator transition. Only at finite U the excitonic condensation happens: as shown in our DMRG results, $U/W \gtrapprox 1.0$ is required to obtain a noticeable staggering in the excitonic correlations. To further investigate the intermediate U region, we calculated the single-particle spectral function $A_{jm}(q,\omega)$ (see Appendix B.4) at $U/W = 2$, using both $\lambda = 0.0$ and $\lambda/W = 0.29$ corresponding to the IC-SDW and excitonic condensate with $r_{coh} \approx 1.0$ (BCS limit), respectively. In Fig. 3.5(b) we show $A_{jm}(q, \omega - \mu)$ for $\lambda = 0$: at this point all (j_{eff}, m) states are degenerate. Comparing to the non-interacting limit band structure, a renormalization of the bands is clearly visible, having two minima structure and a local maxima at $q = \pi$, as a consequence of the Hubbard repulsion. In

this phase, the nesting vector at the chemical potential μ decides the ordering vector of the incommensurate spin-density wave. We also show the single-particle density of states $\rho_{jm}(\omega - \mu)$, Fig 3.5(c), which indicates that the system has a finite density-of-states at μ suggesting this phase is metallic.

Figures 3.5(d) and (e) show $A_{j,m}(q, \omega - \mu)$ for $j_{\text{eff}} = 3/2$ (all $m \in \{\pm 3/2, \pm 1/2\}$ are degenerate) and $j_{\text{eff}} = 1/2$ (both $m \in \{\pm 1/2\}$ are degenerate), respectively. The gaps at μ, at wavevectors $q \approx 0$ and $q \approx \pi$ in the spectral functions of $j_{\text{eff}} = 3/2$ and $j_{\text{eff}} = 1/2$, respectively, are clearly present. These gaps appear due to the formation of bound states of electrons and holes, arising from the $q \approx 0$ and $q \approx \pi$ states of the $j_{\text{eff}} = 3/2$ and $j_{\text{eff}} = 1/2$ bands, respectively. This leads to excitons creation with net momentum $\approx \pi$ (indirect excitons). We also noticed a non-trivial suppression of the spectral function near $q = \pi$ for $j_{\text{eff}} = 3/2$, below μ, but the explanation for these small features requires further work. However, it is evident that the gap opens due to the formation of indirect excitons and eventually leads to a BCS-like state. In Fig. 3.5(f), the j-resolved density-of-states is shown to illustrate the suppression near μ for both the $j_{\text{eff}} = 3/2$ and $1/2$ bands. A small but finite density-of-states at μ is present because of the broadening η used. To confirm the transition from metal (at $\lambda = 0$) to excitonic insulator (at $\lambda/W = 0.29$), we performed finite-size scaling of the charge gap $\Delta_c = E_G(N+1) + E_G(N-1) - 2E_G(N)$ for both points, see Fig. 3.5(g). At $\lambda = 0.29$, using system sizes $L = 8, 12, 16, 24, 32$, and 42, we found the charge gap is quite robust 0.55 eV. Sizes $L = 8, 16, 20, 28, 32$, and 40 were used for the scaling at $\lambda = 0$, which indicates that Δ_c scales to ≈ 0 eV in the thermodynamic limit.

Figure 3.6 ends this section by displaying the full λ vs U phase diagram for our one-dimensional systems. The CPU-costly DMRG calculations were performed for all small circles shown using a system size $L = 16$. After obtaining the ground state, then spin-spin correlations, orbital-orbital correlations, and exciton-exciton correlations were calculated to analyze the properties of each phase. The (j_{eff}, m)-resolved local electronic densities were also studied to identify the relativistic band insulator phase. The dashed line inside the excitonic condensate region (green region) is a guide to the eyes to show the BCS and BEC limits of the excitonic condensate.

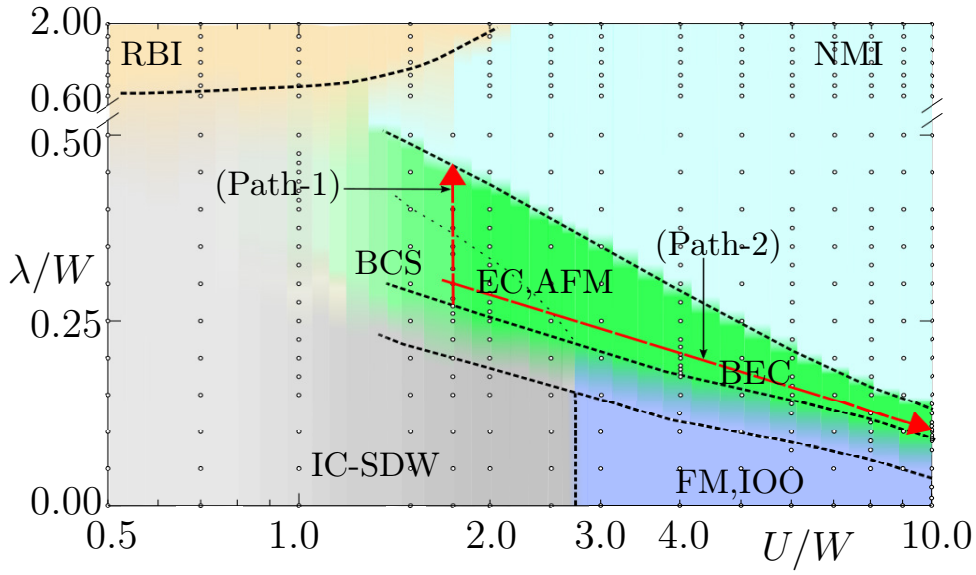

Figure 3.6: λ/W vs U/W phase diagram calculated using DMRG for a one-dimensional system. The two red arrows corresponds to the paths used in panels (c,d) of Fig. 3.4. The vertical red arrow is choosen at $U/W = 1.75$, and depicts Path-1 of Fig. 3.4(c). The diagonal red arrow corresponds to the Path-2 used in Fig. 3.4(d). The notation RBI, IC-SDW, FM, IOO, EC, AFM, and NMI stands for relativistic band insulator, incommensurate spin-density wave, ferromagnetic, excitonic condensate, antiferromagnetic, and non-magnetic insulator, respectively.

3.4 Hartree-Fock results in two-dimensions

In this section, we will present and discuss the results obtained in two-dimensional lattices by performing mean-field calculations in real-space. Hartree-Fock approximations are appropriate to study excitonic condensates as shown in the original publications that started this field [79, 80, 81], as well as in recent numerical calculations on Falicov-Kimball models [92, 113].

In Fig. 3.7(a), we show the full λ vs U phase diagram for the two-dimensional lattice. To identify the various phases, we calculated the spin structure factor and orbital structure factor on 16×16 clusters with periodic boundary conditions for all the points explicitly shown in the phase diagram. Our mean-field calculations in two dimensions capture almost

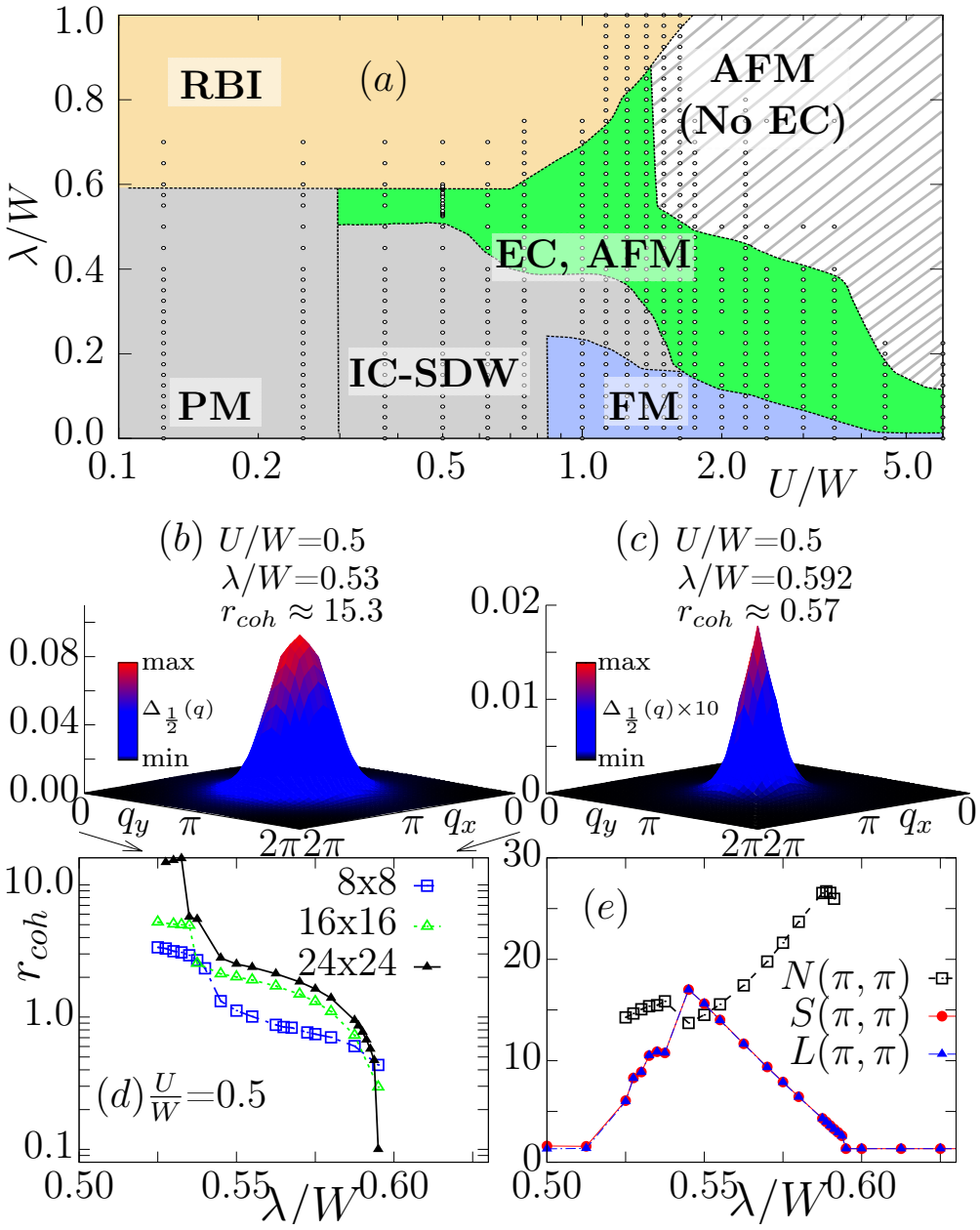

Figure 3.7: Panel (a) shows the λ vs U phase diagram for the square lattice, calculated using the Hartree-Fock approximation. In panels (b) and (c), the momentum distribution function of excitons $\Delta(\mathbf{q})$ is shown at $\lambda = 0.53$ and $\lambda/W = 0.592$, respectively, for fixed $U/W = 0.5$ and a 24×24 system. The coherence length for various values of λ, at fixed $U/W = 0.5$, for system sizes 8×8, 16×16, and 24×24 are in panel (d). The $N(\pi,\pi)$, $S(\pi,\pi)$, and $L(\pi,\pi)$ are in (e) for various values of λ, at fixed $U/W = 0.5$ and using a 24×24 cluster.

all the phases found in our numerical exact one-dimensional results, the main difference being having shifted boundaries, to be expected considering the different dimensionality and different many-body approximations. The only important difference is that our mean-field calculations do not capture the non-magnetic phase in strong coupling, because the lattice non-magnetic state can be written as a direct product of $J_{\text{eff}} = 0$ at each site i.e. ... $|J_{\text{eff}=0}\rangle_i \otimes |J_{\text{eff}=0}\rangle_{i+1} \otimes |J_{\text{eff}=0}\rangle_{i+2}$..., where each $J_{\text{eff}} = 0$ state in the LS coupling limit is a sum of Slater determinants. However, the excitonic condensate phase, the focus of the present chapter, is properly captured by Hartree-Fock and it is present even in a larger region of the phase diagram than in one dimension, hence giving us a good opportunity to discuss the BCS-BEC crossover in two-dimensional lattices. We confirmed that increasing λ the system transists from IC-SDW metal to excitonic insulator at intermediate U, by calculating single particle density-of-states (see Appendix B.5). It must be noted that the excitonic magnet, at large U, found in Hartree-Fock calculations cannot be described by condensation of triplons. In the intermediate U region, the band insulator is present at large λ with excitons as local objects and the band gap is larger than the binding energy of excitons. As λ decreases, the excitonic magnet emerges due to the condensation of these conventional excitons. The above described scenario can be captured in mean-field theory calculations leading to the exctionic condensate state, as discussed earlier [79, 80, 81].

To proceed with our discussion, we fix $U/W = 0.5$ ($W = 8t$) where the excitonic condensation is present in a narrow but finite range of spin-orbit coupling, while for smaller λ's the IC-SDW phase is present. Similar to our one-dimensional DMRG calculations, in two dimensions we found that inside the excitonic condensate region (at a fixed weak or intermediate U/W values), r_{coh} decreases on increasing λ, as shown in Fig. 3.7(d) depicting the BCS-BEC crossover. We have calculated r_{coh} for system sizes 8×8, 16×16, and 24×24. We found that in the BCS limit, r_{coh} increases as the system size increases and r_{coh} can reach values as high as $\approx 15.0a$ for the 24×24 lattice. This clearly supports our claim for the presence of the BCS state above the IC-SDW region, as in our DMRG chain calculations.

On the other hand, in the BEC limit, below the relativistic band insulator in the phase diagram, r_{coh} is $\mathcal{O}(0.1a)$, as shown in Fig. 3.7(d). Figure 3.7(e) displays $S(\pi, \pi)$ and $L(\pi, \pi)$, for $U/W = 0.5$, showing that only for a finite range of λ the antiferromagnetic ordering

develops. We also show the momentum distribution function of excitons $\Delta_{1/2}(\mathbf{q})$ at $\lambda/W = 0.53$ and $\lambda/W = 0.592$ in the BCS and BEC limits, respectively. In the BEC limit $\Delta(\mathbf{q})$ is much sharper near $\mathbf{q} = (\pi, \pi)$ than in the BCS limit, as expected because in BEC a larger ratio of excitons is expected at the condensation momentum than other momenta. To further investigate the above claim we calculated the ratio of excitons at wavevector $\mathbf{q} = (\pi, \pi)$ and at other wavevectors using $N(\pi, \pi) = \Delta_{1/2}(\pi, \pi)/\langle\Delta_{1/2}(\mathbf{q} \neq (\pi, \pi))\rangle$, where $\langle\Delta_{1/2}(\mathbf{q} \neq (\pi, \pi))\rangle = \frac{1}{L^2-1}\sum_{\mathbf{q}\neq(\pi,\pi)} \Delta_{1/2}(\mathbf{q})$. It is evident from Fig. 3.7(e) that $N(\pi, \pi)$ increases as we transition from the BCS to the BEC limits.

3.5 Conclusions

In this chapter, we studied the degenerate t_{2g}^4 multiorbital Hubbard model in the presence of spin-orbit coupling, using one-dimensional chains and numerically exact DMRG and also using two-dimensional clusters within the Hartree-Fock approximation. In both calculations, we provide evidence for a BCS-BEC crossover in the spin-orbit excitonic condensate, in the regime of robust Hund coupling fixed as $J_H = U/4$. Within our accuracy, we established that in this model and at intermediate U/W, the system transits from an IC-SDW metallic phase to the BCS limit of an antiferromagnetic excitonic condensate. Further increasing λ the coherence length of electron-hole pairs decreases rapidly as the system crossovers to the BEC regime. This BEC regime ends as eventually the system transits to the relativistic band insulator on increasing further λ. Our work provides the first indications of a BCS-BEC crossover in the excitonic magnetic state at intermediate U/W, a region of couplings that cannot be explored within approximations developed in the large U/W regime.

We hope our results will encourage further theoretical and experimental investigations on t_{2g}^4 coumpounds with robust spin-orbit coupling. Although our study is performed using degenerate orbitals, we believe that our findings could be generic and relevant for materials showing magnetic excitonic condensation at intermediate values of the Hubbard repulsion and spin-orbit coupling. We believe that it will be also interesting and informative to investigate the dopings other than n=4, as many fractional filled 4d/5d transition metal oxides have also gained considerable interest in the last few years. To pursue this path, we

discuss the physics of fractionally filled , n=3.5, one-dimensional chains using DMRG in the next Chapter.

Chapter 4

Block Excitonic Condensate in a Spin-Orbit Coupled t_{2g} Multiorbital Hubbard Model

In the last decade, the $4d/5d$ transition metal oxides have received considerable attention in the Condensed Mater community, specially because they provide a unique platform for the development of unconventional magnetic and transport properties mainly as a consequence of a robust spin-orbit coupling [30, 31, 32, 33, 34, 35, 36, 37, 38, 46, 49]. One of the most interesting materials is Sr_2IrO_4 containing Ir^{4+} ions, with an electronic density $n = 5$ [39]. This compound displays similarities with La_2CuO_4, even with a relatively smaller Hubbard repulsion, because both exhibit long-range antiferromagnetic ordering in quasi two-dimensional layers [47, 48]. The realization of an effective layered half-filled Hubbard model in Sr_2IrO_4 is a result of a spin-orbit coupling λ close to 0.5 eV that splits the t_{2g} states into $j_{\text{eff}} = 1/2$ and $j_{\text{eff}} = 3/2$ sectors with a gap approximately equal to $3\lambda/2$. At $n = 5$ this leads to a half-filled $j_{\text{eff}} = 1/2$ band and concomitant Mott/Slater insulator behavior. Besides the iridates, other materials have also similarly interesting properties [45, 50, 51]. Even in the context of iron superconductors the importance of spin-orbit coupling has been remarked [58, 18, 61, 62].

Another interesting scenario which has been recently theoretically investigated led to the prediction of unusual magnetism in the $n = 4$ case [85, 56, 57, 64, 63, 65, 94]. At

this electronic density, *spin-orbit excitons* (for details see Sec. 4.2.1) were found to condense at momentum $q = \pi$, both in the intermediate and strong coupling limits, and also display antiferromagnetic staggered magnetic order. Experimentally, for double perovskite materials such as Sr_2YIrO_6 and Ba_2YIrO_6, with Ir^{5+} ions and a $5d^4$ configuration, the presence of the exciton condensate, as discussed time ago in semiconductors [79, 80, 81], has been debated [52, 55, 53, 54, 101]. Recent RIXS (resonant inelastic x-ray scattering) experiments on Sr_2YIrO_6 and Ba_2YIrO_6 have unveiled $J_{\text{eff}} = 1$ and $J_{\text{eff}} = 2$ excitations with weak dispersion at energies appproximately 0.37 eV and 0.7 eV [102], respectively, which suggests that the bandwidth of excitonic excitations is not sufficiently large when compared with λ to realize the predicted spin-orbit exciton condensate. It should be noted that these $J_{\text{eff}} = 1$ and $J_{\text{eff}} = 2$ excitations can be understood in terms of more conventional excitonic (electron-hole pair) states [79, 80, 81] between $j_{\text{eff}} = 3/2$ and $j_{\text{eff}} = 1/2$ sectors. Because in these excitations electrons jump from $j_{\text{eff}} = 3/2$ to $j_{\text{eff}} = 1/2$ states, the addition of angular momentum suggests that this will lead to $J_{\text{eff}} \in \{\frac{3}{2} - \frac{1}{2}, \frac{3}{2} + \frac{1}{2}\}$ i.e. $J_{\text{eff}} = 1$ or 2 excitations. In the layered Sr_2IrO_4 compound, these spin-orbit excitons are also present as stable excited states as shown by recent RIXS and optical conductivity measurements [40, 41, 42] [note that the notation J_{eff} is used for the total effective angular momentum of the system (or an atom), while j_{eff} refers for the effective angular momentum of single particle states. In the rest of the Chapter, we follow the same convention].

In addition to the above mentioned progress, it should be remarked that there are several real quasi-one dimensional materials with robust spin-orbit coupling strength that have been studied in the literature. The doped variants of the materials reported below may directly realize the physics discussed in this Chapter, because our calculations are based on numerically exact solutions of one-dimensional multiorbital models. For example, recently 1D stripes of Sr_2IrO_4 [43] were grown epitaxially and RIXS spectra have shown the presence of spin-orbit excitons at energies nearly 0.6 eV. Other examples of one-dimensional $j_{\text{eff}} = 1/2$ antiferromagnets includes $CaIrO_3$ [71, 114, 115, 116] and Ca_4IrO_6 [67, 117]. $BaIrO_3$ also belongs to the $5d^5$ class but have shown an unexpected charge-density wave [118, 119]. There are also mixed $3d$-$5d$ one-dimensional insulators, such as Ba_5CuIr_3O [120] and Sr_3CuIrO_6 [**?**, 121]. La_3OsO_7, which lies in the category of $5d^3$, is also a quasi-one-dimensional material

with antiferromagnetic ordering and $T_N = 45$ K [122]. There are also examples of quasi-one-dimensional materials with fractional valence states of the Ir and Rh ions, such as $Ba_5AlIr_2O_{11}$ [66, 123, 124], $Ca_5Ir_3O_{12}$ [125, 126], and $Sr_3Rh_4O_{12}$ [67]. $BaRu_6O_{12}$ and KRu_4O_8 are examples of quasi-one-dimensional ruthenates [127, 128] that have also attracted considerable attention. The combination of the existence of real quasi-one-dimensional $4d$ and $5d$ materials and our model studies employing numerically very accurate techniques provides a unique opportunity to explore and understand the phases which can emerge from the interplay of spin-orbit coupling, Coulomb electronic repulsion, and kinetic energy.

To obtain our results we use the numerically accurate density matrix renormalization group (DMRG) technique [129, 77] to solve the degenerate three-orbital Hubbard model in one-dimension. Up to now studies of the phases emerging in fractionally-filled three-orbital Hubbard models with spin-orbit coupling are relatively few, particularly as compared to the thoroughly investigated integer fillings, such as $n = 5$ and $n = 4$. To develop a conceptual understanding, here we used doping $n = 3.5$, i.e. 3.5 electrons per site in average, using a model with degenerate bands. Via DMRG calculations here we report the phase diagram varying λ and U. To our best knowledge, theoretical studies at this electronic doping have not been presented before.

The organization of this Chapter is as follows. In Sec. 4.1, the model used for our study is defined and the details of the computational method are explained. The main results are presented in Sec. 4.2, including the phase diagram varying U and λ. In particular, firstly we present the evidence for the novel block excitonic phase that we unveiled, and then we address the different magnetic phases present in the complete phase diagram, followed by a description of the density of states (DOS). In Sec. 4.3, we discuss our main results and present our conclusions.

4.1 Model and Method

In this manuscript, we use the three-orbital Hubbard model in the presence of spin-orbit coupling. The Hamiltonian contains a tight-binding term, an on-site Hubbard-Hund

interaction, and a spin-orbit coupling: $H = H_K + H_{\rm int} + H_{SOC}$. The tight-binding portion is

$$H_K = -\sum_{i,\sigma,\gamma,\gamma'} t_{\gamma\gamma'}(c^\dagger_{i\sigma\gamma}c_{i+1\sigma\gamma'} + \text{h.c.}) + \sum_{i,\sigma,\gamma}\Delta_\gamma n_{i\sigma\gamma}. \tag{4.1}$$

To gain conceptual understanding, we have focused on the simplest case of degenerate t_{2g} states, hence we fixed $t_{\gamma\gamma'} = t\delta_{\gamma\gamma'}$, where $t = 0.5$, and $\Delta_\gamma = 0$. This leads to a total bandwidth $(W) = 2.0$ eV in the non-interacting limit. The on-site Hubbard-Hund interaction and spin-orbit coupling (SOC) terms are already described in Chapter 2

In the non-interacting limit, both the SOC and tight-binding terms can be diagonalized simultaneously to obtain the following Hamiltonian:

$$H_K \; + \; H_{SOC} \;\; = \;\; \sum_{k,m}(2t\cos(k) \; - \; \frac{\lambda}{2})a^\dagger_{k,\frac{3}{2},m}a_{k,\frac{3}{2},m} \; + \; \sum_{k,m}(2t\cos(k) \; + \; \lambda)a^\dagger_{k,\frac{1}{2},m}a_{k,\frac{1}{2},m}. \tag{4.2}$$

Above we used $a^\dagger_{k,j_{\rm eff},m} = 1/\sqrt{L}\sum_l e^{-\imath lk}a^\dagger_{l,j_{\rm eff},m}$, where $a^\dagger_{l,j_{\rm eff},m}$ is the creation operator for an electron with total effective angular momentum $j_{\rm eff}$ and z-projection m. Equation (4.2) is useful to understand the non-interacting limit of the model. As λ is increased, the $j_{\rm eff} = 3/2$ and $j_{\rm eff} = 1/2$ bands split. For the doping $n = 3.5$ addressed in this study, in the large λ limit all electrons will be located in the $j_{\rm eff} = 3/2$ band, making the $j_{\rm eff} = 3/2$ band fractionally filled and the $j_{\rm eff} = 1/2$ band empty. This phase is called $j_{\rm eff} = 3/2$ metal. In Appendix C.2, we also present the local Coulomb interaction term expressed in the $j_{\rm eff}$ basis. Note that the global $U(1)$ symmetries, corresponding to the conservation of number of particles in the (j, m) states separately, are preserved only for $J_H = 0$ and $U = U'$. Thus, for the case of a finite Hund coupling, as investigated in the present Chapter, these $U(1)$ symmetries are explicitly broken leading to the possibility of long-range order in some channels.

Because our primary interest is to understand the subtle phases emerging from the competition of the Coulomb interaction, spin-orbit coupling, and kinetic energy, we used the DMRG technique which is numerically exact in one dimension. DMRG can treat the above three terms in the Hamiltonian on equal footing. We solved the above described model for various system lengths, such as $L = 8, 16, 24, 32$, and 48, fixing the average local density to $n = 3.5$. To reduce the cost of the simulations, we have targetted subspaces of

the total $J_z^{\text{eff}} = \sum_i (J_z^{\text{eff}})_i$, which is possible because $[H, J_z^{\text{eff}}] = 0$ for the chosen tight-binding parameters (for details see [94]). For the DMRG process, we used up to 1000 states and the corrected single-site DMRG algorithm [78] with correction $a = 0.001 - 0.008$. We performed 35 to 40 sweeps to gain proper convergence to the ground state properties. After convergence, we calculated the spin structure factor $S(q)$, local occupations $\langle n_{jm} \rangle$, local moments $\mathbf{S}_i^2$, $\mathbf{L}_i^2$, and $(\mathbf{J}_i^{\text{eff}})^2$, and also the exciton pair-pair correlation $\langle \Delta_{j\tilde{m}}^{\dagger \tilde{j}\tilde{m}'}(i) \Delta_{jm}^{\tilde{j}m'}(i') \rangle$ in order to construct the phase diagram. Moreover, we also used the DMRG correction vector method [106] with $L = 16$, as well as the Lanczos algorithm [9] with $L = 4$, to calculate the single-particle DOS.

4.2 Results

In Fig. 4.1, we show the phase diagram that we obtained varying U and λ in units of the non-interacting bandwidth W, at a fixed average local electronic density $n = 3.5$. The main result is the presence of a "block excitonic condensate", accompanied with block magnetic ordering (in a $\uparrow\uparrow\downarrow\downarrow$ pattern). We will discuss this novel phase, and other phases, in the following subsections. Also note that our study is in one dimension. For this reason when we express that in a range of U and λ we are located at a particular phase with particular characteristics, this always has to be interpreted in the sense of dominant power-law decaying correlations, as opposed to true long-range order. However, in the Appendix C.2 we show that the $U(1)$ phase characteristic of other excitonic condensates is explicitly broken in our calculation allowing for long-range order in the block exciton condensate regime to develop, compatible with the numerical results to be shown below.

Before discussing the results in detail, note that we expect the boundaries in the phase diagram Fig. 4.1 to correspond to first-order transitions if different symmetries are broken on both sides. In other words, at zero temperature we expect that each boundary between different symmetry breaking patterns corresponds to a level crossing. Computationally this could be tested by plotting the ground state energy varying for example U/W at constant SOC, using a grid of couplings very close to the transition. If a discontinuity

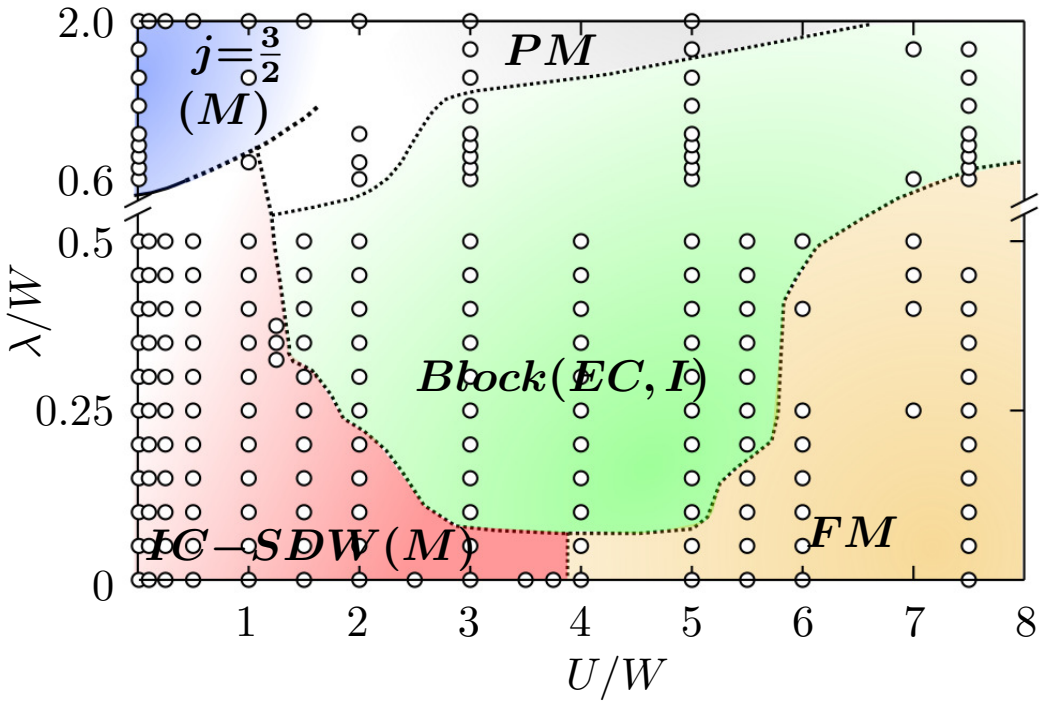

Figure 4.1: Shown is the main result of this Chapter, namely the λ - U phase diagram for $n = 3.5$, where $W = 2.0$ eV. The labels $IC - SDW$, $Block(EC)$, FM, and PM stand for Incommensurate Spin Density Wave, Block Excitonic Condensate, Ferromagnetic, and Paramagnetic phases, respectively. $j = 3/2$ is a metallic phase at large SOC where all electrons are in a $j = 3/2$ band, split from the $j = 1/2$ band that is empty. The labels M and I are used in the IC-SDW, Block EC, and j=3/2 phases to denote metal and insulator, respectively. For the other regimes we could not establish with certainty their metallic vs insulating character. The high density of points was achieved by using a system size $L = 16$ for the DMRG calculations, but several points in the phase diagram were obtained with $L = 32$ chains, as described for special cases below.

in the ground state energy first derivative is found at the transition, a first-order transition occurs. However, these calculations are very time consuming in our multi-orbital model, thus a confirmation of our expectation of first-order transitions is left for future work. Of course, if two regimes are merely separated by a crossover, then this crossover region resembles a continuous transition qualitatively.

4.2.1 Condensation of spin-orbit excitons

We now proceed to show and discuss the evidence of excitonic condensation in our phase diagram. We define the creation operator for an exciton at site i as $\Delta^{\dagger\tilde{j}m'}_{jm}(i) = a^{\dagger}_{ijm}a_{i\tilde{j}m'}$, where $j = 1/2$ and $\tilde{j} = 3/2$ are fixed. The exciton created by the above operator consists of a hole located at a $\tilde{j} = 3/2$ state with projection m' and an electron with $j = 1/2$ with projection m. These excitons are called "spin-orbit excitons" because the electron-hole pair is present in a spin-orbit entangled state. A similar excitonic operator was used before in [94, 64] to investigate the condensation of spin-orbit excitons for the $n = 4$ case. We would like to mention that the present work is the first study where the condensation of these excitons is shown to be stable for $n = 3.5$.

To investigate excitonic condensation we measure the real-space correlation between the excitons i.e. $\langle\Delta^{\dagger\tilde{j}\tilde{m}'}_{j\tilde{m}}(i)\Delta^{\tilde{j}m'}_{jm}(i')\rangle$. Here we would like to mention that earlier similar type of analysis was performed for one-dimensional systems to investigate quasi-excitonic condensations but in simpler models such as the extended Falicov-Kimball model [91].

For the spin-orbit excitons, as the quantum number m can take two values ($m = \pm 1/2$), this gives rise to two channels for excitonic condensation, namely the singlet and triplet channels [79, 80, 81, 83]. We define the exciton creation operators in both channels in the following manner:

$$\phi^{s}(i) = \sum_{m} \Delta^{\tilde{j}m\dagger}_{jm}(i), \tag{4.3}$$

$$\boldsymbol{\phi}^{t}(i) = \sum_{mm'} \Delta^{\tilde{j}m\dagger}_{jm'}(i)\boldsymbol{\tau}_{mm'}, \tag{4.4}$$

where $\boldsymbol{\tau}$ are the Pauli matrices.

In Fig. 4.2(a), we show the real-space correlations between the exciton pairs (with respect to the central site defined as $i' = 23$) for a system size $L = 48$, at $U/W = 4.0$ and $\lambda/W = 0.1$. In Fig. 4.2(a), we fix $m = 1/2$. Note the robust block ordering $[++--]$ that we found in the pair-pair correlation between excitons (see "$\tilde{m}' = \tilde{m} = m' = 1/2$", red line), consisting of holes and electrons with the same projection $j^{\text{eff}}_{z} = 1/2$. We also noticed

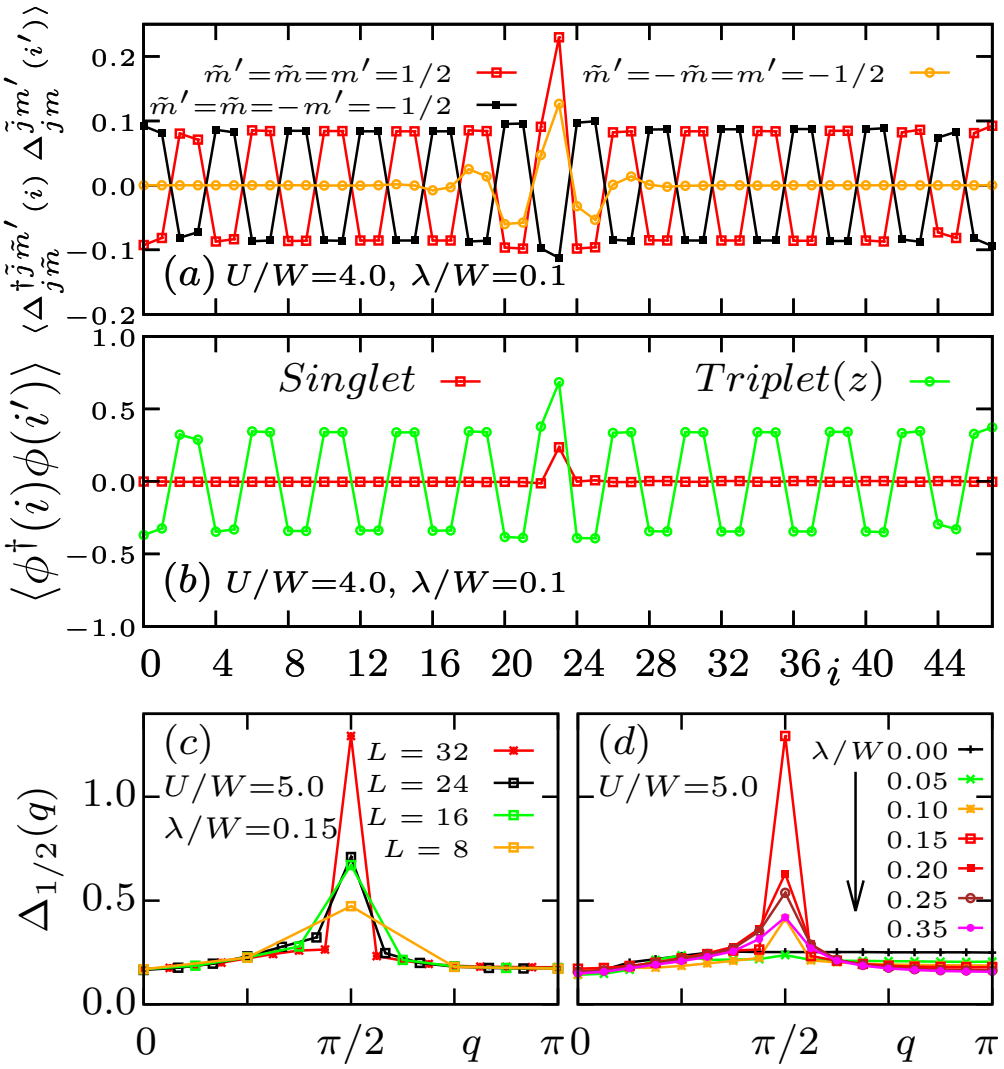

Figure 4.2: Panels (a,b) show the exciton-exciton correlation in real space, at $U/W = 4.0$ and $\lambda/W = 0.1$ using a $L = 48$ system size. For panels (a,b), $m = 1/2$ and i'=23 (in the middle of a chain with open boundary conditions) are fixed. Panel (c) shows the momentum distribution function for excitons at $U/W = 5.0$ and $\lambda/W = 0.15$. Similar momentum distribution functions of excitons for various λ's are shown in panel (d). A system size $L = 32$ is used for panel (d).

the presence of very long distance correlations between excitons of opposite projections (see "$\tilde{m}' = \tilde{m} = -m' = -1/2$" in Fig. 4.2(a), black line), i.e. one exciton consists of a hole and electron pair with projection $j_z^{\text{eff}} = 1/2$ and the other exciton is made up of a hole and electron with projection $j_z^{\text{eff}} = -1/2$. Note that the above discussed excitonic

correlations will contribute to both the singlet and the z component of the triplet channels. Similarly, we can create excitons consisting of electron ($j_z^{\text{eff}} = 1/2$) and hole ($j_z^{\text{eff}} = -1/2$) with different projections: the correlations between these excitons are shown in Fig. 4.2(a) (see "$\tilde{m}' = -\tilde{m} = m' = -1/2$", orange line) and they display a rapid exponential decay. These excitonic correlations contribute to the x and y components of the triplet channel.

Using the above information and Eqs.(4.3,4.4), we calculate the real-space correlations for the excitons in the singlet and triplet channels (z component). As shown in Fig. 4.2(b), clearly the triplet channel is the dominant showing quasi long-range order (likely a very slow power-law decay in our finite one dimensional system). As discussed before, the x and y components of the triplet channel have exponential decay. This asymmetry between the x, y, and z components is just a consequence of targeting the total J_z^{eff} sector in our DMRG simulations. For the one-dimensional case studied here, long range correlations (slow power-law decays) is used as evidence for excitonic condensation. For a simpler two-band models, early work [79, 80, 81] showed that condensation of excitons in the triplet channel leads to a spin-density wave and in the singlet channel leads, instead, to a charge-density wave.

Surprisingly, we also observed block magnetic ordering in the excitonic condensate phase reported here, which will be discussed in detail in Sec. 4.2.2. The dominating correlations in the z direction of the triplet channel implies that the relevant excitons are created by pairing electron and holes with the same j_z^{eff}, and from now on we will focus only on these excitons.

The momentum distribution function for excitons is $\Delta_m(q) = \frac{1}{L}\sum_{i,i'}\langle\Delta_{jm}^{\dagger\tilde{j}m}(i)\Delta_{jm}^{\tilde{j}m}(i')\rangle e^{\iota q(i-i')}$. This quantity provides an indication of the number of excitons (with projection m) at momentum q. In Fig. 4.2(d) we show $\Delta_m(q)$ for $U/W = 5$ and various λ's. For spin-orbit coupling strength $\lambda/W \lessapprox 0.07$, in the ferromagnetic region (to be discussed in more detail in the next subsection), the momentum distribution function is nearly flat. But at larger spin-orbit coupling, excitons condense at momentum $\pi/2$ and on further increasing λ, the number of excitons at $q = \pi/2$ again decreases, as shown in Fig. 4.2(d). The spin-orbit coupling strength for this crossover from the ferromagnetic phase to the block-excitonic condensate depends on the strength of U. We noticed the interesting feature (see phase diagram in Fig.(4.1)) that for $U/W \gtrapprox 5$, a larger U needs a larger λ for the condensation to occur. We also found $\pi/2$ order in the excitonic correlations above the IC-SDW region,

as shown in the phase diagram of Fig. 1, contrary to the strong coupling region, where increasing U needs smaller a λ for stabilizing the block-excitonic condensate.

We also show the finite-size scaling of the excitonic momentum distribution function in Fig. 4.2(c), for system sizes $L = 8, 16, 24$, and 32. The nearly linear growth of $\Delta_{1/2}(q = \pi/2)$ with the system size (L) again suggests the presence of a robust excitonic condensation. Long-range order is possible because the $U(1)$ symmetry is explicitly broken in the model, as discussed in the Appendix C.2.

4.2.2 Magnetic ordering

In this subsection, we will discuss and show the evidence for the different types of magnetic orderings found in the phase diagram. To investigate the various magnetic orderings, we calculate the spin-spin correlation $\langle \mathbf{S}_i \cdot \mathbf{S}_j \rangle$, and associated spin structure factor $S(q) = \frac{1}{L}\sum_{i,j}\langle \mathbf{S}_i \cdot \mathbf{S}_j \rangle e^{\iota(i-j)q}$. We also calculated the averaged local moments, $\langle \mathbf{S}^2 \rangle = \frac{1}{L}\sum_i \langle \mathbf{S}_i^2 \rangle$. Similarly we calculated $\langle \mathbf{L}^2 \rangle$, $\langle (\mathbf{J}^{\text{eff}})^2 \rangle$, and $\langle \mathbf{L} \cdot \mathbf{S} \rangle$. To evaluate the angle between the average local spin and average local orbital moment, i.e. ϕ_{LS}, we used $\phi_{LS} = cos^{-1}(\frac{\langle \mathbf{L}\cdot\mathbf{S} \rangle}{\langle l \rangle \langle s \rangle})$, where $\langle l \rangle(\langle l \rangle + 1) = \langle \mathbf{L}^2 \rangle$, and $\langle s \rangle(\langle s \rangle + 1) = \langle \mathbf{S}^2 \rangle$.

For $U/W \lessapprox 3.5$, we found that the IC-SDW region is smoothly connected to the non-interacting limit. In this region (red region in Fig. 4.1) the local moments gradually form up to the saturated values $\langle \mathbf{S}_i^2 \rangle = 2.875$ and $\langle \mathbf{L}_i^2 \rangle = 1$ as we increase U/W. Eventually this IC-SDW phase crossovers to the ferromagnetic (FM) phase. We noticed that in this IC-SDW region, the spin-ordering vector continuously changes depending on the values of U and λ, as shown in Appendix C.3, which we believe is the result of Fermi surface renormalization by the combined effect of U and λ. In Fig. 4.3(a), we show the real-space spin-spin correlation for $U/W = 3$ and $\lambda/W = 0$ depicting the incommensurate order, for a system size $L = 32$. By increasing λ, we found the block magnetic ordering phase above this IC-SDW region, but only as long as $U/W \gtrapprox 1.0$, as shown in the phase diagram Fig. 4.1. This block magnetic order survives up to $\lambda/W \approx 1$. In Fig. 4.3(b), we display the spin structure factor $S(q)$ for $U/W = 3$ for various λ/W's depicting the clear transition from IC-SDW to block magnetic

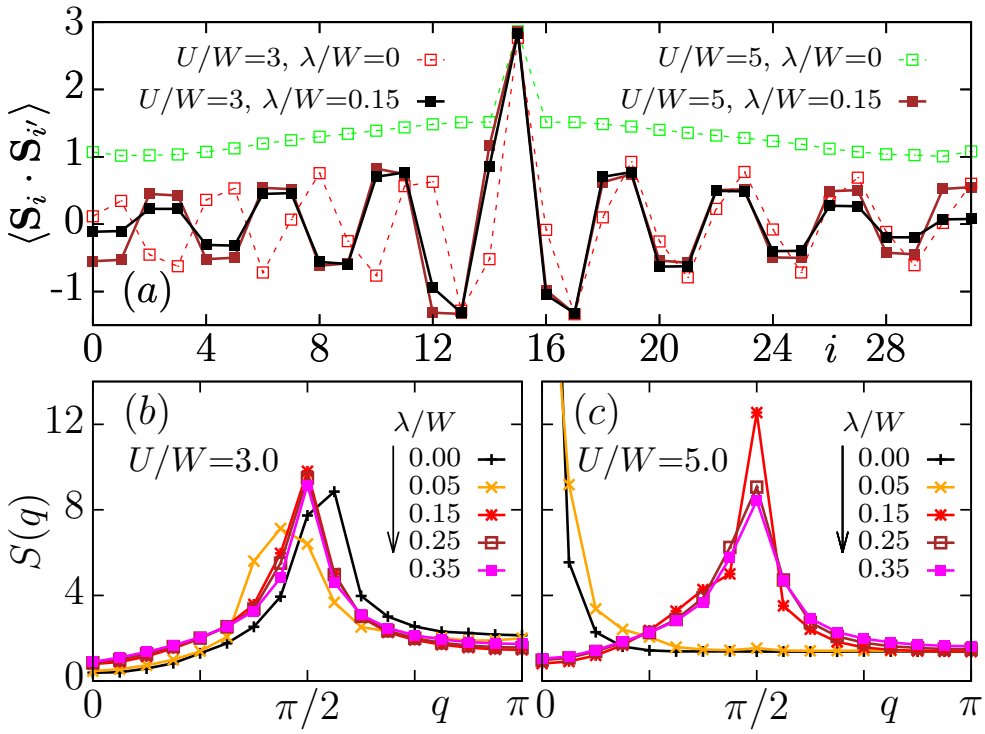

Figure 4.3: In panel (a) the real-space spin-spin correlations are shown for $U/W = 3$ and $U/W = 5$, and for $\lambda/W = 0$ and $\lambda/W = 0.15$. In panels (b) and (c), the spin structure factor $S(q)$ is shown for $U/W = 3$ and $U/W = 5$, respectively, and for various values of λ/W, as indicated.

order. We also show the real-space spin-spin correlation at $U/W = 3$ and $\lambda/W = 0.15$ in Fig. 4.3(a), portraying the block magnetic order ($\uparrow\uparrow\downarrow\downarrow\uparrow\uparrow$).

As shown in Fig. 4.1, for $\lambda/W = 0$ the above mentioned IC-SDW phase is directly connected to the ferromagnetic (FM) region in the strong coupling limit; this transition happens approximately at $U/W \approx 3.9$. In this FM phase, the local spin and orbital moments are fully saturated. The saturated values of the moments can be understood by considering the two-sites case in the large U limit. As we are interested in density $n = 3.5$, in the large U limit the main contribution to the two-sites ground state will arise from the d^3-d^4 configuration. The d^3 site will have local $\langle \mathbf{S}^2 \rangle = \frac{3}{2}(\frac{3}{2}+1) = 3.75$, while the d^4 site will have local $\langle \mathbf{S}^2 \rangle = 2$, leading to an average 2.875. Similarly the average local moment $\langle \mathbf{L}^2 \rangle = 1$ arises from $\langle \mathbf{L}^2 \rangle = 0$ (for d^3) and $\langle \mathbf{L}^2 \rangle = 2$ (for d^4).

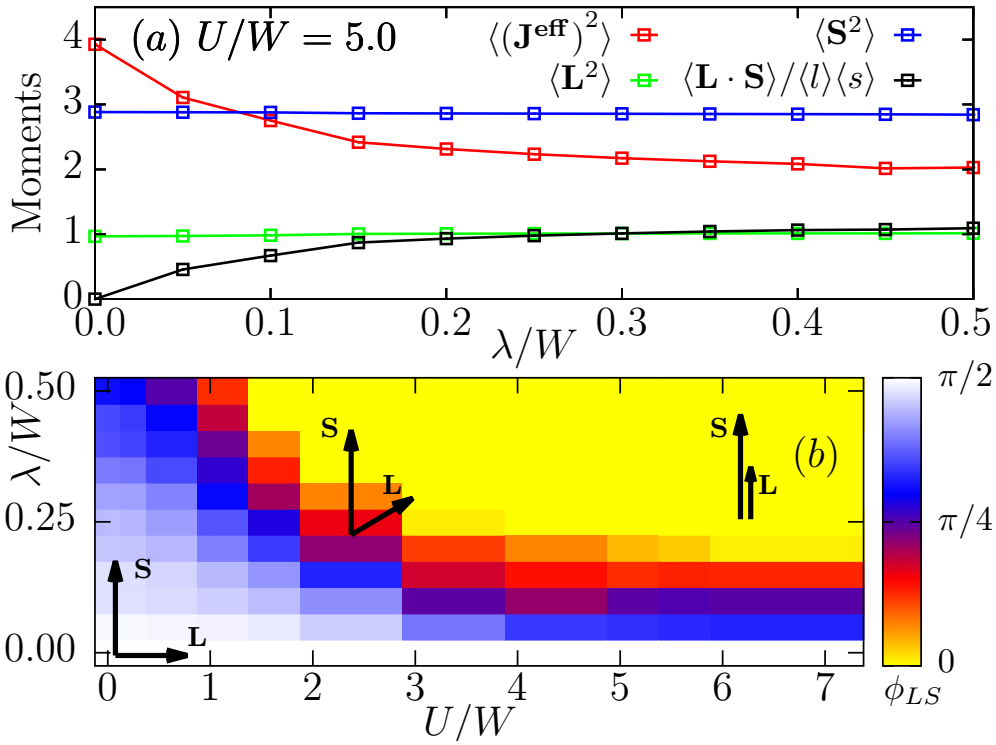

Figure 4.4: (a) Average local moments and $\langle \mathbf{L} \cdot \mathbf{S} \rangle / \langle l \rangle \langle s \rangle$ for $U/W = 5$, shown for various λ/Ws. In panel (b), ϕ_{LS} is presented for several λ/W's and U/W's, where the color depicts the value of ϕ_{LS} as shown in the side panel scale.

As we increase λ in this FM phase, the system eventually transitions to the block magnetic ordering. In Fig. 4.3(a), we show the real-space spin-spin correlations for $U/W = 5.0$ and $\lambda/W = 0.0$, and for $U/W = 5.0$ and $\lambda/W = 0.15$, as evidence of the ferromagnetic and block magnetic orders, respectively. The spin structure factors for $U/W = 5.0$ are shown in Fig. 4.3(c) for various $\lambda's$, depicting the crossover from the ferromagnetic to the block magnetic ordered phases. As discussed in Sec. 4.2.1, we suspect this block magnetic ordered phase is related with the condensation of spin-orbit excitons at momentum $q = \pi/2$. Note that for all the points shown in Fig. 4.1 in the block exciton condensate region (green region in the phase diagram of Fig. 4.1), we found block magnetic ordering and condensation of excitons at $q = \pi/2$. We also noticed that, as we increase λ, gradually $\Delta_{1/2}(q = \pi/2)$ decreases and the system transitions smoothly into a paramagnetic (PM) phase, with a

nearly flat spin structure factor. This PM phase is exotic because it is stabilized at large SOC and large U/W. Its properties will be studied in future work.

Now we turn our focus towards the effect of spin-orbit coupling on the local moments. In Fig. 4.4(a), we fixed $U/W = 5$, and on increasing λ we observed that the local $\langle \mathbf{S}^2 \rangle$ and $\langle \mathbf{L}^2 \rangle$ remain nearly 2.875 and 1.0, respectively. But although their magnitudes are nearly constant there is a substantial change in the relative orientation of the spin and orbital moments i.e. they gradually modify their relative angle from $\pi/2$ to 0. This rotation affects the local $\langle (\mathbf{J}^{\text{eff}})^2 \rangle$, which decreases as the spin and orbital moments become parallel. In Fig. 4.4, we show the average angle between the local spin and orbital moments. We notice that, as we increase U, smaller λ's are enough to render S and L parallel to each other. This indicates that *Coulomb interactions enhance the effect of spin-orbit coupling* and helps to entangle the spin and orbital moments. It is interesting to observe that the novel block excitonic phase we found lies in the region where L and S are parallel to each other with $\langle \mathbf{L} \cdot \mathbf{S} \rangle \approx \langle l \rangle \langle s \rangle \approx 0.8$. We would like to mention that $\langle \mathbf{L} \cdot \mathbf{S} \rangle$ is directly related to the branching ratio calculated by XAS (X-ray Absorption Spectroscopy) experiments for the materials where SOC is robust [70].

4.2.3 Local Densities and Density of States

In the last two subsections we established the presence of a novel block excitonic condensate, accompanied with block magnetic order. Now we will discuss the spin-orbit basis-resolved average local occupations $\langle n_{jm} \rangle = \frac{1}{L} \sum_i \langle n_{i,jm} \rangle$ using a $L = 16$ sites system. We also calculate the DOS ($\rho_{jm}(\omega - \mu)$) on a 4-site chain using Lanczos [9], and on a $L = 16$ system using the DMRG correction vector method [106], where μ is the chemical potential evaluated via $(E(N+1) - E(N-1))/2$ for a system with N electrons. In particular, we used the DMRG++ computer program [130] and the Krylov formulation [107] for the DMRG correction vector method [106].

In Fig. 4.5, we show the effect of spin-orbit coupling on the average local occupations $\langle n_{jm} \rangle$ for three different U values i.e. $U/W = 0.01$, $U/W = 3.0$, and $U/W = 5.0$. Before

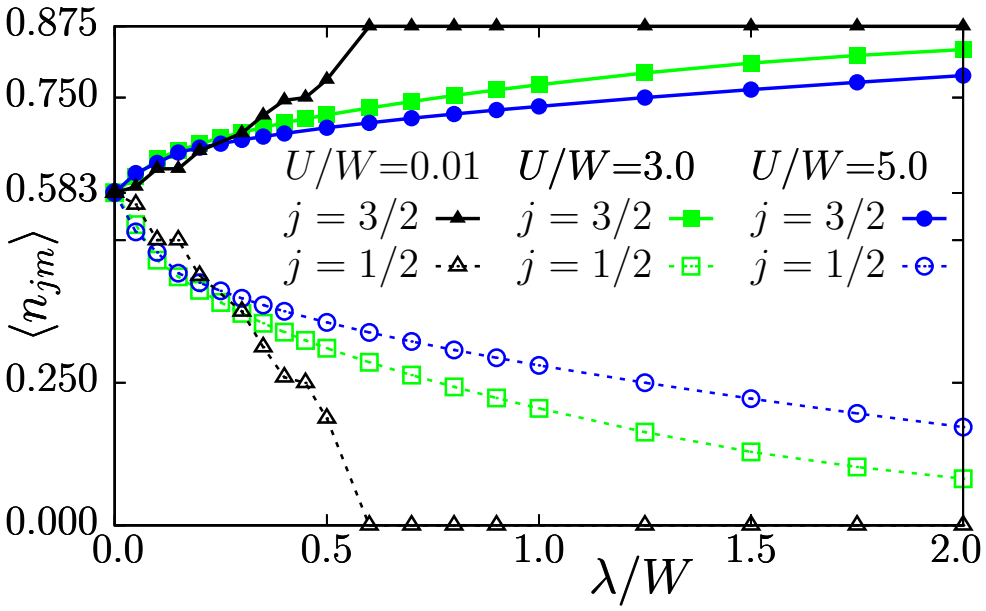

Figure 4.5: Average local occupations $\langle n_{jm} \rangle$ shown for $U/W = 0.01$, $U/W = 3.0$, and $U/W = 5.0$, with increasing λ/W. For $j = 1/2$ and $j = 3/2$, m can be $\{\pm 1/2\}$ and $\{\pm 1/2, \pm 3/2\}$, respectively.

explaining the results we would like to mention that the occupations in the t_{2g} orbital basis for any λ and U are found to be same i.e. $\langle n_{\sigma\alpha} \rangle \approx 0.5833$, which is consequence of using degenerate orbitals in the kinetic energy term, and Coulomb interaction and spin-orbital coupling that do not break this symmetry in the t_{2g} orbitals. The "good" basis for systems in the presence of spin-orbit coupling (in non-interating limit) is provided by the j, m states, thus it is reasonable to discuss the occupation in terms of $\langle n_{jm} \rangle$. For small values of Coulomb interaction, such as $U/W = 0.01$, we clearly reproduce the physics of the non-interacting limit. For $\lambda = 0$ we found $\langle n_{jm} \rangle \approx 0.5833$ and as we increase λ the system transitions to a $j_{\text{eff}} = 3/2$ metallic regime where the low-energy $j_{\text{eff}} = 3/2$ band is fractionally filled with $\langle n_{3/2m} \rangle = 0.875$ electrons per site, and the higher energy band $j_{\text{eff}} = 1/2$ is empty. At larger U/W values, this $j_{\text{eff}} = 3/2$ metallic phase is pushed towards larger λ. As also shown in Fig. 4.5, that for $U/W = 3$ and $U/W = 5$ we do not find a $j_{\text{eff}} = 3/2$ metal for λ/W as large as 2.0. This explains the curvature of the lower boundary of the $j_{\text{eff}} = 3/2$ metal in the phase diagram Fig. 4.1. To confirm these results, we also calculated the local occupations

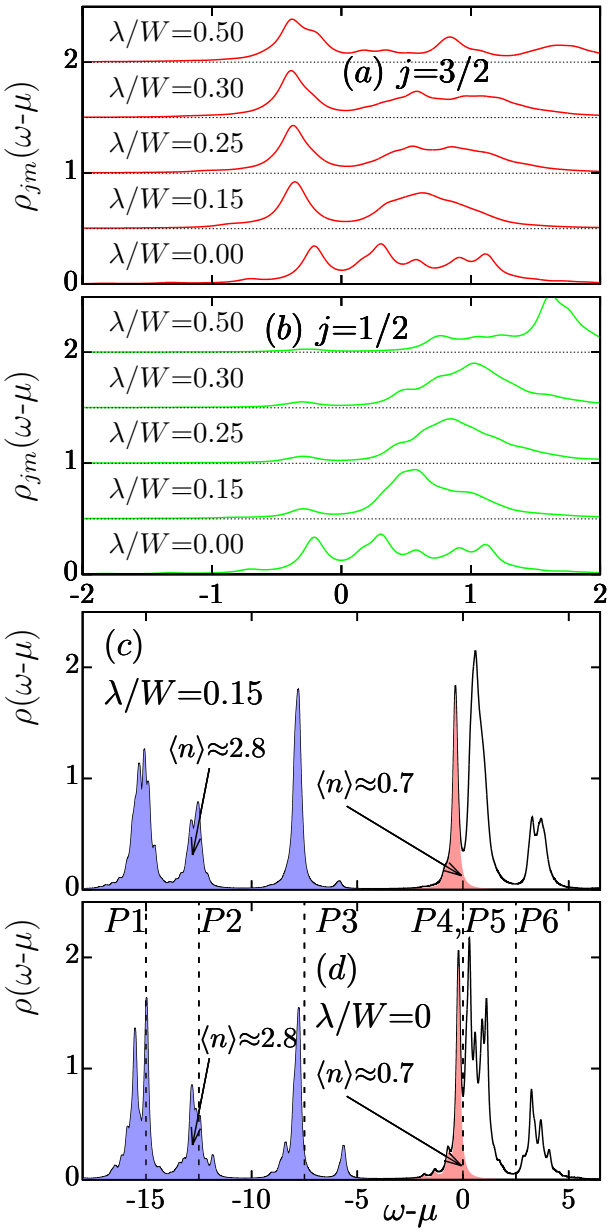

Figure 4.6: Density of states, $\rho_{jm}(\omega-\mu)$, near μ shown for various values of λ/W, and at $j_{\text{eff}} = 3/2$ and $j_{\text{eff}} = 1/2$ in panels (a) and (b), respectively. In panels (c) and (d), the total $\rho(\omega-\mu)$ is shown for $\lambda/W = 0.15$ and $\lambda/W = 0$, respectively. All the above results are calculated for a $L = 4$ (OBC) site cluster using Lanczos at $U/W = 5.0$. A broadening $\eta = 0.1$ was used for all the results above. For $j = 1/2$ and $j = 3/2$, m can be $\{\pm 1/2\}$ and $\{\pm 1/2, \pm 3/2\}$, respectively.

for different U/W's at a fixed $\lambda/W = 2.0$, and found that increasing U gradually increases the filling in the $j_{\text{eff}} = 1/2$ state.

Now let us discuss the DOS calculated using the Lanczos method employing a four-site cluster with open boundary conditions. We checked that even using such a small four-site system, we obtain the same phases as in the phase diagram Fig. 4.1. Firstly, let us discuss the total DOS $\rho(\omega - \mu) = \sum_{jm} \rho_{jm}(\omega - \mu)$ for $\lambda = 0$, as shown in Fig. 4.6(d) for $U/W = 5.0$ where we have a FM ground state. We noticed that away from the chemical potential we have four dominant peaks, named $P1$, $P2$, $P3$, and $P6$. These single-particle excitations can be understood in the strong coupling limit using a two-site cluster, as explained in Appendix C.1. The interesting feature is the presence of a metallic band near the chemical potential: in the two-site limit this band consists only of two single-particle excitations $P4$ and $P5$. This metallic band in the strong coupling limit, Appendix C.1, contains nearly 0.5 itinerant electrons per site, which are moving in the ferromagnetic background of the other electrons, and leads to a FM metal. For $U/W = 5$, the occupied part of this metallic band is made of nearly 0.7 electrons per site.

Let us investigate the effect of λ on the density of states. In Fig. 4.6(c), we show $\rho(\omega - \mu)$ for $U/W = 5$ and $\lambda/W = 0.15$. At these couplings our Lanczos results show block magnetic order (with block excitonic order). We noticed that the positions of the peaks away from μ are not changed much, but the DOS at μ decreases with a tendency to open a gap as we move into the block excitonic phase. To explore this issue further, we calculated the j, m-resolved DOS $\rho_{jm}(\omega - \mu)$ near the chemical potential for different λ/W values, as shown in Figs. 4.6(a,b). For both $j_{\text{eff}} = 3/2$ and $1/2$, note that with increasing λ/W the DOS near μ decreases with the split in the metallic band. But for $j_{\text{eff}} = 1/2$, the DOS below μ gradually decreases to 0, because in the limit of very large λ/W the $j_{\text{eff}} = 1/2$ states will be empty. It should be also noted that for $\lambda/W = 0.5$, we already see the emergence of states near the chemical potential for $j_{\text{eff}} = 3/2$, with the system moving towards the paramagnetic phase. From the above exact analysis of the four-site system, we can conclude that there is a clear tendency towards the opening of a gap in the block phase, thus a clear tendency to form an insulator.

To confirm that the above described results persists for larger systems, we also calculated $\rho_{jm}(\omega-\mu)$ near the chemical potential using the DMRG vector correction method for a $L=16$ site system. We again fixed $U/W=5$ and focused on $\lambda/W=0$ and $\lambda/W=0.15$, which shows ferromagnetic and block magnetic ordering, respectively, as discussed in Sec. 4.2.2. We noted that the metallic band is clearly present in the ferromagnetic phase, see Fig. 4.7(b). This suggests that indeed there is a fraction of electrons that develop a metallic band, having other localized electrons create a ferromagnetic background with spins $S\approx 3/2$. If now we increase λ/W to 0.15, driving the system towards the block excitonic phase, both the $j_{\text{eff}}=3/2$ and $1/2$ sectors show a tendency to open a gap and being insulating. These results further confirm the understanding deduced from the small $L=4$ exact result. To establish the insulating nature of the block excitonic phase, we calculated the single-particle charge gap $\Delta_c = E_{N+1}+E_{N-1}-2E_N$, where N is the total number of electrons. We performed finite-size scaling of the gap Δ_c using various system sizes between $L=8$ and $L=44$. As shown in the inset of Fig. 4.7(a), we noticed that $\lim_{L\to\infty}\Delta_c(L)$ converges approximately to 0.1 eV.

The novel block phase shown in this Chapter resembles the block magnetic order phase reported earlier in the context of three-orbital Hubbard models. In fact, block magnetic ordering, without the excitonic condensate component, has been found previously in models without spin-orbit coupling, in the context of the Orbital Selective Mott Phase (OSMP) [5, 25, 26, 27, 110]. In the latter, two orbitals are metallic with fractional filling and one orbital is insulating with half-filling. However, note that the block phase discussed in this Chapter is *not* accompanied by an OSMP phase, as indicated by the average local occupations. Instead the novel block phase discussed here is accompanied by the condensation of spin-orbit excitons at momentum $q=\pi/2$ for which a finite spin-orbit coupling is a necessary condition.

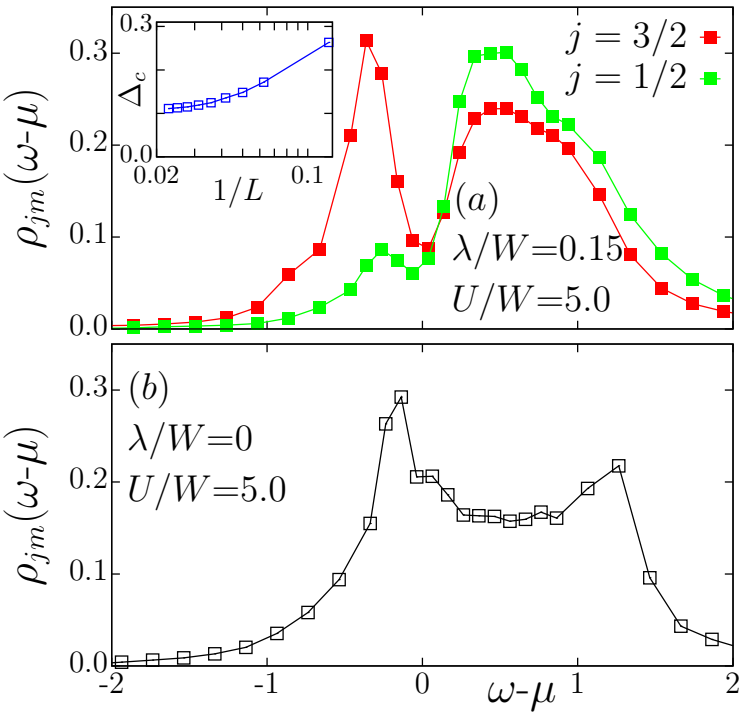

Figure 4.7: Density of states, $\rho_{jm}(\omega - \mu)$, shown for a $L = 16$ site system at $\lambda/W = 0.15$ and $\lambda/W = 0$ in panels (a) and (b), respectively. The DMRG vector correction method is used to calculate these results. $U/W = 5.0$ and a broadening $\eta = 0.1$ are employed. The inset in panel (a) contains a finite-size scaling of the charge gap at $\lambda/W = 0.15$ and $U/W = 5.0$. For $j = 1/2$ and $j = 3/2$, m can be $\{\pm 1/2\}$ and $\{\pm 1/2, \pm 3/2\}$, respectively.

4.3 Conclusions

In this Chapter, we used an accurate numerical technique, DMRG, to construct the λ vs U phase diagram for the one-dimensional three-orbital Hubbard model at $n = 3.5$. As our main result, we provide the first numerical evidence for the condensation of spin-orbit excitons in the fractionally filled three-orbital Hubbard model. Our calculations show that the spin-orbit excitons condense in the triplet channel and at momentum $\pi/2$, for all the points shown inside the green region of the phase diagram displayed in Fig. 4.1. This quasi-condensation of excitons is accompanied by tendencies to open a gap at the chemical potential and also by block magnetic ordering. Interestingly, the block excitonic condensate unveiled here can be stabilized by introducing the spin-orbit coupling on both the IC-SDW and Ferromagnetic

metallic phases. We also noticed that in this novel block excitonic condensate phase, local spin and orbital moments are highly entangled and nearly parallel to each other.

We believe the results reported in this chapter – which are unique given the considerable computational effort needed that requires vast computational resources – will encourage further theoretical and experimental investigations on fractionally-filled iridates [131, 132, 133, 134, 135] and also on other quasi-one dimensional materials with large spin-orbit coupling. While our model calculations cannot establish which precise material will realize the novel phase unveiled, we believe from now on the block condensate has to be considered among the candidate states when $n = 3.5$ materials are studied.

In this chapter we have shown a novel way to stabilize exotic block magnetic ordering in presence of robust spin orbit coupling. The block magnetic ordering up to this point was only discussed in the context of low-dimensional iron based supercounductors, accompanied with orbital-selective Mott phase. In the next chapter, we will discuss the spin dynamics on this block orbital-selective Mott phase.

Chapter 5

Spin dynamics of the block orbital-selective Mott phase

5.1 Introduction

Inelastic neutron scattering (INS) measurements are crucial for the study of quantum magnetism in condensed matter physics. This powerful experimental technique provides detailed information of momentum and energy resolved spin excitations. The importance of INS studies is best illustrated in the case of high critical temperature superconductors. Shortly after the discovery of the copper-oxide compounds it became evident that the standard BCS theory of the electron-phonon coupling could not explain the experimental findings. Simultaneously, INS results showed that superconductivity appears in close proximity to the antiferromagnetic (AFM) ordering of $S = 1/2$ Cu^{2+} moments providing robust evidence that the new pairing mechanism is based on spin fluctuations [136, 60, 137, 9].

The discovery of iron-based superconductors (FeSC) added an extra complication to this "simple" picture. Although the phase diagrams of Cu-based and Fe-based materials are qualitatively similar [138], there are important conceptual differences. The most significants are in the minimal models that describe the materials [105, 139]. While cuprates have a single Fermi surface (FS), the iron-based compounds have a complicated FS with electron and hole pockets originating in the five $3d$ orbitals of iron. As a consequence, the FeSC have to be described by means of multi-orbital Hubbard models, involving not only a standard Hubbard

U repulsion but also a Hund coupling. The competition between electronic, orbital, and spin degrees of freedom can lead to many exotic magnetic phases [140, 141, 18, 142, 143, 144].

Past experience in cuprates showed that the analysis of lower dimensional systems, such as chains and ladders, can provide useful information to better contrast theory with experiments [145]. One reason is that theoretical many-body calculations based on model Hamiltonians can be accurately performed in one dimension, particularly numerically. For this reason, it was exciting when a one-dimensional family of compounds containing two-leg ladders was unveiled also in the iron-superconductors context. Specifically, we refer to the low-dimensional FeSC in the 123 family, $A\mathrm{Fe_2X_3}$, where A are alkali metals A=K, Ba, Rb, Cs, and X are chalcogenides X=S, Se. These compounds are build of double chains (i.e. they are ladders) of edge sharing FeX_4 tetrahedra [146]. Recently, a superconducting state was identified under pressure for $\mathrm{BaFe_2S_3}$ [22, 147] and $\mathrm{BaFe_2Se_3}$ [148, 149]. The pressure-dependent phase diagram of these materials resembles that of copper-oxide ladders, e.g., the telephone number compound $\mathrm{Sr_{14-x}Ca_xCu_{24}O_{41}}$ [15]. Similar to their copper oxide counterparts, the iron-123 family is insulating at ambient pressure. This behavior is unusual since, unlike the cuprates, the parent compounds of FeSC are typically bad metals. In addition, it was argued that orbital-selective Mott physics (OSMP) [150] is consistent with results for $\mathrm{BaFe_2Se_3}$ [151, 5, 152, 4]. Within such a phase, itinerant and localized conduction electrons coexist.

It should be remarked that INS experiments on 123 materials have been performed up to now only on powder samples and, as a consequence, detailed data of the momentum dependence of the spin excitations over the whole Brillouin zone is not yet available. Nevertheless, the static $(\pi, 0)$ stripe AFM order – with ferromagnetic rungs and antiferromagnetic legs – was identified for $\mathrm{BaFe_2S_3}$ [153], $\mathrm{RbFe_2Se_3}$ [154], $\mathrm{CsFe_2Se_3}$ [155, 156], and also for $\mathrm{KFe_2S_3}$ [151]. However, in the special case of $\mathrm{BaFe_2Se_3}$ remarkably an exotic block magnetism was found [157, 151, 2, 4, 149] involving antiferromagnetically coupled ferromagnetic islands made of 2×2 iron clusters. This unusual magnetic state was also observed in the vicinity of superconductivity [158, 159, 160] in two-dimensional (2D) materials with $\sqrt{5} \times \sqrt{5}$ ordered iron vacancies, such as $\mathrm{Rb_{0.89}Fe_{1.58}Se_2}$ [161] and $\mathrm{K_{0.8}Fe_{1.6}Se_2}$ [162, 163, 164]. In addition,

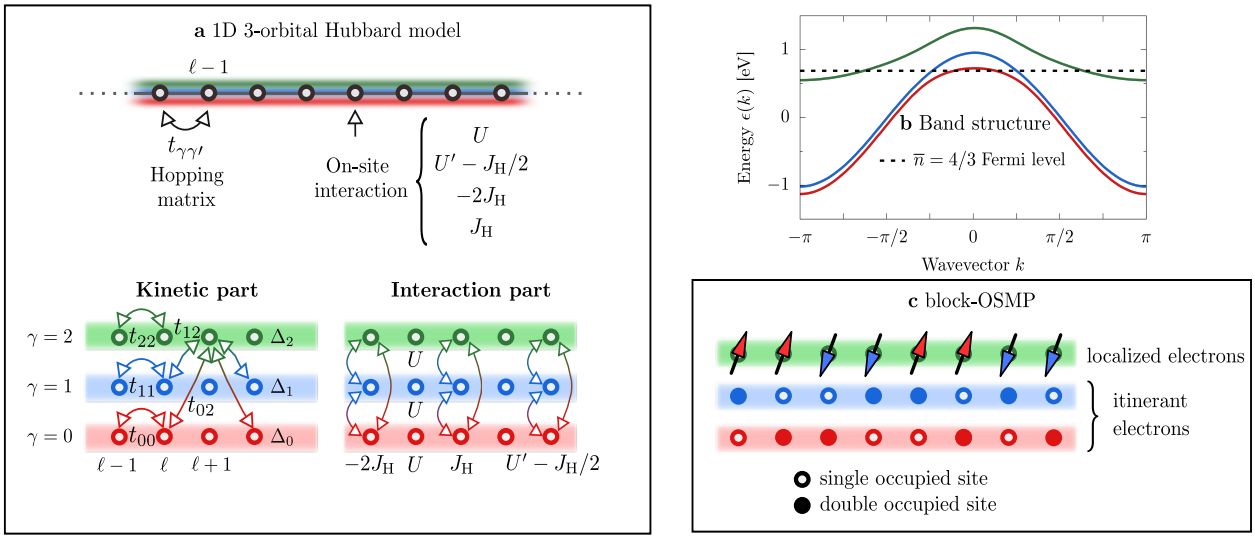

Figure 5.1: Schematic representation of the Hamiltonian. (a) Three-orbital Hubbard model on a one-dimensional lattice geometry (see text for details). (b) Band structure of Hamiltonian Eq. (5.1). Note that due to the hybridization $t_{\gamma\gamma'} \neq 0$ for $\gamma \neq \gamma'$, the band numbers do not correspond directly to the orbital numbers. (c) Schematic representation of the block orbital selective Mott phase. The pattern of single and double occupied sites in the itinerant electrons is meant to be random, representing pictorially the not-localized nature of those orbitals.

for $BaFe_2Se_3$ [4], $BaFe_2S_3$ [153], and $RbFe_2Se_3$ [154] the INS revealed the existence of low-energy acoustic and high-energy optical modes separated by an energy gap. It is important to remark that the generic features of the INS spectra of the aforementioned compounds are similar, but the physical origin of the acoustic modes can differ significantly - these modes reflect on the long-distance properties of the magnetic order in the system. Moreover, the origin and characteristics of the optical modes, that are induced by short-distance properties, have not been clarified so far.

In this Chapter, we will address the spin dynamical properties of the exotic block magnetic state found in $BaFe_2Se_3$. The static (time independent) properties of this phase were previously qualitatively studied in Ref. [5] via a three-orbital Hubbard model in one-dimension (1D) that unveiled an OSMP regime. Here, we will use the same Hamiltonian to investigate the momentum and energy resolved spin dynamics. To test the general features of our findings we present also results obtained in a quasi-1D ladder geometry. In agreement

with experimental findings we have observed two distinct modes of spin excitations: a low-energy dispersive mode and high-energy dispersionless optical modes. The low-energy acoustic mode reveals the frustrated nature of the block magnetism which can be described by a spin J_1-J_2 Hamiltonian. On the other hand, we argue that the optical mode is controlled by local orbital physics and it cannot be properly captured by a Heisenberg-like model. The main features of our analysis are simple and generic and should characterize any multi-orbital model as long as its ground state is in a magnetic block phase.

5.2 Results

Model and observables. We will focus on a specific three-orbital Hubbard model on a one-dimensional lattice, but our conclusions are generic for a broad group of models and materials in the OSMP magnetic block-phase regime. As mentioned before, the model chosen was previously studied with regards to its time-independent properties, and it is known that it displays an OSMP regime in the ground state [5]. The kinetic part of the Hamiltonian, $H_{\rm kin}$, is defined as:

$$H_{\rm kin} = -\sum_{\ell,\sigma,\gamma,\gamma'} t_{\gamma\gamma'} \left(c^{\dagger}_{\ell,\gamma,\sigma} c_{\ell+1,\gamma',\sigma} + \text{H.c.} \right) + \sum_{\ell,\gamma,\sigma} \Delta_{\gamma} n_{\ell,\gamma,\sigma} \,, \tag{5.1}$$

where $c^{\dagger}_{\ell,\gamma,\sigma}$ creates an electron with spin $\sigma = \{\uparrow,\downarrow\}$ at orbital $\gamma = \{0,1,2\}$ and site $\ell = \{1,\ldots,L\}$ of a 1D chain. $n_{\ell,\gamma,\sigma} = c^{\dagger}_{\ell,\gamma,\sigma} c_{\ell,\sigma,\gamma}$ is the local (ℓ,γ) electron density with spin σ. Note that another common labeling of these orbitals could be based on the canonical t_{2g} manifold, i.e. $\{yz\,, xz\,, xy\}$, respectively. $t_{\gamma\gamma'}$ denotes a symmetric hopping amplitude matrix defined in the orbital space γ: $t_{00} = t_{11} = -0.5$, $t_{22} = -0.15$, $t_{02} = t_{12} = 0.1$ and $t_{01} = 0$, all in eV units [Fig. 5.1(a) displays a schematic representation of the Hamiltonian]. The crystal-field splitting is set to $\Delta_0 = -0.1$, $\Delta_1 = 0$, and $\Delta_2 = 0.8$, also in eV units. The total kinetic-energy bandwidth is $W = 2.45\,\text{eV}$. These phenomenological values of parameters were chosen before [5] to reproduce qualitatively the band structure properties of higher dimensional selenides at an electronic density $\overline{n} = 4/3$ per orbital, namely an electron-like pocket at $k = 0$ and hole-like pockets at $k = \pm\pi$ (see Fig. 5.1(b), and also Ref. [24] and

references therein). It should be pointed out that the existence of an OSMP highlights the striking orbital sensitivity on electron correlations in multi-orbital Hubbard models, and its presence is not limited to our use of 1D geometries nor to our choice of $t_{\gamma\gamma'}$ hoppings. For example, the OSMP was proven to be relevant [165] for 2D alkaline iron selenides as well, with and without $\sqrt{5} \times \sqrt{5}$ ordered vacancies. We wish to emphasize that our predictions primarily depend on the existence of an OSMP magnetic block-phase state, rather than on the details of the Hamiltonian that leads to its stabilization. In this context, we believe that our results are universal for iron-based superconductors. To support this claim, we will present calculations for several models showing that all the many reported results lead essentially to the same qualitative conclusions.

The interaction portion of the Hamiltonian H_{int} is the same as discussed in the Chapter 2. We set the Hund coupling to $J_{\text{H}} = U/4$, a value widely used before and considered to be realistic for Fe-based materials [166, 167]. We refer the interested reader to Refs. [5, 25, 94] for details of the J_{H}-U phase diagram of the above Hamiltonian. Here, if not stated differently, we will use $U/W = 0.8$ where previous studies found [5] a block-OSMP , i.e. antiferromagnetically (AFM) coupled ferromagnetic (FM) blocks (magnetic unit cells), $\uparrow\uparrow\downarrow\downarrow\uparrow\uparrow\downarrow\downarrow$, in the localized orbital $\gamma = 2$ [see Fig. 5.1(c)]. Note that the block order is usually studied in the context of Heisenberg-like spin Hamiltonians (such as dimerized [4, 161] or J_1–J_2 models [168]). Here, the block phase is a consequence of nontrivial electronic correlations within the OSMP phase. Since the latter is a feature of multi-orbital systems that cannot be analyzed using purely spin systems, we believe that our setup is more suitable for the study of iron-based materials.

In this Chapter, we will investigate the zero-temperature frequency ω-dependent spin structure factor (SSF) $S(q, \omega)$, defined as the Fourier transform of the real-space total (on-site, $S_\ell = \sum_\gamma S_{\ell,\gamma}$) spin correlation functions (see Appendix D.1). Furthermore, we will study the contributions from the individual orbitals to the total SSF, i.e. $S_{\gamma\gamma'}(q, \omega)$. $\gamma = \gamma'$ denotes the spin fluctuations within each of the orbitals, while $\gamma \neq \gamma'$ are spin fluctuations between different orbitals. As a consequence $S(q, \omega) = \sum_\gamma S_{\gamma\gamma}(q, \omega) + \sum_{\gamma \neq \gamma'} S_{\gamma\gamma'}(q, \omega)$. From the experimental perspective, only the total SSF has a meaning [169] because neutrons

couple to electrons in all orbitals in neutron scattering experiments. However, the theoretical investigations of orbital-resolved SSF can provide further insight into the OSMP physics.

The Hamiltonians are diagonalized via the DMRG method, where the dynamical correlation functions are obtained with the help of dynamical DMRG techniques (see Appendix D for details of the numerical simulations).

Dynamical spin structure factor. In Fig. 5.2 we present one of the main results of our effort: the frequency-momentum dependence of the dynamical SSF in the block-OSMP phase (i.e. at $U/W = 0.8$). Panel (a) depicts the total SSF, $S(q,\omega)$, while panel (b) shows only the contribution from the localized orbital, $S_{22}(q,\omega)$. Several conclusions can be obtained directly from the presented results: (i) A robust contribution to the total SSF arises from the localized orbital. Moreover, all the qualitative features of $S(q,\omega)$ are already present in $S_{22}(q,\omega)$. In fact, $S(q,\omega)$ and $S_{22}(q,\omega)$ become almost indistinguishable if normalized by the local magnetic moment squared (i.e. $S^2 = 3/4$ for the $S = 1/2$ localized electron, and $S^2 = 2$ for the total moment [5]). (ii) The energy range for the spin dynamics is much smaller when compared with the energy bandwidth $W = 2.45\,\text{eV}$ of the Hamiltonian. (iii) Clearly the dynamical SSF has two distinct modes: a low-frequency, $\omega \lesssim \omega_c = 0.08\,\text{eV}$, dispersive (acoustic) band and a high-frequency, $\omega \sim 0.11\,\text{eV}$, dispersionless (optical) band. Similar results were previously reported experimentally in INS investigations of $BaFe_2Se_3$ [4] (with 2×2 FM blocks), $BaFe_2S_3$ [153] and $RbFe_2Se_3$ [154] (with 2×1 FM blocks). The different types of blocks in the INS investigations, and the similarity of results between neutrons and our calculations, suggest that our results apply to a broad variety of iron chalcogenides. Moreover, the INS measurements where performed on powder samples and, as a consequence, no detailed analysis of the spin excitations over all crystal momenta q (over the whole Brillouin zone) have been reported. In this respect, our results define clear theoretical predictions on what future single-crystal experiments should display.

In Fig. 5.3(a) we present the ω dependence of the total SSF at special values of the momenta q. It is evident that the acoustic mode is strongly momentum dependent in the range $0 < q/\pi \lesssim 1/2$, while it reduces drastically its intensity for $q/\pi > 1/2$. To understand these results, we can reanalyze the SSF spectrum using two-sites as a rigid block, namely creating an effective magnetic unit cell of FM-blocks with momentum $\widetilde{q}$. The acoustic mode

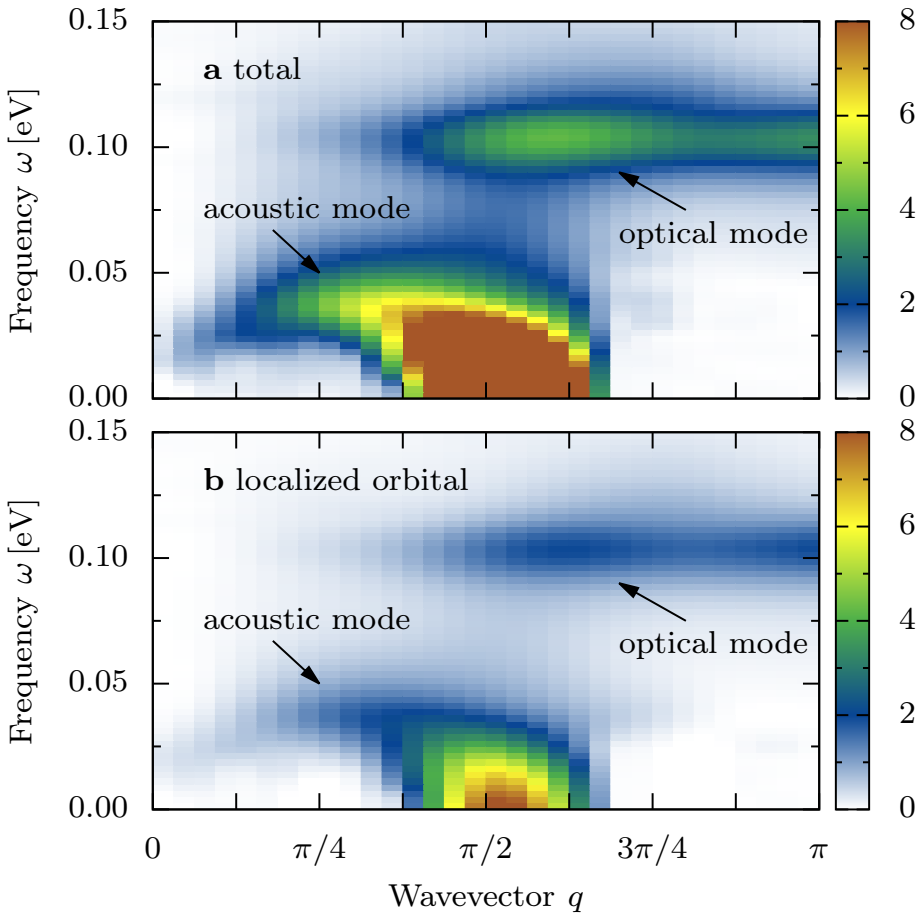

Figure 5.2: Dynamical spin structure factor (SSF). (a) Total SSF, $S(q,\omega)$, and (b) SSF of the localized orbital, $S_{22}(q,\omega)$. Both results exhibit a low-energy acoustic and a high-energy optical modes. Note that the spectral weight of the localized orbital, S_{22}, constitutes $\sim 50\%$ of the total SSF weight. The results were obtained using a dynamical DMRG method with parameters $L = 16$ (48 orbitals), $M = 800$, $\delta\omega = 0.005\,\mathrm{eV}$, and $\eta/\delta\omega = 2$.

as a function of $\widetilde{q}$ then is located between $0 < \widetilde{q} < \pi$, resembling a gapless continuum of spin excitations. Such an interpretation is consistent with "collective" spin waves based on FM blocks. On the other hand, the high-energy optical contribution is q-independent for $q/\pi \gtrsim 1/2$, with vanishing intensity in the $q \to 0$ limit. As discussed later, this mode can be associated to local (on-site) spin excitations affecting the Coulomb potential portion of the Hamiltonian, independently of the dimensionality of the system. The q-dependence of both modes is also clearly visible in the static SSF obtained from the energy integration of

the dynamical SSF, i.e. $S_\alpha(q) = (1/\pi)\int \mathrm{d}\omega\, S(q,\omega)$. In Fig. 5.3(b) we present the acoustic ($\alpha = \mathrm{A}$) and optical ($\alpha = \mathrm{O}$) contribution to the total ($\alpha = T$) static SSF, coming from the integration over the frequency ranges $0 < \omega < \omega_c$, $\omega_c < \omega < \infty$, and $0 < \omega < \infty$, respectively. From the dynamical SSF spectra, it is evident that $S_\mathrm{O}(q)$ provides the sole contribution to the total static SSF for momentum $0.75 < q/\pi < 1$. As a consequence, at least within a block-OSMP state it is remarkable that already in the static SSF one can observe the clear presence of an optical mode, a novel result which is intrinsic of block phases to our knowledge. In the same panel, we also present the total static SSF independently obtained from the expectation value of the ground state (GS), i.e., $S_\mathrm{stat}(q) = \langle \mathrm{GS}|S_q \cdot S_{-q}|\mathrm{GS}\rangle$, where S_q is the Fourier transform of the S_ℓ operators for the same system size L. The agreement between $S_\mathrm{stat}(q)$ and $S_\mathrm{T}(q)$ serves as nontrivial accuracy test of the dynamical DMRG method, since the former can be obtained with much higher accuracy.

Orbital contribution. Before addressing the optical and acoustic modes in more detail, we will comment on the orbital γ contribution to $S(q,\omega)$. As already shown in Fig. 5.2, the main contribution to the total SSF originates in the localized orbital $\gamma = 2$. Our results [see Fig. 5.3(c)] indicate that the spin fluctuations for the itinerant electrons (orbitals $\gamma = 0$ and $\gamma = 1$) follow the behavior of the localized orbital. As argued below, this is a consequence of the Hund coupling which aligns ferromagnetically spins at different orbitals. However, the nature of these orbitals is metallic and magnetic moments are not well formed. As a consequence, the spectral weight of the total itinerant contribution (2 orbitals) is approximately the same as the localized (1 orbital). On the other hand the inter-orbital SSF $S_{\gamma\neq\gamma'}$ have a large contribution only to the acoustic mode, especially near the $q/\pi = 1/2$ point.

Acoustic mode. Consider now the properties of the acoustic mode. Motivated by the results presented above, with the main contribution to the SSF arising from the localized orbital, we express the eigenstates in terms of the basis states of localized orbital $|\cdot\rangle_{\gamma=2}$ (see Appendix D.1). Since the electrons are indeed localized with occupation $n_{\gamma=2} = 1$ [5] in the OSMP, in the low-energy portion of the spectrum the basis states with empty and double

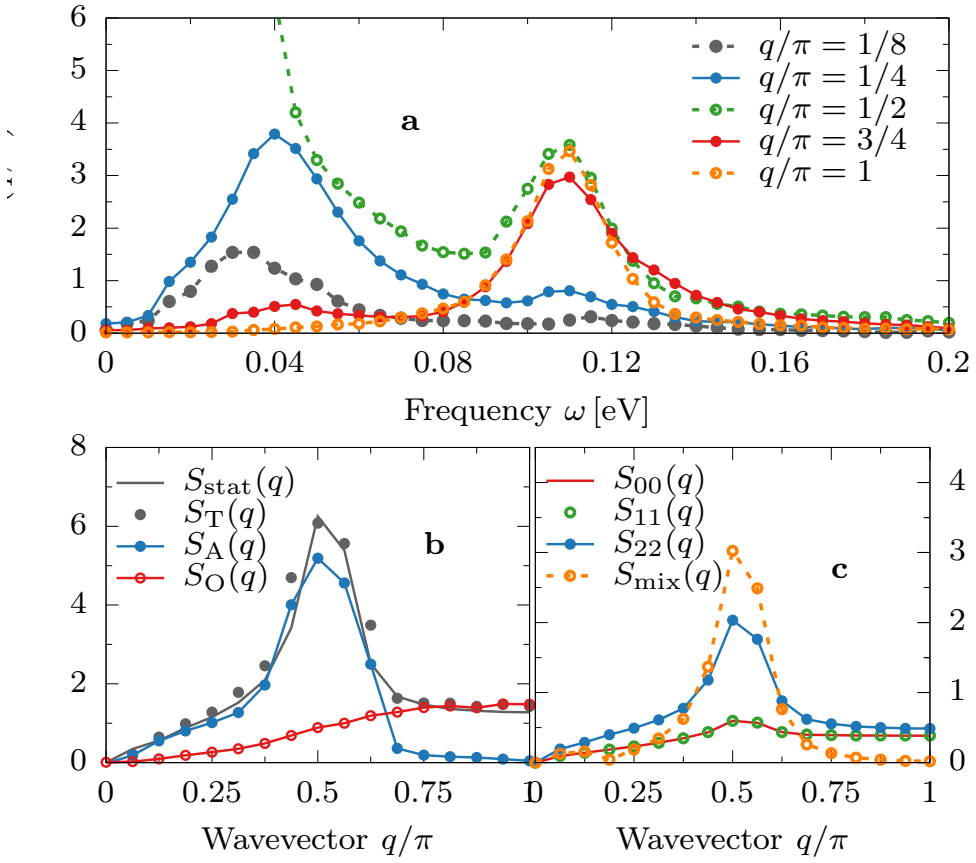

Figure 5.3: Frequency and momentum dependence. (a) Finite momentum cuts, $q/\pi = 1/8, 1/4, 1/2, 3/4, 1$, of the dynamical SSF. (b) Total static SSF obtained as an expectation value in the $|\mathrm{GS}\rangle$, $S_{\rm stat}(q)$ (black line), and also via the ω integration of the dynamical SSF, $S_{\rm T}(q)$ (black points). In the same panel we present also the contributions to the static SSF from acoustic and optical modes, $S_{\rm A}(q)$ and $S_{\rm O}(q)$, respectively. (c) Contribution to the static SSF $S_{\gamma\gamma'}(q)$: $\gamma = \gamma'$ represents the SSF component for each of the orbitals, while $S_{\rm mix}(q) = \sum_{\gamma\neq\gamma'} S_{\gamma\gamma'}(q)$ represents the sum of the inter-orbital contributions. The system parameters are the same as in Fig. 5.2.

occupied orbital $\gamma = 2$ should not be present. Within such a representation the GS of the block-OSMP phase can be identified as a superposition of $|\uparrow\uparrow\downarrow\downarrow\rangle_{\gamma=2}$ and $|\downarrow\downarrow\uparrow\uparrow\rangle_{\gamma=2}$ states which constitutes $\sim 50\%$ of the true GS. One can improve further the qualitative description by investigating a simple toy model. Let us consider two FM coupled $S = 1/2$ spins as one $S = 1$ object, i.e. $|\mathbf{1}\rangle = |\uparrow\uparrow\rangle_{\gamma=2}$, $|-\mathbf{1}\rangle = |\downarrow\downarrow\rangle_{\gamma=2}$, and $|\mathbf{0}\rangle = 1/\sqrt{2}(|\uparrow\downarrow\rangle_{\gamma=2} + |\uparrow\downarrow\rangle_{\gamma=2})$. In this setup, a 4-site $S = 1/2$ system reduces to two antiferromagnetically coupled $S = 1$

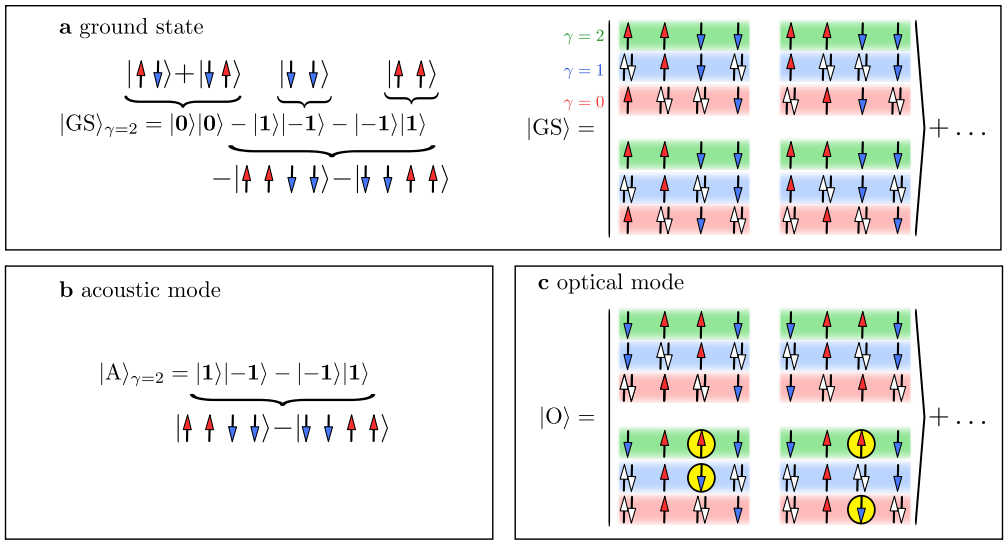

Figure 5.4: States relevant for the dynamical SSF. Spin configuration in the localized orbital ($\gamma = 2$) (see text for details) of the (a) $|\mathrm{GS}\rangle$ (singlet) and (b) $|\mathrm{A}\rangle$ state (triplet) contributing to the acoustic mode. (c) Schematic representation of particle configuration of all orbitals of the $|\mathrm{GS}\rangle$ and optical triplet $|\mathrm{O}\rangle$. Circles represent pairs of antiferromagnetically aligned spins which break the Hund's rule.

spins. The ground state of the latter is simply

$$|\mathrm{GS}\rangle_{\gamma=2} = c_a|\mathbf{0}\rangle|\mathbf{0}\rangle - c_b\Big(|\mathbf{1}\rangle|-\mathbf{1}\rangle + |-\mathbf{1}\rangle|\mathbf{1}\rangle\Big)\,, \tag{5.2}$$

where $c_a = c_b = 1/\sqrt{3}$ [see Fig. 5.4(a) for a schematic representation]. Note that the above state, in agreement with numerics, is a singlet. The last two terms of Eq. 5.2 correspond to the "perfect" block order, i.e., $|\uparrow\uparrow\downarrow\downarrow\rangle_{\gamma=2} + |\downarrow\downarrow\uparrow\uparrow\rangle_{\gamma=2}$, while the first term depicts the x–y component of the block order,

$$\begin{aligned}|\mathbf{0}\rangle|\mathbf{0}\rangle = \frac{1}{2}\Big(&|\uparrow\downarrow\uparrow\downarrow\rangle_{\gamma=2} + |\downarrow\uparrow\downarrow\uparrow\rangle_{\gamma=2} \\ &+ |\uparrow\downarrow\downarrow\uparrow\rangle_{\gamma=2} + |\downarrow\uparrow\uparrow\downarrow\rangle_{\gamma=2}\Big)\,.\end{aligned} \tag{5.3}$$

Our $L = 4$ Lanczos investigation of the full Hamiltonian indicates that such a state has coefficients equal to $\widetilde{c}_a^2 \simeq 1/6$ and $\widetilde{c}_b^2 \simeq 1/4$, which yields now a better overlap, $\sim 70\%$, with the true GS. Finally, the first excited state - contributing to the acoustic mode - can

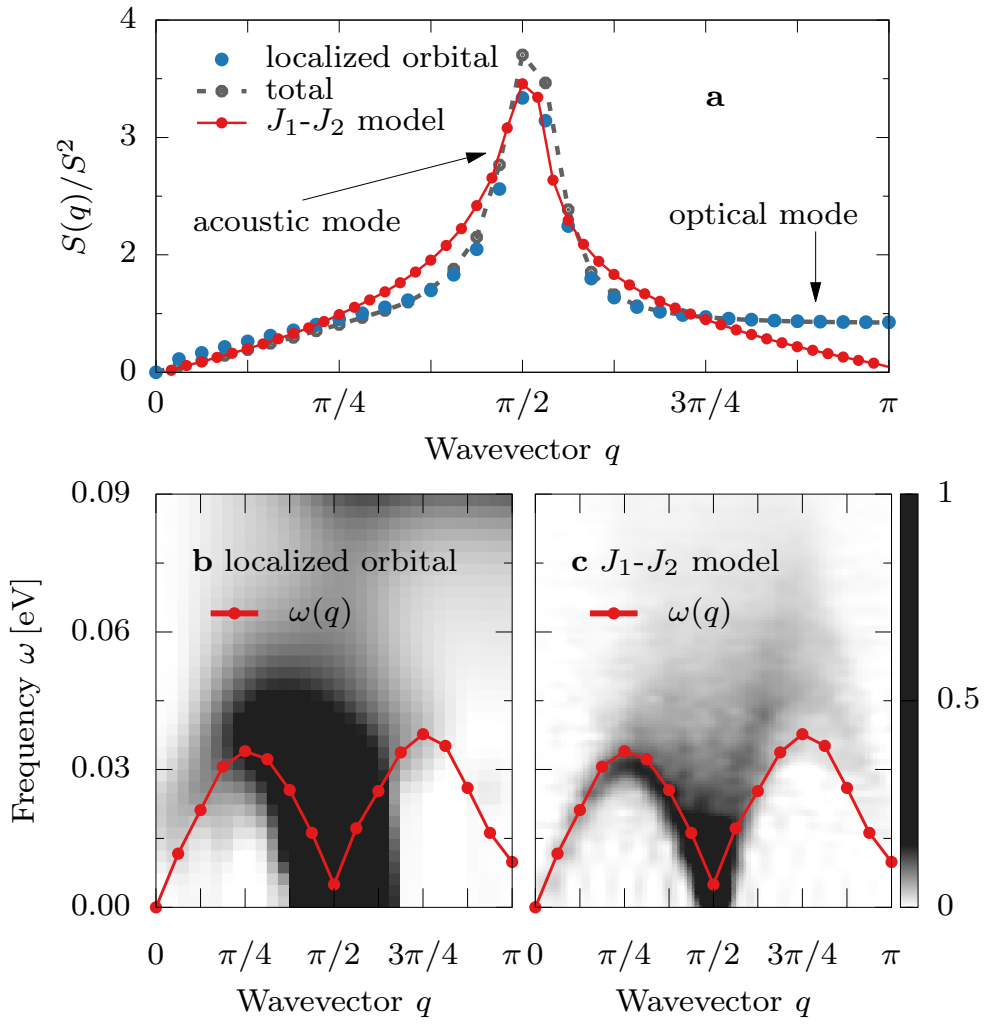

Figure 5.5: Comparison with the J_1–J_2 model. (a) Comparison of the static SSF $S(q)$ corresponding to the multi-orbital system vs results for the J_1–J_2 model with $J_2/|J_1| = 1$, calculated for $L = 32$ and $L = 48$, respectively. $S(q)$ is normalized by the local magnetic moment squared $S^2 = S(S+1)$, where $S^2 = 3/4$ for the localized orbital and the J_1–J_2 result, and $S^2 = 2$ [5] for the total SSF. (b) Acoustic mode of the dynamical SSF within the block-OSMP phase [the same results as in Fig. 5.2(b)] compared against the dispersion relation $\omega(q)$ of the J_1–J_2 model with $|J_1| = J_2 = 0.6J_{\text{eff}}$, where the effective spin exchange energy scale is set to $J_{\text{eff}} = 4\,t_{22}^2/U$. The latter is obtained with the help of Lanczos diagonalization on a chain of 32 sites with periodic boundary conditions. (c) Dynamical SSF of the J_1–J_2 model with $|J_1| = J_2 = 0.6J_{\text{eff}}$ as calculated using DMRG for a $L = 48$ chain.

be identified as a triplet of the form $|\mathrm{A}\rangle_{\gamma=2} = \widetilde{c}_A(|\uparrow\uparrow\downarrow\downarrow\rangle_{\gamma=2} - |\downarrow\downarrow\uparrow\uparrow\rangle_{\gamma=2})$ where $\widetilde{c}_A^2 \simeq 4/9$ [see Fig. 5.4(b)]. This large overlap of $|\mathrm{A}\rangle_{\gamma=2}$ with the full solution is also captured by

the toy model since $|\mathbf{1}\rangle|-\mathbf{1}\rangle - |-\mathbf{1}\rangle|\mathbf{1}\rangle$ is one of the first excitations in our two-site $S = 1$ problem. Note that the above description of the $|\mathrm{GS}\rangle_{\gamma=2}$ ($|\mathrm{A}\rangle_{\gamma=2}$) as a spin singlet (triplet) is not obvious from the signs of the localized orbital basis representation. While the above states capture the essence of the problem, the itinerant orbitals have to be included in the description to account for the true nature of the singlet-triplet excitation.

Although simplified, descriptions such as those above of the low-energy spectrum can yield nontrivial consequences. A similar ground state to our $|\mathrm{GS}\rangle_{\gamma=2}$ with $\pi/2$ pitch angle was previously observed in the frustrated ferromagnetic $S = 1/2$ J_1–J_2 Heisenberg model with ferromagnetic J_1 and antiferromagnetic J_2 [170, 171, 168, 172, 173]. In Fig. 5.5(a) we present a comparison of the multi-orbital system SSF vs J_1-J_2 results obtained for $J_2/|J_1| = 1$. Within the latter the dynamical SSF yields a continuum of excitations with maximum intensity at $q/\pi = 1/2$ and vanishing intensity in the $q/\pi \to 1$ limit. In fact, the dynamical SSF of the J_1–J_2 model is very similar to the acoustic mode found in our multi-orbital system, i.e. compare panels (b) and (c) of Fig. 5.5. To strengthen this argument, in Fig. 5.5(b,c) we present the dynamical SSF factor plotted against the quantum dispersion relation of the J_1–J_2 model $\omega(q) = \epsilon_q - \epsilon_{\mathrm{GS}}$ where ϵ_q is the energy of the lowest eigenstate at a given q. To match the energy scales we set $|J_1| = J_2 = 0.6 J_{\mathrm{eff}}$ where $J_{\mathrm{eff}} = 4\,t_{22}^2/U$ is the natural superexchange scale within the localized orbital, as a crude approximation. As clearly shown in Fig. 5.5(b), $\omega(q)$ quantitatively captures the main features of the acoustic portion of the spectrum.

We remark that the present comparison with the J_1–J_2 model is at a phenomenological level, since this effective description of the lowest mode of the spin dynamics was not rigorously derived from our multi-orbital Hamiltonian. The acoustic mode reflects the frustrated nature of the magnetism within the block-OSMP phase. Also, the J_1–J_2 model may be relevant in a wide range of interaction U within the OSMP phase, beyond the block ordering region $0.4 \lesssim U/W \lesssim 1.5$. For example, previous results showed that in the range $1.5 \lesssim U/W \lesssim 20$ the system is in a ferromagnetic-OSMP [5], where the spins within the localized orbital $\gamma = 2$ have ferromagnetic ordering. Clearly, a J_1–J_2 model with small or vanishing J_2 will also exhibit a similar ordering. Finally, note that although the alternative $S = 1$ toy model is useful in the description of elementary states of the block-OSMP system,

its validity is limited for the dynamical spin response: it is well known that the dynamical SSF of the $S = 1$ AFM Heisenberg model exhibits "sharp" magnon lines, in contrast to the $S(q, \omega)$ of the $S = 1/2$ model that contains a continuum of excitation (at least at low-ω), in agreement with our results for the three-orbital Hamiltonian.

Optical mode. Let us now turn to the high-energy optical mode of the dynamical SSF spectrum. The states contributing to this mode are also triplet excitations. In the $L = 4$ Lanczos analysis we found that this high-energy mode arises from a state of the form $|\mathrm{O}\rangle_{\gamma=2} \simeq 1/2(|\downarrow\uparrow\uparrow\downarrow\rangle_{\gamma=2} + |\uparrow\downarrow\downarrow\uparrow\rangle_{\gamma=2})$. It is evident that $|\mathrm{O}\rangle$ breaks the FM magnetic unit cells present in the GS. Note, again, that the discussed states do not have doubly occupied or empty sites, reflecting the Mott nature of orbital $\gamma = 2$. It should be also pointed out that using a small $L = 4$ system with OBC we have found another state which contributes to the optical mode, i.e., $|\widetilde{\mathrm{O}}\rangle_{\gamma=2} = 1/2(|\downarrow\uparrow\downarrow\uparrow\rangle_{\gamma=2} + |\uparrow\downarrow\uparrow\downarrow\rangle_{\gamma=2})$. However, such a state is not present in the system with periodic boundary conditions.

To understand properly the optical mode it is not enough to focus solely on the localized orbital. A detailed analysis of the remaining "metallic" orbitals $\gamma = 0, 1$ indicates that: (i) the $|\mathrm{GS}\rangle$ and the $|\mathrm{A}\rangle$ states obey the Hund's rule: spins in different orbitals of the same site are ferromagnetically aligned [see Fig. 5.4(a) for a schematic representation]. (ii) However, the $|\mathrm{O}\rangle$ states, Fig. 5.4(c), do not fulfill this rule because part of the spins are antiferromagnetically aligned. As a consequence, the main difference in energy between the $|\mathrm{GS}\rangle$ and $|\mathrm{O}\rangle$ arises from the local (on-site) Hund exchange portion of the electronic interaction. We confirm this by calculating separately the expectation values of all terms contributing to the Hamiltonian (see Appendix D.1). The main difference between the energy of the $|\mathrm{GS}\rangle$ and $|\mathrm{A}\rangle$ arises from the kinetic portion. On the other hand, the difference in $|\mathrm{O}\rangle$ originates, as expected, from the Hund coupling part of the interaction energy. The local on-site nature of the optical mode is also visible in the orbital resolved SSF. In Fig. 5.3(c) we present the spin correlations between different orbitals at different sites, i.e. S_{mix}. As clearly visible, the $S_{\mathrm{mix}}(q \to \pi) \to 0$, indicating a drastic reduction of spectral weight at large momentum. These findings indicate that the optical mode is not present in the inter-orbital inter-site spin correlations. As a consequence, the only remaining possibility of the origin of

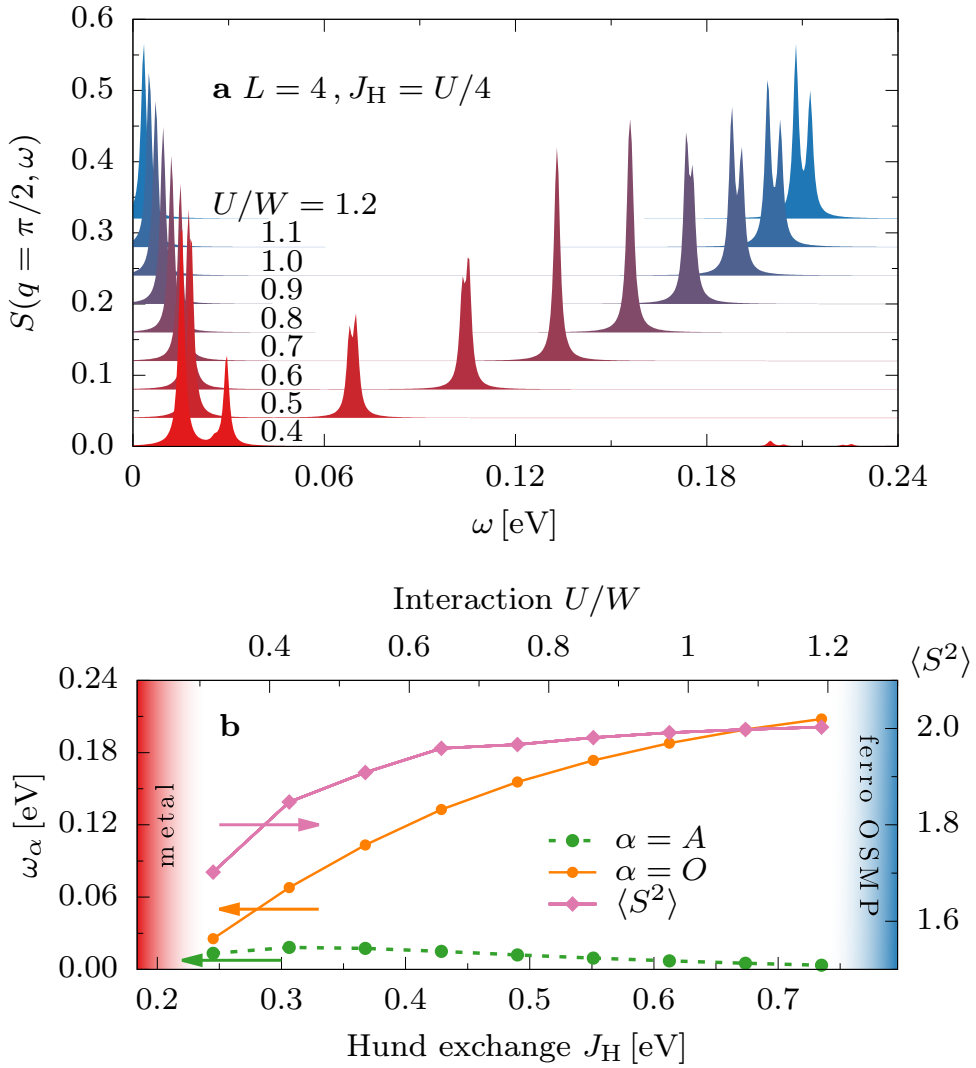

Figure 5.6: Hund exchange dependence. (a) Dynamical SSF at $q/\pi = 1/2$ for various values of the interaction U, all within the block-OSMP phase, $U/W = 0.4, \ldots, 1.2$ (bottom to top, with 0.04 offset), at a fixed $J_{\rm H}/U = 1/4$, calculated for $L = 4$ using the Lanczos method. (b) Left y-axis: Frequency $\omega_\alpha = \epsilon_\alpha - \epsilon_{\rm GS}$ dependence of the acoustic and optical modes vs the value of the Hund exchange coupling $J_{\rm H}$. Right y-axis: Magnetic moment $\langle S^2 \rangle$ development within the block-OSMP phase.

the optical mode are the intra-site fluctuations between orbitals. Our investigation of orbital resolved SSF [see Fig. 5.3(c)] shows that each orbital contributes to the optical mode with a similar weight. Finally, the lack of momentum dependence of the optical mode (at least

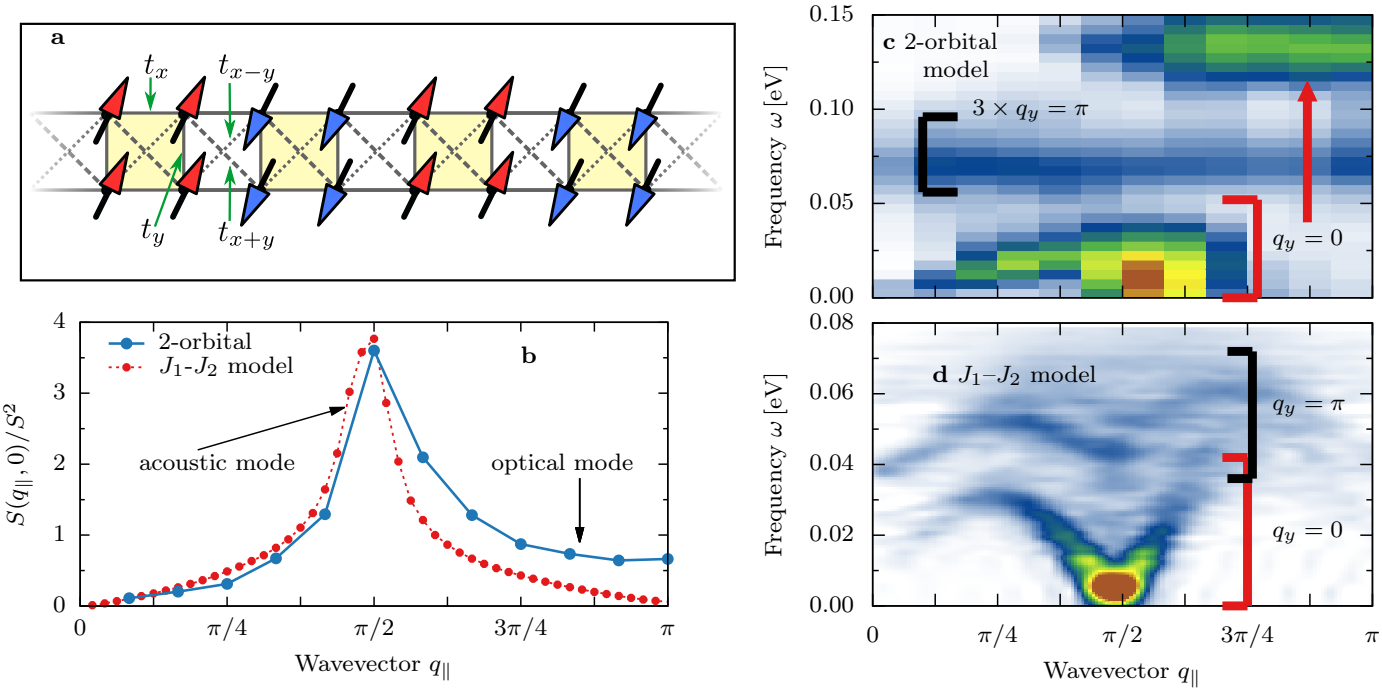

Figure 5.7: Spin dynamics within the ladder geometry. (a) Schematic representation of the two-orbital two-leg ladder system used in our analysis (see Appendix D.1 for details). Arrows depict the 2×2 block state. (b) Static SSF in the $q_y = 0$ sector for both bthe J_1-J_2 and multi-orbital models on a ladder geometry. (c,d) Dynamical SSF of the (c) two-orbital and (d) J_1-J_2 spin models on a two-leg ladder geometry (using $L = 12$ and $L = 48$ rungs, respectively).

for $q/\pi > 1/2$) suggests that such excitations are local (on-site) fluctuations of spin between different orbitals at the same site.

In addition, we have shown that the frequency $\omega_{\rm O} = \epsilon_{\rm O} - \epsilon_{\rm GS}$ of the corresponding $|{\rm O}\rangle$ excitation is directly proportional to the value of the Hund exchange $J_{\rm H}$, contrary to the $|{\rm A}\rangle$ excitation with energy $\omega_{\rm A} = \epsilon_{\rm A} - \epsilon_{\rm GS}$. In Fig. 5.6(a) we present the dynamical SSF at $q/\pi = 1/2$ for various values of U within the block-OSMP calculated via the Lanczos method on $L = 4$ sites, at a fixed $J_{\rm H}/U = 1/4$. Our results in Fig. 5.6(b) indicate that this behavior is valid throughout the entire block-OSMP phase, $0.4 \lesssim U/W \lesssim 1.5$.

Ladder geometry. Finally, let us comment on the lattice geometry dependence of our results. In Fig. 5.7 we present the SSF for the two-leg ladder two-orbital Hamiltonian introduced in Ref. [24] for the $BaFe_2Se_3$ compound. The lattice is sketched in Fig. 5.7(a) and hopping values are given in the Appendix D.1. It was previously shown [24] that at density $\overline{n} = 1.75/2$, $J_{\rm H} = U/4$, and $U/W_L = 2$ with $W_L = 3.82\,\text{eV}$ the system is in an enlarged block phase, similar to the 2×2 block state of $BaFe_2Se_3$ [4]. Before addressing specific results, it is important to remark that the DMRG numerical studies of multi-orbital ladders require expensive computations. This is because the inter-site inter-orbital hoppings behave effectively as long-distance hoppings in the equivalent one-dimensional representation, leading to larger entanglement for the ground state (see Appendix D.2 for details). The calculation of dynamical quantities is certainly a challenge and even the static expectation values have to be carefully analyzed with regards to the number of states kept (here $M = 1000$ states are used). As a consequence, the results presented for the two-orbital two-leg ladder below may not be as accurate as those for the chains.

On a ladder, there are two separate contributions to the SSF arising from the bonding ($q_y = 0$) and antibonding ($q_y = \pi$) sectors. For the two-orbital two-leg ladder results, presented in Fig. 5.7(b), we find a $q_y = 0$ dispersive mode at low- ω, with a continuum of spin excitations similar to the acoustic mode of the chain geometry. At $\omega \simeq 0.075\,\text{eV}$ we find an energy narrow $q_y = \pi$ mode. According to our analysis of the 1D system, a similar spectrum can be found in the J_1-J_2 model on the ladder with FM rung coupling $J_\perp = J_1$, see Fig. 5.7(c-d). Both the J_1-J_2 spin model and multi-orbital model on the ladder studied here exhibit the 2×2 block state, i.e. AFM coupled blocks of four FM aligned spins on two neighbouring rungs [see Fig. 5.7(a)]. Such a state has a peak in the static SSF at $q_x = \pi/2$ in the bonding contribution ($q_y = 0$), see Fig. 5.7(c). Note that the maximum of the acoustic mode appear at $\omega \neq 0$, which suggests a non-zero spin gap, common in ladders. Finally, at higher frequencies ($\omega \simeq 0.13\,\text{eV}$) in the $q_y = 0$ sector we find a flat mode of excitations, similar to the optical mode present in the chain analysis. It is again evident that the latter is not captured by the J_1-J_2 model.

5.3 Discussion

Let us compare the INS data for $BaFe_2Se_3$ reported in Ref. [4] against our results. Note that this compound is insulating [151], while our system for the parameters considered in this Chapter, $U/W = 0.8$ and $J_H/U = 1/4$, is a (bad) metal in the block-OSMP phase, becoming insulator only for $U/W \gtrsim 1.5$ in the ferromagnetic-OSMP phase [27]. Our Hamiltonian reproduces the OSMP state and the magnetic block phase of $BaFe_2Se_3$, and although the charge dynamics of our model does not capture the experimentally observed insulating nature of the real material, it is still appealing to study the spin physics. The lack of other multi-orbital models that can reproduce both the spin and charge sector of low-dimensional iron selenides makes it appealing to carry out detailed theoretical calculations of the spin dynamics within this model and compare with the experiments.

Within the spin-wave theory the low-ω portion of the INS spectra was interpreted [4] as a dispersive mode which reflects the frustrated nature of the $\pi/2$-order. In addition, the high-energy optical modes were interpreted as local excitation of spins within the 2×2 plaquette. A similar rationale was used to explain the INS result of the doped compound $Rb_{0.89}Fe_{1.58}Se_2$ [161]. The spin-wave theory of $BaFe_2Se_3$ reproduces [4] all of the modes and also properly captures the frequency bandwidth of the spin excitations. However, only $\sim 2/3$ of the total spectral weight expected for localized $3d$ electrons is obtained. Also note that within the considered spin models of Ref. [4, 161] unphysically large dimerization spin-exchange couplings are required [174, 175] to stabilize the $\pi/2$ spin pattern.

From the perspective of our results, the interpretation of the INS spin spectra of low-dimensional ladder iron chalcogenides is different from spin-wave theory. The latter assumes that all excitations occur between localized spins, while in our system we have a mixture of localized and itinerant electrons. Moreover, as shown above, the SSF of multi-orbital systems not only contains dispersive acoustic modes but also local excitations controlled by the Hund exchange, at least within the block-OSMP. The inter-orbital nature of such modes cannot be properly captured by localized Heisenberg models. Our results, on both chain and ladder geometries, indicate that spin models can only properly capture dispersive modes resulting from the peculiar spin order of a given phase as in the $\pi/2$ state of $BaFe_2Se_3$. However, we

argue that only one of the low lying optical modes of this compound arises from a weakly dispersive (probably beyond experimental resolution of powder sample) $q_y = \pi$ excitation. Within our interpretation of the SSF spectra, the second optical mode is of a different nature, involving inter-orbital spin fluctuations on each site. Such a picture is consistent with our multi-orbital ladder results.

Concerning the spectral weight, for the chosen parameters $U/W = 0.8$ and $J_{\mathrm{H}}/U = 1/4$ we observe the magnetic moment $\langle S^2 \rangle \sim 2$ (maximal possible for $\overline{n} = 4/3$). This is consistent with previous Hartree-Fock calculations [24] of the block-OSMP phase within a five-orbital ladder system, which reported $\langle S^2 \rangle \sim 6$ for $\overline{n} = 6/5$ (again the maximal value). As a consequence, our results do not reproduce the missing spectral weight observed in experiments [4]. However, the magnetic moments evolve within the block-OSMP [5] (see also Appendix D.3 for additional results) and only saturate to its maximal value at $U/W \gtrsim 0.6$, namely in the middle of the block-phase. Since the exact value of U and J_{H} are not know for $BaFe_2Se_3$, it is possible in theoretical investigations to stabilize the block-OSMP phase with a reduced $\langle S^2 \rangle < 2$ [see Fig. 5.6(b)]. Moreover, note that recently it was argued [176] that insufficient energy (time) resolution in INS experiments produces moments that can be smaller than the actual instantaneous moments. In this context, faster x-ray based techniques such as photoemission spectroscopy (PES), x-ray absorption spectroscopy (XAS), and x-ray emission spectroscopy (XES) are needed to resolve this issue.

In conclusion, we have investigated the dynamical spin structure factor of a one-dimensional three-orbital Hubbard model in the block orbital selective Mott phase, as well as a ladder two-orbital Hubbard model also in a similar block state. This has been a computationally demanding effort even with the powerful DMRG, and to our knowledge this is the first time that results of this quality are produced. We have shown that our Hamiltonian captures nontrivial features of a broad family of low-dimensional iron chalcogenides, in particular for the ladder $BaFe_2Se_3$ compound for which $\pi/2$–block order was reported. We have found two different types of modes in the spin spectra: (i) low-frequency dispersive (acoustic) spin excitations and (ii) optical dispersionless excitations at higher energy. The acoustic band reflects the nature of magnetic order of the system, namely for the block-OSMP the frustrated $\pi/2$-ordering can be captured by the quantum

J_1-J_2 frustrated Heisenberg model, as also shown here. The optical band arises from on-site inter-orbital spin fluctuations controlled by the Hund exchange coupling. Finally, our 1D dynamical SSF is in qualitative agreement with the powder INS spectrum of $BaFe_2Se_3$ (see Appendix D.4). Although the latter has only a quasi-1D geometry, with small but nonzero couplings perpendicular to the ladder, the ω dependent spectra should be dominated by the predominantly 1D nature of the system. As a consequence, the location in momentum and energy space is properly resolved by our model Hamiltonian for both of the modes.

Our results are general and should apply to a variety of block states in multi-orbital quasi-1D systems. They should all contain an acoustic band (with pitch wavevector compatible with the size of the magnetic block), a strong asymmetry in the distribution of weight of this acoustic band in different portions of the Brillouin zone, and optical modes with at least one of them related to atomic transitions regulated by the Hund coupling.

Chapter 6

Summary

In this dissertation, studies addressing one-dimensional three-orbital Hubbard models are discussed in detail including the effect of interactions. The primary goal is to gain conceptual understanding of the several exotic phases present in transition metal oxides with multiple orbitals at the Fermi-level, such as iron-based superconductors with $3d$ active orbitals and also compounds of the $4d/5d$ transition metal rows having robust spin-orbit coupling. Exact diagonalization techniques to study small lattice sizes as well as numerically accurate density matrix renormalization group (DMRG) techniques were used to study these one-dimensional chains. Dynamical-DMRG was also used to study the single-particle spectral functions and the dynamical spin structure factor relevant to ARPES and inelastic neutron scattering experiments, respectively.

Chapter 2 focused on the effect of spin-orbit coupling on a three-orbital Hubbard model in the $(t_{2g})^4$ sector (with tetragonal crystal-field splitting) and in one dimension. Fixing the Hund coupling to a robust value compatible with some multiorbital materials, we present the phase diagram varying the Hubbard U and spin-orbit coupling λ, at zero temperature. Accurate DMRG results shows an interesting transition from a spin block orbital-selective Mott phase to a staggered excitonic state accompanied with antiferromagnetic ordering, with increasing λ at intermediate U. In the strong U coupling limit, we find a nonmagnetic insulator with a local effective angular momentum $\langle \mathbf{J}^2_{eff} \rangle \neq 0$ near the excitonic phase, smoothly connected to the regime with $\langle \mathbf{J}^2_{eff} \rangle = 0$. A partial list of quasi-one-dimensional materials where the physics discussed here could be realized was also provided.

In Chapter 3, we further investigated the excitonic condensate with magnetic order using a simpler model with degenerate t_{2g} states. There we showed that the canonical electron-hole excitations (excitons) transform into local triplon excitations at large U. We also showed that the Bose Einstein condensate strong coupling regime of this excitonic magnet is smoothly connected to the intermediate U excitonic insulator region where pairs are no longer at the atomic scale, i.e. in the same atom, but they spread over longer distances. Calculations in one dimension were performed using the DMRG, while in two dimensions we used the Hartree-Fock approximation (HFA). The main result is that at intermediate Hubbard U, increasing λ at fixed U the system transitions from an incommensurate spin-density-wave metal to a Bardeen-Cooper-Schrieffer (BCS) excitonic insulator, with coherence length r_{coh} of order the lattice spacing a and of order 10 times the lattice spacing $10a$ in 1D and 2D, respectively. Further increasing λ, the system eventually crosses over to the BEC limit (with $r_{coh} << a$) previously described.

Experiments involving iridates with noninteger valence states for the Ir ions are also starting to attract attention. In the Chapter 4, we presented the first evidence for the existence of a novel excitonic condensate at $n = 3.5$ in a one-dimensional Hubbard model with a degenerate t_{2g} sector, when in the presence of spin-orbit coupling. At intermediate Hubbard U and spin-orbit λ couplings, we found an excitonic condensate at the unexpected momentum $q = \pi/2$ involving $j_{\text{eff}} = 3/2, m = \pm 1/2$, and $j_{\text{eff}} = 1/2, m = \pm 1/2$ bands in the triplet channel, coexisting with an also unexpected block magnetic order. We also unveiled the entire λ vs U phase diagram, at a fixed and robust Hund coupling. Interestingly, this new "block excitonic phase" is present even at large values of λ, unlike the $n = 4$ excitonic phase discussed in Chapters 2 and 3. Our computational study hopefully will help to better understand and predict the possible magnetic phases of materials with $d^{3.5}$ valence and robust spin-orbit coupling.

In Chapter 5, we presented the theoretical prediction for the dynamical spin structure factor within a block orbital-selective Mott phase regime using the density-matrix renormalization-group method. Previous theoretical investigations of the multi-orbital Hubbard model in one-dimension revealed the existence of an orbital-selective Mott phase with block spin order. Recent inelastic neutron scattering (INS) experiments on the $BaFe_2Se_3$

ladder compound confirmed the relevance of the block-OSMP. Moreover, this powder INS spectrum revealed an unexpected structure, containing both low-energy acoustic (spin waves) and high-energy optical modes. In agreement with experiments, we find two dominant features: low-energy dispersive and high-energy dispersionless modes. We argue that the former represents the spin-wave-like dynamics of the block ferromagnetic islands, while the latter is attributed to a novel type of local on-site spin excitations controlled by the Hund coupling.

In summary, by using accurate numerical techniques we were able to study complicated multiorbital Hubbard models in chains, and in some cases also in ladders. The merit of our work is that we have unveiled many interesting phases keeping a high level of confidence that the results are correct. Often in higher dimensions, such as 2D and 3D, crude approximations are required to treat equally complex models, and for this reason a veil of uncertainty exists in comparing with experiments because we do not know how accurate the theoretical predictions are. However, in one dimension this uncertainty issue is removed, providing a fertile playground for cross fertilization between theory and experiments.

Bibliography

[1] Q. Si, R. Yu, and E. Abrahams, "High-temperature superconductivity in iron pnictides and chalcogenides," *Nat Rev Mater*, vol. 1, 2016. ix, 2

[2] Y. Nambu, K. Ohgushi, S. Suzuki, F. Du, M. Avdeev, Y. Uwatoko, K. Munakata, H. Fukazawa, S. Chi, Y. Ueda, and T. J. Sato, "Block magnetism coupled with local distortion in the iron-based spin-ladder compound $bafe_2se_3$," *Phys. Rev. B*, vol. 85, p. 064413, Feb 2012. ix, 2, 3, 66

[3] J. Ying, H. Lei, C. Petrovic, Y. Xiao, and V. V. Struzhkin, "Interplay of magnetism and superconductivity in the compressed fe-ladder compound $bafe_2se_3$," *Phys. Rev. B*, vol. 95, p. 241109, Jun 2017. ix, 2, 3, 4

[4] M. Mourigal, S. Wu, M. B. Stone, J. R. Neilson, J. M. Caron, T. M. McQueen, and C. L. Broholm, "Block magnetic excitations in the orbitally selective mott insulator $bafe_2se_3$," *Phys. Rev. Lett.*, vol. 115, p. 047401, Jul 2015. ix, xviii, 5, 6, 66, 67, 69, 70, 80, 81, 82, 134, 137

[5] J. Rincón, A. Moreo, G. Alvarez, and E. Dagotto, "Exotic magnetic order in the orbital-selective mott regime of multiorbital systems," *Phys. Rev. Lett.*, vol. 112, p. 106405, Mar 2014. xvi, 5, 9, 12, 19, 62, 66, 67, 68, 69, 70, 72, 75, 76, 82, 132, 133

[6] P. J. Brown, "Magnetic form factors," *Chapter 4.4.5, International tables for crystallography vol. C (A. J. C. Wilson, ed.)*, pp. 391–399. xviii, 134, 137

[7] J. Hubbard, "Electron correlations in narrow energy bands," *Proc. R. Soc. Lond.*, vol. 276, no. 1365, 1963. 1

[8] J. Bednorz and K. Müller, "Possible hight c superconductivity in the balacuo system," *Physik B - Condensed Matter*, vol. 64, pp. 189–193, 1986. 1

[9] E. Dagotto, "Correlated electrons in high-temperature superconductors," *Rev. Mod. Phys.*, vol. 66, pp. 763–840, Jul 1994. 1, 50, 58, 65

[10] S. R. White and D. J. Scalapino, "Density matrix renormalization group study of the striped phase in the 2d $t - J$ model," *Phys. Rev. Lett.*, vol. 80, pp. 1272–1275, Feb 1998. 1

[11] C. Buhler, S. Yunoki, and A. Moreo, "Magnetic domains and stripes in a spin-fermion model for cuprates," *Phys. Rev. Lett.*, vol. 84, pp. 2690–2693, Mar 2000. 1

[12] M. Moraghebi, S. Yunoki, and A. Moreo, "Robust d-wave pairing correlations in a hole-doped spin-fermion model," *Phys. Rev. Lett.*, vol. 88, p. 187001, Apr 2002. 1

[13] E. Dagotto, J. Riera, and D. Scalapino, "Superconductivity in ladders and coupled planes," *Phys. Rev. B*, vol. 45, pp. 5744–5747, Mar 1992. 1

[14] E. Dagotto, "Experiments on ladders reveal a complex interplay between a spin-gapped normal state and superconductivity," *Reports on Progress in Physics*, vol. 62, pp. 1525–1571, nov 1999. 1

[15] M. Uehara, T. Nagata, J. Akimitsu, H. Takahashi, N. Mri, and K. Kinoshita, "Superconductivity in the ladder material sr0.4ca13.6cu24o41.84," *Journal of the Physical Society of Japan*, vol. 65, no. 9, pp. 2764–2767, 1996. 1, 66

[16] Y. Kamihara, H. Hiramatsu, M. Hirano, R. Kawamura, H. Yanagi, T. Kamiya, and H. Hosono, "Iron-based layered superconductor: laofep," *Journal of the American Chemical Society*, vol. 128, no. 31, pp. 10012–10013, 2006. PMID: 16881620. 2

[17] Y. Kamihara, T. Watanabe, M. Hirano, and H. Hosono, "Iron-based layered superconductor la[o1-xfx]feas (x = 0.050.12) with tc = 26 k," *Journal of the American Chemical Society*, vol. 130, no. 11, pp. 3296–3297, 2008. PMID: 18293989. 2

[18] P. Dai, J. P. Hu, and E. Dagotto, "Magnetism and its microscopic origin in iron-based high-temperature superconductors," *Nature Physics*, vol. 8, pp. 709–718, Oct 2012. 2, 8, 12, 46, 66

[19] V. J. Emery, "Theory of high-t_c superconductivity in oxides," *Phys. Rev. Lett.*, vol. 58, pp. 2794–2797, Jun 1987. 2

[20] B. Lau, M. Berciu, and G. A. Sawatzky, "High-spin polaron in lightly doped cuo_2 planes," *Phys. Rev. Lett.*, vol. 106, p. 036401, Jan 2011. 2

[21] E. Dagotto, "Colloquium: The unexpected properties of alkali metal iron selenide superconductors," *Rev. Mod. Phys.*, vol. 85, pp. 849–867, May 2013. 2

[22] H. Takahashi, A. Sugimoto, Y. Nambu, T. Yamauchi, Y. Hirata, T. Kawakami, M. Avdeev, K. Matsubayashi, F. Du, C. Kawashima, H. Soeda, S. Nakano, Y. Uwatoko, Y. Ueda, T. J. Sato, and K. Ohgushi, "Pressure-induced superconductivity in the iron-based ladder material $bafe_2s_3$," *Nature Materials*, vol. 14, p. 1008, 2015. 2, 66

[23] W. Li, C. Setty, X. Chen, and et al., "Electronic and magnetic structures of chain structured iron selenide compounds," *Front. Phys.*, vol. 9, pp. 465–471, 2014. 4

[24] Q. Luo, A. Nicholson, J. Rincón, S. Liang, J. Riera, G. Alvarez, L. Wang, W. Ku, G. D. Samolyuk, A. Moreo, and E. Dagotto, "Magnetic states of the two-leg-ladder alkali metal iron selenides afe_2se_3," *Phys. Rev. B*, vol. 87, p. 024404, Jan 2013. 4, 68, 80, 82, 130

[25] J. Rincón, A. Moreo, G. Alvarez, and E. Dagotto, "Quantum phase transition between orbital-selective mott states in hund's metals," *Phys. Rev. B*, vol. 90, p. 241105, Dec 2014. 5, 9, 12, 19, 62, 69

[26] G. Liu, N. Kaushal, S. Li, C. B. Bishop, Y. Wang, S. Johnston, G. Alvarez, A. Moreo, and E. Dagotto, "Orbital-selective mott phases of a one-dimensional three-orbital hubbard model studied using computational techniques," *Phys. Rev. E*, vol. 93, p. 063313, Jun 2016. 5, 9, 12, 19, 62

[27] S. Li, N. Kaushal, Y. Wang, Y. Tang, G. Alvarez, A. Nocera, T. A. Maier, E. Dagotto, and S. Johnston, "Nonlocal correlations in the orbital selective mott phase of a one-dimensional multiorbital hubbard model," *Phys. Rev. B*, vol. 94, p. 235126, Dec 2016. 5, 9, 12, 19, 22, 62, 81

[28] N. D. Patel, A. Nocera, G. Alvarez, A. Moreo, S. Johnston, and E. Dagotto, "Fingerprints of an orbital-selective mott phase in the block magnetic state of $bafe_2se_3$ ladders," *Communication Physics*, vol. 2, 2019. 5

[29] N. D. Patel, N. Kaushal, A. Nocera, G. Alvarez, and E. Dagotto, "Emergence of superconductivity in doped multiorbital hubbard chains," *npj Quantum Materials volume*, vol. 5, 2020. 5

[30] G. Cao and P. Schlottmann, "The challenge of spin–orbit-tuned ground states in iridates: a key issues review," *Reports on Progress in Physics*, vol. 81, p. 042502, feb 2018. 6, 46

[31] R. J. Cava, B. Batlogg, K. Kiyono, H. Takagi, J. J. Krajewski, W. F. Peck, L. W. Rupp, and C. H. Chen, "Localized-to-itinerant electron transition in $sr_2ir_{1-x}ru_xo_4$," *Phys. Rev. B*, vol. 49, pp. 11890–11894, May 1994. 6, 46

[32] T. Shimura, Y. Inaguma, T. Nakamura, M. Itoh, and Y. Morii, "Structure and magnetic properties of $sr_{2-x}a_xiro_4$ (a=ca and ba)," *Phys. Rev. B*, vol. 52, pp. 9143–9146, Oct 1995. 6, 46

[33] G. Cao, J. Bolivar, S. McCall, J. E. Crow, and R. P. Guertin, "Weak ferromagnetism, metal-to-nonmetal transition, and negative differential resistivity in single-crystal sr_2iro_4," *Phys. Rev. B*, vol. 57, pp. R11039–R11042, May 1998. 6, 46

[34] H. Okabe, M. Isobe, E. Takayama-Muromachi, A. Koda, S. Takeshita, M. Hiraishi, M. Miyazaki, R. Kadono, Y. Miyake, and J. Akimitsu, "Ba_2iro_4: A spin-orbit mott insulating quasi-two-dimensional antiferromagnet," *Phys. Rev. B*, vol. 83, p. 155118, Apr 2011. 6, 46

[35] W. Witczak-Krempa, G. Chen, Y. B. Kim, and L. Balents, "Correlated quantum phenomena in the strong spin-orbit regime," *Annual Review of Condensed Matter Physics*, vol. 5, no. 1, pp. 57–82, 2014. 6, 46

[36] H. Watanabe, T. Shirakawa, and S. Yunoki, "Theoretical study of insulating mechanism in multiorbital hubbard models with a large spin-orbit coupling: Slater versus mott scenario in sr_2iro_4," *Phys. Rev. B*, vol. 89, p. 165115, Apr 2014. 6, 46

[37] J. G. Rau, E. K.-H. Lee, and H.-Y. Kee, "Spin-orbit physics giving rise to novel phases in correlated systems: Iridates and related materials," *Annual Review of Condensed Matter Physics*, vol. 7, no. 1, pp. 195–221, 2016. 6, 46

[38] D. Haskel, G. Fabbris, M. Zhernenkov, P. P. Kong, C. Q. Jin, G. Cao, and M. van Veenendaal, "Pressure tuning of the spin-orbit coupled ground state in sr_2iro_4," *Phys. Rev. Lett.*, vol. 109, p. 027204, Jul 2012. 6, 46

[39] B. J. Kim, H. Jin, S. J. Moon, J.-Y. Kim, B.-G. Park, C. S. Leem, J. Yu, T. W. Noh, C. Kim, S.-J. Oh, J.-H. Park, V. Durairaj, G. Cao, and E. Rotenberg, "Novel $J_{\text{eff}} = 1/2$ mott state induced by relativistic spin-orbit coupling in sr_2iro_4," *Phys. Rev. Lett.*, vol. 101, p. 076402, Aug 2008. 7, 46

[40] M. Souri, B. H. Kim, J. H. Gruenewald, J. G. Connell, J. Thompson, J. Nichols, J. Terzic, B. I. Min, G. Cao, J. W. Brill, and A. Seo, "Optical signatures of spin-orbit exciton in bandwidth-controlled Sr_2Iro_4 epitaxial films via high-concentration ca and ba doping," *Phys. Rev. B*, vol. 95, p. 235125, Jun 2017. 7, 47

[41] J. Kim, D. Casa, M. H. Upton, T. Gog, Y.-J. Kim, J. F. Mitchell, M. van Veenendaal, M. Daghofer, J. van den Brink, G. Khaliullin, and B. J. Kim, "Magnetic excitation spectra of sr_2iro_4 probed by resonant inelastic x-ray scattering: Establishing links to cuprate superconductors," *Phys. Rev. Lett.*, vol. 108, p. 177003, Apr 2012. 7, 47

[42] J. Kim, M. Daghofer, A. H. Said, T. Gog, J. van den Brink, G. Khaliullin, and B. J. Kim, "Excitonic quasiparticles in a spinorbit mott insulator," *Nature Communications*, vol. 5, no. 4453, 2014. 7, 47

[43] J. H. Gruenewald, J. Kim, H. S. Kim, J. M. Johnson, J. Hwang, M. Souri, J. Terzic, S. H. Chang, A. Said, J. W. Brill, G. Cao, H.-Y. Kee, and S. S. A. Seo, "Engineering 1d quantum stripes from superlattices of 2d layered materials," *Advanced Materials*, vol. 29, no. 1, p. 1603798, 2017. 7, 47

[44] J. Matsuno, Y. Okimoto, Z. Fang, X. Z. Yu, Y. Matsui, N. Nagaosa, M. Kawasaki, and Y. Tokura, "Metallic ferromagnet with square-lattice coo$_2$ sheets," *Phys. Rev. Lett.*, vol. 93, p. 167202, Oct 2004. 7

[45] B. J. Kim, J. Yu, H. Koh, I. Nagai, S. I. Ikeda, S.-J. Oh, and C. Kim, "Missing xy-band fermi surface in $4d$ transition-metal oxide sr$_2$rho$_4$: Effect of the octahedra rotation on the electronic structure," *Phys. Rev. Lett.*, vol. 97, p. 106401, Sep 2006. 7, 46

[46] B. J. Kim, H. Ohsumi, T. Komesu, S. Sakai, T. Morita, H. Takagi, and T. Arima, "Phase-sensitive observation of a spin-orbital mott state in sr2iro4," *Science*, vol. 323, no. 5919, pp. 1329–1332, 2009. 7, 46

[47] S. Fujiyama, H. Ohsumi, T. Komesu, J. Matsuno, B. J. Kim, M. Takata, T. Arima, and H. Takagi, "Two-dimensional heisenberg behavior of J_{eff}=1/2 isospins in the paramagnetic state of the spin-orbital mott insulator sr$_2$iro$_4$," *Phys. Rev. Lett.*, vol. 108, p. 247212, Jun 2012. 7, 46

[48] G. Jackeli and G. Khaliullin, "Mott insulators in the strong spin-orbit coupling limit: From heisenberg to a quantum compass and kitaev models," *Phys. Rev. Lett.*, vol. 102, p. 017205, Jan 2009. 7, 46

[49] H. Watanabe, T. Shirakawa, and S. Yunoki, "Microscopic study of a spin-orbit-induced mott insulator in ir oxides," *Phys. Rev. Lett.*, vol. 105, p. 216410, Nov 2010. 7, 46

[50] C. Martins, M. Aichhorn, L. Vaugier, and S. Biermann, "Reduced effective spin-orbital degeneracy and spin-orbital ordering in paramagnetic transition-metal oxides: sr$_2$iro$_4$ versus sr$_2$rho$_4$," *Phys. Rev. Lett.*, vol. 107, p. 266404, Dec 2011. 7, 46

[51] B. F. Phelan, E. M. Seibel, D. Badoe, W. Xie, and R. Cava, "Influence of structural distortions on the ir magnetism in ba2xsrxyiro6 double perovskites," *Solid State Communications*, vol. 236, pp. 37 – 40, 2016. 7, 26, 46

[52] G. Cao, T. F. Qi, L. Li, J. Terzic, S. J. Yuan, L. E. DeLong, G. Murthy, and R. K. Kaul, "Novel magnetism of ir^{5+}($5d^4$) ions in the double perovskite sr$_2$yiro$_6$," *Phys. Rev. Lett.*, vol. 112, p. 056402, Feb 2014. 7, 8, 29, 47

[53] J. Terzic, H. Zheng, F. Ye, H. D. Zhao, P. Schlottmann, L. E. De Long, S. J. Yuan, and G. Cao, "Evidence for a low-temperature magnetic ground state in double-perovskite iridates with $Ir^{5+}(5d^4)$ ions," *Phys. Rev. B*, vol. 96, p. 064436, Aug 2017. 7, 8, 29, 47

[54] T. Dey, A. Maljuk, D. V. Efremov, O. Kataeva, S. Gass, C. G. F. Blum, F. Steckel, D. Gruner, T. Ritschel, A. U. B. Wolter, J. Geck, C. Hess, K. Koepernik, J. van den Brink, S. Wurmehl, and B. Büchner, "ba_2yiro_6: A cubic double perovskite material with ir^{5+} ions," *Phys. Rev. B*, vol. 93, p. 014434, Jan 2016. 7, 8, 29, 47

[55] L. T. Corredor, G. Aslan-Cansever, M. Sturza, K. Manna, A. Maljuk, S. Gass, T. Dey, A. U. B. Wolter, O. Kataeva, A. Zimmermann, M. Geyer, C. G. F. Blum, S. Wurmehl, and B. Büchner, "Iridium double perovskite sr_2yiro_6: A combined structural and specific heat study," *Phys. Rev. B*, vol. 95, p. 064418, Feb 2017. 7, 8, 29, 47

[56] O. N. Meetei, W. S. Cole, M. Randeria, and N. Trivedi, "Novel magnetic state in d^4 mott insulators," *Phys. Rev. B*, vol. 91, p. 054412, Feb 2015. 7, 29, 46

[57] C. Svoboda, M. Randeria, and N. Trivedi, "Effective magnetic interactions in spin-orbit coupled d^4 mott insulators," *Phys. Rev. B*, vol. 95, p. 014409, Jan 2017. 7, 23, 29, 38, 46

[58] D. C. Johnston, "The puzzle of high temperature superconductivity in layered iron pnictides and chalcogenides," *Advances in Physics*, vol. 59, no. 6, pp. 803–1061, 2010. 8, 46

[59] P. J. Hirschfeld, M. M. Korshunov, and I. I. Mazin, "Gap symmetry and structure of fe-based superconductors," *Reports on Progress in Physics*, vol. 74, p. 124508, oct 2011. 8

[60] D. J. Scalapino, "A common thread: The pairing interaction for unconventional superconductors," *Rev. Mod. Phys.*, vol. 84, pp. 1383–1417, Oct 2012. 8, 65

[61] D. Liu, H. Zhang, D. Mou, J. He, Y. Ou, Q. Wang, and *et al.*, "Electronic origin of high-temperature superconductivity in single-layer fese superconductor," *Nature Communications*, vol. 3, p. 931, July 2012. 8, 46

[62] S. V. Borisenko, D. V. Evtushinsky, Z.-H. Liu, I. Morozov, and *et al.*, "Direct observation of spinorbit coupling in iron-based superconductors," *Nature Physics*, vol. 12, pp. 311–317, December 2015. 8, 10, 46

[63] T. Sato, T. Shirakawa, and S. Yunoki, "Spin-orbit-induced exotic insulators in a three-orbital hubbard model with $(t_{2g})^5$ electrons," *Phys. Rev. B*, vol. 91, p. 125122, Mar 2015. 10, 17, 20, 21, 46

[64] T. Sato, T. Shirakawa, and S. Yunoki, "Spin-orbital entangled excitonic insulator with quadrupole order," *Phys. Rev. B*, vol. 99, p. 075117, Feb 2019. 10, 17, 20, 21, 26, 28, 29, 46, 52

[65] A. J. Kim, H. O. Jeschke, P. Werner, and R. Valentí, "**J** freezing and hund's rules in spin-orbit-coupled multiorbital hubbard models," *Phys. Rev. Lett.*, vol. 118, p. 086401, Feb 2017. 10, 28, 29, 46

[66] J. Terzic, J. C. Wang, F. Ye, W. H. Song, S. J. Yuan, S. Aswartham, L. E. DeLong, S. V. Streltsov, D. I. Khomskii, and G. Cao, "Coexisting charge and magnetic orders in the dimer-chain iridate $Ba_5AlIr_2o_{11}$," *Phys. Rev. B*, vol. 91, p. 235147, Jun 2015. 10, 48

[67] G. Cao, V. Durairaj, S. Chikara, S. Parkin, and P. Schlottmann, "Partial antiferromagnetism in spin-chain $sr_5rh_4o_{12}$, $ca_5ir_3o_{12}$, and ca_4Iro_6 single crystals," *Phys. Rev. B*, vol. 75, p. 134402, Apr 2007. 10, 47, 48

[68] X. Liu, V. M. Katukuri, L. Hozoi, W.-G. Yin, M. P. M. Dean, M. H. Upton, J. Kim, D. Casa, A. Said, T. Gog, T. F. Qi, G. Cao, A. M. Tsvelik, J. van den Brink, and J. P. Hill, "Testing the validity of the strong spin-orbit-coupling limit for octahedrally coordinated iridate compounds in a model system sr_3cuiro_6," *Phys. Rev. Lett.*, vol. 109, p. 157401, Oct 2012. 10

[69] G. Cao, J. Crow, R. Guertin, P. Henning, C. Homes, M. Strongin, D. Basov, and E. Lochner, "Charge density wave formation accompanying ferromagnetic ordering in

quasi-one-dimensional bairo3," *Solid State Communications*, vol. 113, no. 11, pp. 657 – 662, 2000. 10

[70] M. A. Laguna-Marco, D. Haskel, N. Souza-Neto, J. C. Lang, V. V. Krishnamurthy, S. Chikara, G. Cao, and M. van Veenendaal, "Orbital magnetism and spin-orbit effects in the electronic structure of bairo$_3$," *Phys. Rev. Lett.*, vol. 105, p. 216407, Nov 2010. 10, 58

[71] N. A. Bogdanov, V. M. Katukuri, H. Stoll, J. van den Brink, and L. Hozoi, "Post-perovskite cairo$_3$: A $j = \mathbf{1/2}$ quasi-one-dimensional antiferromagnet," *Phys. Rev. B*, vol. 85, p. 235147, Jun 2012. 10, 19, 47

[72] T. Nguyen and H.-C. [zur Loye], "A family of one-dimensional oxides: Sr3mlro6 (m = ni, cu, zn): Structure and magnetic properties," *Journal of Solid State Chemistry*, vol. 117, no. 2, pp. 300 – 308, 1995. 10

[73] K. Xiong, W. Liu, S. J. Teat, L. An, H. Wang, T. J. Emge, and J. Li, "New hybrid lead iodides: From one-dimensional chain to two-dimensional layered perovskite structure," *Journal of Solid State Chemistry*, vol. 230, pp. 143 – 148, 2015. 10

[74] Y. Wang, D. Walker, B.-H. Chen, and B. A. Scott, "High-pressure synthesis of one-dimensional alkaline-earth palladates," *Journal of Alloys and Compounds*, vol. 285, no. 1, pp. 98 – 104, 1999. 10

[75] A. Abragam and B. Bleaney, "Electron paramagnetic resonance of transition ions," 1970. 13

[76] S. R. White, "Density matrix formulation for quantum renormalization groups," *Phys. Rev. Lett.*, vol. 69, pp. 2863–2866, Nov 1992. 15, 31, 129

[77] S. R. White, "Density-matrix algorithms for quantum renormalization groups," *Phys. Rev. B*, vol. 48, pp. 10345–10356, Oct 1993. 15, 31, 48

[78] S. R. White, "Density matrix renormalization group algorithms with a single center site," *Phys. Rev. B*, vol. 72, p. 180403, Nov 2005. 15, 32, 50, 129

[79] D. Jérome, T. M. Rice, and W. Kohn, "Excitonic insulator," *Phys. Rev.*, vol. 158, pp. 462–475, Jun 1967. 17, 28, 32, 36, 41, 43, 47, 52, 54

[80] B. I. HALPERIN and T. M. RICE, "Possible anomalies at a semimetal-semiconductor transistion," *Rev. Mod. Phys.*, vol. 40, pp. 755–766, Oct 1968. 17, 28, 32, 36, 41, 43, 47, 52, 54

[81] B. Halperin and T. Rice, "The excitonic state at the semiconductor-semimetal transition**a summary of thin paper was presented at the meeting of the american physical society, at toronto, canada, june 1967.," vol. 21, pp. 115 – 192, 1968. 17, 28, 32, 36, 41, 43, 47, 52, 54

[82] L. Du, X. Sheng, H. Weng, and X. Dai, "The electronic structure of NaIrO 3 , mott insulator or band insulator?," *EPL (Europhysics Letters)*, vol. 101, p. 27003, jan 2013. 17

[83] J. Kuneš, "Excitonic condensation in systems of strongly correlated electrons," *Journal of Physics: Condensed Matter*, vol. 27, p. 333201, jul 2015. 20, 28, 35, 52

[84] T. Kaneko and Y. Ohta, "Roles of hund's rule coupling in excitonic density-wave states," *Phys. Rev. B*, vol. 90, p. 245144, Dec 2014. 21, 35

[85] G. Khaliullin, "Excitonic magnetism in van vleck–type d^4 mott insulators," *Phys. Rev. Lett.*, vol. 111, p. 197201, Nov 2013. 26, 29, 46

[86] S. Bhowal, S. Baidya, I. Dasgupta, and T. Saha-Dasgupta, "Breakdown of $j = 0$ nonmagnetic state in d^4 iridate double perovskites: A first-principles study," *Phys. Rev. B*, vol. 92, p. 121113, Sep 2015. 26

[87] N. F. Mott, "The transition to the metallic state," *The Philosophical Magazine: A Journal of Theoretical Experimental and Applied Physics*, vol. 6, no. 62, pp. 287–309, 1961. 28, 36

[88] R. S. Knox, "Introduction to exciton physics," pp. 183–245, 1983. 28, 36

[89] C. D. Batista, J. E. Gubernatis, J. Bonča, and H. Q. Lin, "Intermediate coupling theory of electronic ferroelectricity," *Phys. Rev. Lett.*, vol. 92, p. 187601, May 2004. 28

[90] K. Sugimoto, S. Nishimoto, T. Kaneko, and Y. Ohta, "Strong coupling nature of the excitonic insulator state in ta_2nise_5," *Phys. Rev. Lett.*, vol. 120, p. 247602, Jun 2018. 28

[91] S. Ejima, T. Kaneko, Y. Ohta, and H. Fehske, "Order, criticality, and excitations in the extended falicov-kimball model," *Phys. Rev. Lett.*, vol. 112, p. 026401, Jan 2014. 28, 38, 52

[92] K. Seki, R. Eder, and Y. Ohta, "Bcs-bec crossover in the extended falicov-kimball model: Variational cluster approach," *Phys. Rev. B*, vol. 84, p. 245106, Dec 2011. 28, 41

[93] V.-N. Phan, K. W. Becker, and H. Fehske, "Spectral signatures of the bcs-bec crossover in the excitonic insulator phase of the extended falicov-kimball model," *Phys. Rev. B*, vol. 81, p. 205117, May 2010. 28

[94] N. Kaushal, J. Herbrych, A. Nocera, G. Alvarez, A. Moreo, F. A. Reboredo, and E. Dagotto, "Density matrix renormalization group study of a three-orbital hubbard model with spin-orbit coupling in one dimension," *Phys. Rev. B*, vol. 96, p. 155111, Oct 2017. 28, 29, 32, 34, 46, 50, 52, 69

[95] N. Kaushal, A. Nocera, G. Alvarez, A. Moreo, and E. Dagotto, "Block excitonic condensate at $n = 3.5$ in a spin-orbit coupled t_{2g} multiorbital hubbard model," *Phys. Rev. B*, vol. 99, p. 155115, Apr 2019. 28, 38

[96] A. Kogar, M. S. Rak, S. Vig, A. A. Husain, F. Flicker, Y. I. Joe, L. Venema, G. J. MacDougall, T. C. Chiang, E. Fradkin, J. van Wezel, and P. Abbamonte, "Signatures of exciton condensation in a transition metal dichalcogenide," *Science*, vol. 358, no. 6368, pp. 1314–1317, 2017. 29

[97] Y. F. Lu, T. I. Larkin, R. A. W., T. T., B. A. V., K. B., and T. H., "Zero-gap semiconductor to excitonic insulator transition in ta2nise5," *Nature Communications*, vol. 8, no. 14408, 2017. 29

[98] J. P. Eisenstein and A. H. MacDonald, "Boseeinstein condensation of excitons in bilayer electron systems," *Nature*, vol. 432, pp. 691–694, 2004. 29

[99] G. W. Burg, N. Prasad, K. Kim, T. Taniguchi, K. Watanabe, A. H. MacDonald, L. F. Register, and E. Tutuc, "Strongly enhanced tunneling at total charge neutrality in double-bilayer graphene-wse_2 heterostructures," *Phys. Rev. Lett.*, vol. 120, p. 177702, Apr 2018. 29

[100] S. Fuchs, T. Dey, G. Aslan-Cansever, A. Maljuk, S. Wurmehl, B. Büchner, and V. Kataev, "Unraveling the nature of magnetism of the $5d^4$ double perovskite ba_2yiro_6," *Phys. Rev. Lett.*, vol. 120, p. 237204, Jun 2018. 29

[101] A. Nag, S. Bhowal, A. Chakraborty, M. M. Sala, A. Efimenko, F. Bert, P. K. Biswas, A. D. Hillier, M. Itoh, S. D. Kaushik, V. Siruguri, C. Meneghini, I. Dasgupta, and S. Ray, "Origin of magnetic moments and presence of spin-orbit singlets in ba_2yiro_6," *Phys. Rev. B*, vol. 98, p. 014431, Jul 2018. 29, 47

[102] M. Kusch, V. M. Katukuri, N. A. Bogdanov, B. Büchner, T. Dey, D. V. Efremov, J. E. Hamann-Borrero, B. H. Kim, M. Krisch, A. Maljuk, M. M. Sala, S. Wurmehl, G. Aslan-Cansever, M. Sturza, L. Hozoi, J. van den Brink, and J. Geck, "Observation of heavy spin-orbit excitons propagating in a nonmagnetic background: The case of $(Ba, Sr)_2yiro_6$," *Phys. Rev. B*, vol. 97, p. 064421, Feb 2018. 29, 47

[103] H. Gretarsson, H. Suzuki, H. Kim, K. Ueda, M. Krautloher, B. J. Kim, H. Yavaş, G. Khaliullin, and B. Keimer, "Observation of spin-orbit excitations and hund's multiplets in ca_2ruo_4," *Phys. Rev. B*, vol. 100, p. 045123, Jul 2019. 29

[104] T. Feldmaier, P. Strobel, M. Schmid, P. Hansmann, and M. Daghofer, "Excitonic magnetism at the intersection of spin-orbit coupling and crystal-field splitting," *arXiv*, vol. 1910.13977, 2019. 29

[105] M. Daghofer, A. Nicholson, A. Moreo, and E. Dagotto, "Three orbital model for the iron-based superconductors," *Phys. Rev. B*, vol. 81, p. 014511, Jan 2010. 30, 65

[106] T. D. Kühner and S. R. White, "Dynamical correlation functions using the density matrix renormalization group," *Phys. Rev. B*, vol. 60, pp. 335–343, Jul 1999. 32, 50, 58, 129

[107] A. Nocera and G. Alvarez, "Spectral functions with the density matrix renormalization group: Krylov-space approach for correction vectors," *Phys. Rev. E*, vol. 94, p. 053308, Nov 2016. 32, 58, 129

[108] J. Herbrych, J. Heverhagen, N. D. Patel, G. Alvarez, M. Daghofer, A. Moreo, and E. Dagotto, "Novel magnetic block states in low-dimensional iron-based superconductors," *Phys. Rev. Lett.*, vol. 123, p. 027203, Jul 2019. 34

[109] N. D. Patel, A. Nocera, G. Alvarez, A. Moreo, S. Johnston, and E. Dagotto, "Fingerprints of an orbital-selective mott phase in the block magnetic state of bafe2se3 ladders," *Communications Physics*, vol. 2, Article number: 64, June 2019. 34

[110] J. Herbrych, N. Kaushal, A. Nocera, G. Alvarez, A. Moreo, and E. Dagotto, "Spin dynamics orbital-selective mott phase in the block magnetic state of bafe2se3 ladders," *Nature Communications*, vol. 9, Article number: 3736, 2018. 34, 62

[111] S. Feng, N. D. Patel, P. Kim, J. H. Han, and N. Trivedi, "Magnetic phase transitions in quantum spin-orbital liquids," *Phys. Rev. B*, vol. 101, p. 155112, Apr 2020. 34

[112] T. Kaneko, S. Ejima, H. Fehske, and Y. Ohta, "Exact-diagonalization study of exciton condensation in electron bilayers," *Phys. Rev. B*, vol. 88, p. 035312, Jul 2013. 35

[113] P. Farkašovský, "Formation and condensation of excitonic bound states in the generalized falicov-kimball model," *Phys. Rev. B*, vol. 95, p. 045101, Jan 2017. 41

[114] K. Ohgushi, J.-i. Yamaura, H. Ohsumi, K. Sugimoto, S. Takeshita, A. Tokuda, H. Takagi, M. Takata, and T.-h. Arima, "Resonant x-ray diffraction study of the

strongly spin-orbit-coupled mott insulator $cairo_3$," *Phys. Rev. Lett.*, vol. 110, p. 217212, May 2013. 47

[115] M. M. Sala, K. Ohgushi, A. Al-Zein, Y. Hirata, G. Monaco, and M. Krisch, "$cairo_3$: A spin-orbit mott insulator beyond the $j_{\text{eff}} = 1/2$ ground state," *Phys. Rev. Lett.*, vol. 112, p. 176402, Apr 2014. 47

[116] S.-W. Kim, C. Liu, H.-J. Kim, J.-H. Lee, Y. Yao, K.-M. Ho, and J.-H. Cho, "Nature of the insulating ground state of the $5d$ postperovskite $cairo_3$," *Phys. Rev. Lett.*, vol. 115, p. 096401, Aug 2015. 47

[117] S. Calder, G.-X. Cao, S. Okamoto, J. W. Kim, V. R. Cooper, Z. Gai, B. C. Sales, M. D. Lumsden, D. Mandrus, and A. D. Christianson, "$J_{\text{eff}} = \frac{1}{2}$ mott spin-orbit insulating state close to the cubic limit in ca_4iro_6," *Phys. Rev. B*, vol. 89, p. 081104, Feb 2014. 47

[118] K. Maiti, R. S. Singh, V. R. R. Medicherla, S. Rayaprol, and E. V. Sampathkumaran, "Origin of charge density wave formation in insulators from a high resolution photoemission study of $bairo_3$," *Phys. Rev. Lett.*, vol. 95, p. 016404, Jun 2005. 47

[119] O. B. Korneta, S. Chikara, S. Parkin, L. E. DeLong, P. Schlottmann, and G. Cao, "Pressure-induced insulating state in $ba_{1-x}R_xiro_3$ (r = Gd, eu) single crystals," *Phys. Rev. B*, vol. 81, p. 045101, Jan 2010. 47

[120] M. Ye, H.-S. Kim, J.-W. Kim, C.-J. Won, K. Haule, D. Vanderbilt, S.-W. Cheong, and G. Blumberg, "Covalency-driven collapse of strong spin-orbit coupling in face-sharing iridium octahedra," *Phys. Rev. B*, vol. 98, p. 201105, Nov 2018. 47

[121] W.-G. Yin, X. Liu, A. M. Tsvelik, M. P. M. Dean, M. H. Upton, J. Kim, D. Casa, A. Said, T. Gog, T. F. Qi, G. Cao, and J. P. Hill, "Ferromagnetic exchange anisotropy from antiferromagnetic superexchange in the mixed $3d-5d$ transition-metal compound sr_3cuiro_6," *Phys. Rev. Lett.*, vol. 111, p. 057202, Aug 2013. 47

[122] R. Morrow, M. A. Susner, M. D. Sumption, and P. M. Woodward, "Magnetic structure of the quasi-one-dimensional La_3Oso_7 as determined by neutron powder diffraction," *Phys. Rev. B*, vol. 92, p. 134402, Oct 2015. 48

[123] S. V. Streltsov, G. Cao, and D. I. Khomskii, "Suppression of magnetism in $ba_5alir_2o_{11}$: Interplay of hund's coupling, molecular orbitals, and spin-orbit interaction," *Phys. Rev. B*, vol. 96, p. 014434, Jul 2017. 48

[124] Y. Wang, R. Wang, J. Kim, M. H. Upton, D. Casa, T. Gog, G. Cao, G. Kotliar, M. P. M. Dean, and X. Liu, "Direct detection of dimer orbitals in $ba_5alir_2o_{11}$," *Phys. Rev. Lett.*, vol. 122, p. 106401, Mar 2019. 48

[125] X. Chen and S. D. Wilson, "Structural evolution and electronic properties of $(Sr_{1-x}Ca_x)_{2-y}iro_{4+z}$ spin-orbit-assisted insulators," *Phys. Rev. B*, vol. 94, p. 195115, Nov 2016. 48

[126] K. Matsuhira, K. Nakamura, Y. Yasukuni, Y. Yoshimoto, D. Hirai, and Z. Hiroi, "Nonlinear conductivity of geometrically frustrated iridate ca5ir3o12," *Journal of the Physical Society of Japan*, vol. 87, no. 1, p. 013703, 2018. 48

[127] Z. Q. Mao, T. He, M. M. Rosario, K. D. Nelson, D. Okuno, B. Ueland, I. G. Deac, P. Schiffer, Y. Liu, and R. J. Cava, "Quantum phase transition in quasi-one-dimensional $baru_6o_{12}$," *Phys. Rev. Lett.*, vol. 90, p. 186601, May 2003. 48

[128] W. Kobayashi, "Transport properties of quasi-one-dimensional kru_4o_8," *Phys. Rev. B*, vol. 79, p. 155116, Apr 2009. 48

[129] S. R. White and R. M. Noack, "Real-space quantum renormalization groups," *Phys. Rev. Lett.*, vol. 68, pp. 3487–3490, Jun 1992. 48

[130] G. Alvarez, "The density matrix renormalization group for strongly correlated electron systems: A generic implementation," *Computer Physics Communications*, vol. 180, no. 9, pp. 1572 – 1578, 2009. 58

[131] W. Ju, G.-Q. Liu, and Z. Yang, "Exotic spin-orbital mott insulating states in bairo$_3$," *Phys. Rev. B*, vol. 87, p. 075112, Feb 2013. 64

[132] J. Gunasekera, Y. Chen, J. W. Kremenak, P. F. Miceli, and D. K. Singh, "Mott insulator-to-metal transition in yttrium-doped CaIrO3," *Journal of Physics: Condensed Matter*, vol. 27, p. 052201, jan 2015. 64

[133] J. Gunasekera, L. Harriger, A. Dahal, T.Heitmann, G. Vignale, and D. K. Singh, "Magnetic fluctuations driven insulator-to-metal transition in ca(ir1xrux)o3," *Scientific Reports*, vol. 5, Dec 2016. 64

[134] J. Chakraborty, "Interplay of covalency, spin-orbit coupling, and geometric frustration in the $d^{3.5}$ system ba$_3$liir$_2$o$_9$," *Phys. Rev. B*, vol. 97, p. 235147, Jun 2018. 64

[135] S. K. Panda, S. Bhowal, Y. Li, S. Ganguly, R. Valentí, L. Nordström, and I. Dasgupta, "Electronic structure and spin-orbit driven magnetism in $d^{4.5}$ insulator ba$_3$yir$_2$o$_9$," *Phys. Rev. B*, vol. 92, p. 180403, Nov 2015. 64

[136] J. Tranquada, H. Woo, T. Perring, H. Goka, G. Gu, G. Xu, M. Fujita, and K. Yamada, "Universal magnetic excitation spectrum in cuprates," *Journal of Physics and Chemistry of Solids*, vol. 67, no. 1, pp. 511 – 515, 2006. Spectroscopies in Novel Superconductors 2004. 65

[137] E. Fradkin, S. A. Kivelson, and J. M. Tranquada, "Colloquium: Theory of intertwined orders in high temperature superconductors," *Rev. Mod. Phys.*, vol. 87, pp. 457–482, May 2015. 65

[138] D. N. Basov and A. V. Chubukov *Nature Physics*, vol. 7, pp. 272–276, April 2011. 65

[139] R. M. Fernandes and A. V. Chubukov, "Low-energy microscopic models for iron-based superconductors: a review," *Reports on Progress in Physics*, vol. 80, p. 014503, nov 2016. 65

[140] Z. P. Yin, K. Haule, and G. Kotliar, "Kinetic frustration and the nature of the magnetic and paramagnetic states in iron pnictides and iron chalcogenides," *Nature Materials*, vol. 10, p. 932, 2010. 66

[141] M. D. Lumsden and A. D. Christianson, "Magnetism in fe-based superconductors," *Journal of Physics: Condensed Matter*, vol. 22, p. 203203, apr 2010. 66

[142] E. Dagotto, "Colloquium: The unexpected properties of alkali metal iron selenide superconductors," *Rev. Mod. Phys.*, vol. 85, pp. 849–867, May 2013. 66

[143] W. Li, C. Setty, X. H. Chen, and J. Hu, "Electronic and magnetic structures of chain structured iron selenide compounds," *Front. Phys.*, vol. 9, pp. 465–471, 2014. 66

[144] E. Bascones, B. Valenzuela, and M. J. Caldern, "Magnetic interactions in iron superconductors: A review," *Comptes Rendus Physique*, vol. 17, no. 1, pp. 36 – 59, 2016. Iron-based superconductors / Supraconducteurs base de fer. 66

[145] E. Dagotto and T. M. Rice, "Surprises on the way from one- to two-dimensional quantum magnets: The ladder materials," *Science*, vol. 271, no. 5249, pp. 618–623, 1996. 66

[146] K. Takubo, Y. Yokoyama, H. Wadati, S. Iwasaki, T. Mizokawa, T. Boyko, R. Sutarto, F. He, K. Hashizume, S. Imaizumi, T. Aoyama, Y. Imai, and K. Ohgushi, "Orbital order and fluctuations in the two-leg ladder materials bafe$_2X_3$ (x = S and se) and csfe$_2$se$_3$," *Phys. Rev. B*, vol. 96, p. 115157, Sep 2017. 66

[147] T. Yamauchi, Y. Hirata, Y. Ueda, and K. Ohgushi, "Pressure-induced mott transition followed by a 24-k superconducting phase in bafe$_2$s$_3$," *Phys. Rev. Lett.*, vol. 115, p. 246402, Dec 2015. 66

[148] J. Ying, H. Lei, C. Petrovic, Y. Xiao, and V. V. Struzhkin, "Interplay of magnetism and superconductivity in the compressed fe-ladder compound bafe$_2$se$_3$," *Phys. Rev. B*, vol. 95, p. 241109, Jun 2017. 66

[149] Y. Zhang, L.-F. Lin, J.-J. Zhang, E. Dagotto, and S. Dong, "Sequential structural and antiferromagnetic transitions in bafe$_2$se$_3$ under pressure," *Phys. Rev. B*, vol. 97, p. 045119, Jan 2018. 66

[150] A. Georges, L. d. Medici, and J. Mravlje, "Strong correlations from hunds coupling," *Annual Review of Condensed Matter Physics*, vol. 4, no. 1, pp. 137–178, 2013. 66

[151] J. M. Caron, J. R. Neilson, D. C. Miller, K. Arpino, A. Llobet, and T. M. McQueen, "Orbital-selective magnetism in the spin-ladder iron selenides $ba_{1-x}k_xfe_2se_3$," *Phys. Rev. B*, vol. 85, p. 180405, May 2012. 66, 81

[152] S. Dong, J.-M. Liu, and E. Dagotto, "$bafe_2Se_3$: A high T_C magnetic multiferroic with large ferrielectric polarization," *Phys. Rev. Lett.*, vol. 113, p. 187204, Oct 2014. 66

[153] M. Wang, S. J. Jin, M. Yi, Y. Song, H. C. Jiang, W. L. Zhang, H. L. Sun, H. Q. Luo, A. D. Christianson, E. Bourret-Courchesne, D. H. Lee, D.-X. Yao, and R. J. Birgeneau, "Strong ferromagnetic exchange interaction under ambient pressure in $bafe_2s_3$," *Phys. Rev. B*, vol. 95, p. 060502, Feb 2017. 66, 67, 70

[154] M. Wang, M. Yi, S. Jin, H. Jiang, Y. Song, H. Luo, A. D. Christianson, C. de la Cruz, E. Bourret-Courchesne, D.-X. Yao, D. H. Lee, and R. J. Birgeneau, "Spin waves and magnetic exchange interactions in the spin-ladder compound $rbfe_2se_3$," *Phys. Rev. B*, vol. 94, p. 041111, Jul 2016. 66, 67, 70

[155] T. Hawai, Y. Nambu, K. Ohgushi, F. Du, Y. Hirata, M. Avdeev, Y. Uwatoko, Y. Sekine, H. Fukazawa, J. Ma, S. Chi, Y. Ueda, H. Yoshizawa, and T. J. Sato, "Temperature and composition phase diagram in the iron-based ladder compounds $ba_{1-x}cs_xfe_2se_3$," *Phys. Rev. B*, vol. 91, p. 184416, May 2015. 66

[156] S. Chi, Y. Uwatoko, H. Cao, Y. Hirata, K. Hashizume, T. Aoyama, and K. Ohgushi, "Magnetic precursor of the pressure-induced superconductivity in fe-ladder compounds," *Phys. Rev. Lett.*, vol. 117, p. 047003, Jul 2016. 66

[157] J. M. Caron, J. R. Neilson, D. C. Miller, A. Llobet, and T. M. McQueen, "Iron displacements and magnetoelastic coupling in the antiferromagnetic spin-ladder compound $bafe_2se_3$," *Phys. Rev. B*, vol. 84, p. 180409, Nov 2011. 66

[158] J. Guo, S. Jin, G. Wang, S. Wang, K. Zhu, T. Zhou, M. He, and X. Chen, "Superconductivity in the iron selenide $k_xfe_2se_2$ ($0 \leq x \leq 1.0$)," *Phys. Rev. B*, vol. 82, p. 180520, Nov 2010. 66

[159] Z. Shermadini, A. Krzton-Maziopa, M. Bendele, R. Khasanov, H. Luetkens, K. Conder, E. Pomjakushina, S. Weyeneth, V. Pomjakushin, O. Bossen, and A. Amato, "Coexistence of magnetism and superconductivity in the iron-based compound $cs_{0.8}(fese_{0.98})_2$," *Phys. Rev. Lett.*, vol. 106, p. 117602, Mar 2011. 66

[160] F. Ye, S. Chi, W. Bao, X. F. Wang, J. J. Ying, X. H. Chen, H. D. Wang, C. H. Dong, and M. Fang, "Common crystalline and magnetic structure of superconducting $A_2fe_4se_5$ ($a = \mathrm{K, Rb, Cs, Tl}$) single crystals measured using neutron diffraction," *Phys. Rev. Lett.*, vol. 107, p. 137003, Sep 2011. 66

[161] M. Wang, C. Fang, D.-X. Yao, G. Tan, L. W. Harriger, Y. Song, T. Netherton, C. Zhang, M. Wang, M. B. Stone, W. Tian, J. Hu, and P. Dai, "Spin waves and magnetic exchange interactions in insulating $rb_{0.89}fe_{1.58}se_2$," *Nature Communications*, vol. 2, Article number: 1573, 2018. 66, 69, 81

[162] W. Bao, Q.-Z. Huang, G.-F. Chen, D.-M. Wang, J.-B. He, and Y.-M. Qiu, "A novel large moment antiferromagnetic order in k0.8fe1.6se2 superconductor," *Chinese Physics Letters*, vol. 28, p. 086104, aug 2011. 66

[163] Y.-Z. You, H. Yao, and D.-H. Lee, "Spin excitations of the block-antiferromagnetic state in $k_{0.8}fe_{1.6}se_2$," *Phys. Rev. B*, vol. 84, p. 020406, Jul 2011. 66

[164] R. Yu, P. Goswami, and Q. Si, "Magnetic phase diagram of an extended $J_1 - J_2$ model on a modulated square lattice and its implications for the antiferromagnetic phase of $k_yfe_xse_2$," *Phys. Rev. B*, vol. 84, p. 094451, Sep 2011. 66

[165] R. Yu and Q. Si, "Orbital-selective mott phase in multiorbital models for alkaline iron selenides $\mathbf{k}_{1-x}fe_{2-y}se_2$," *Phys. Rev. Lett.*, vol. 110, p. 146402, Apr 2013. 69

[166] K. Haule and G. Kotliar, "Coherence-incoherence crossover in the normal state of iron oxypnictides and importance of hund's rule coupling," *New Journal of Physics*, vol. 11, p. 025021, feb 2009. 69

[167] Q. Luo, G. Martins, D.-X. Yao, M. Daghofer, R. Yu, A. Moreo, and E. Dagotto, "Neutron and arpes constraints on the couplings of the multiorbital hubbard model for the iron pnictides," *Phys. Rev. B*, vol. 82, p. 104508, Sep 2010. 69

[168] J. Ren and J. Sirker, "Spinons and helimagnons in the frustrated heisenberg chain," *Phys. Rev. B*, vol. 85, p. 140410, Apr 2012. 69, 76

[169] A. Nicholson, Q. Luo, W. Ge, J. Riera, M. Daghofer, G. B. Martins, A. Moreo, and E. Dagotto, "Role of degeneracy, hybridization, and nesting in the properties of multiorbital systems," *Phys. Rev. B*, vol. 84, p. 094519, Sep 2011. 69

[170] R. Bursill, G. A. Gehring, D. J. J. Farnell, J. B. Parkinson, T. Xiang, and C. Zeng, "Numerical and approximate analytical results for the frustrated spin- 1/2 quantum spin chain," *Journal of Physics: Condensed Matter*, vol. 7, pp. 8605–8618, nov 1995. 76

[171] M. Enderle, B. Fåk, H.-J. Mikeska, R. K. Kremer, A. Prokofiev, and W. Assmus, "Two-spinon and four-spinon continuum in a frustrated ferromagnetic spin-1/2 chain," *Phys. Rev. Lett.*, vol. 104, p. 237207, Jun 2010. 76

[172] H. Onishi, "Magnetic excitations of spin nematic state in frustrated ferromagnetic chain," *Journal of the Physical Society of Japan*, vol. 84, no. 8, p. 083702, 2015. 76

[173] H. Onishi, "Effects of magnetic anisotropy on spin dynamics of ferromagnetic frustrated chain," *Journal of Physics: Conference Series*, vol. 592, p. 012109, mar 2015. 76

[174] J.-K. Bao, C.-M. Feng, Y.-K. Luo, H. Jiang, Y.-L. Sun, W.-H. Jiao, C.-Y. Shen, Z.-A. Xu, and G.-H. Cao, "Variable range hopping conductivity and spin glass behavior in spin-ladder ba0.6k0.4fe2se3single crystals," *Journal of Physics: Condensed Matter*, vol. 26, p. 026002, dec 2013. 81

[175] Z. V. Popović, M. Šćepanović, N. Lazarević, M. Opačić, M. M. Radonjić, D. Tanasković, H. Lei, and C. Petrovic, "Lattice dynamics of bafe$_2X_3$(x = S, Se) compounds," *Phys. Rev. B*, vol. 91, p. 064303, Feb 2015. 81

[176] N. Mannella, "The magnetic moment enigma in fe-based high temperature superconductors," *Journal of Physics: Condensed Matter*, vol. 26, p. 473202, oct 2014. 82

[177] H. Lu, J. R. Chamorro, C. Wan, and T. M. McQueen, "Universal single-ion physics in spinorbit-coupled d5 and d4 ions," *Inorganic Chemistry*, vol. 57, no. 22, pp. 14443–14449, 2018. 114

[178] D. D. Johnson, "Modified broyden's method for accelerating convergence in self-consistent calculations," *Phys. Rev. B*, vol. 38, pp. 12807–12813, Dec 1988. 120

[179] J. Salafranca, G. Alvarez, and E. Dagotto, "Electron-lattice coupling and partial nesting as the origin of fermi arcs in manganites," *Phys. Rev. B*, vol. 80, p. 155133, Oct 2009. 121

[180] U. Schollwöck, "The density-matrix renormalization group," *Rev. Mod. Phys.*, vol. 77, pp. 259–315, Apr 2005. 129

[181] E. Jeckelmann, "Dynamical density-matrix renormalization-group method," *Phys. Rev. B*, vol. 66, p. 045114, Jul 2002. 129

[182] H. Benthien and E. Jeckelmann, "Spin and charge dynamics of the one-dimensional extended hubbard model," *Phys. Rev. B*, vol. 75, p. 205128, May 2007. 129

[183] edited by A. Avella and F. Mancini, "Strongly correlated systems - numerical methods," *Springer Series in Solid–State Sciences 176, Berlin*, vol. 176, 2013. 132

[184] K. Tomiyasu, M. Fujita, A. I. Kolesnikov, R. I. Bewley, M. J. Bull, and S. M. Bennington, "Conversion method of powder inelastic scattering data for one-dimensional systems," *Applied Physics Letters*, vol. 94, no. 9, p. 092502, 2009. 133

Appendices

A Appendix for Chapter 2

A.1 Theorem for conservation of J_z^{eff}

As discussed in Chapter 2, to reduce the computational cost of our numerical calculations we target specific J_z^{eff} sectors. In order for J_z^{eff} to become a good quantum number, namely to achieve $[H, J_z^{eff}] = 0$, we need to choose carefully the parameters contained in H_K (both the crystal-field splittings and hopping parameters) so that they satisfy the constraints discussed in this Appendix.

H_K can be written in the a_{jm} basis explicitly as $H_K = \sum_{\langle ll' \rangle} A_l^\dagger T A_{l'} + \sum_l A_l^\dagger \tilde{\Delta} A_l$, where $A_l^\dagger = (a^\dagger_{l,\frac{3}{2},\frac{3}{2}}, a^\dagger_{l,\frac{3}{2},-\frac{1}{2}}, a^\dagger_{l,\frac{1}{2},-\frac{1}{2}}, a^\dagger_{l,\frac{3}{2},-\frac{3}{2}}, a^\dagger_{l,\frac{3}{2},\frac{1}{2}}, a^\dagger_{l,\frac{1}{2},\frac{1}{2}})$ and matrices T and $\tilde{\Delta}$ are shown on next page. This is calculated simply by using the inverse transformation of Eq. (2.4). The J_z^{eff} operator can also be written in the same basis as

$$J_z^{eff} = \sum_{ijm} (m) n_{i,j,m} \,. \tag{1}$$

Below are the constraints on the H_K parameters (asumming that the $t_{\gamma\gamma'}$ and Δ_γ are real) which are obtained after imposing explicitly the condition $[H_K, J_z^{eff}] = 0$:

- $t_{\gamma\gamma'} = 0 \; \forall \; \gamma \neq \gamma'$, i.e., no interorbital hopping,
- $t_{00} = t_{11}$, namely the hopping amplitudes of the d_{xz} and d_{yz} orbitals must be equal,
- $\Delta_0 = \Delta_1$, namely the crystal-field splittings for the d_{xz} and d_{yz} orbitals must be equal.

We have selected the parameters in H_K such that the above constraints are satisfied. These constraints forbid all scattering processes of electrons under which J_z^{eff} changes, but the hybridization between the states $(j^{eff} = 3/2, m = \pm 1/2)$ and $(j^{eff} = 1/2, m = \pm 1/2)$ is still allowed and our choice of parameters hybridize the above mentioned bands. For this reason $[(\mathbf{J}^{eff})^2, H_K] \neq 0$.

$$T = \begin{bmatrix} \frac{t_{00}+t_{11}}{2} & \frac{it_{00}-it_{11}+2t_{01}}{2\sqrt{3}} & \frac{-it_{00}+it_{11}-2t_{01}}{\sqrt{6}} & 0 & \frac{t_{12}+it_{02}}{\sqrt{3}} & \frac{t_{12}+it_{02}}{\sqrt{6}} \\ \frac{-it_{00}+it_{11}+2t_{01}}{2\sqrt{3}} & \frac{t_{00}+t_{11}+4t_{22}}{6} & \frac{-t_{00}-t_{11}+2t_{22}}{3\sqrt{2}} & \frac{t_{12}+it_{02}}{\sqrt{3}} & 0 & \frac{t_{02}+it_{12}}{\sqrt{2}} \\ \frac{it_{00}-it_{11}-2t_{01}}{\sqrt{6}} & \frac{-t_{00}-t_{11}+2t_{22}}{3\sqrt{2}} & \frac{t_{00}+t_{11}+t_{22}}{3} & \frac{t_{12}+it_{02}}{\sqrt{6}} & \frac{-t_{02}-it_{12}}{\sqrt{2}} & 0 \\ 0 & \frac{t_{12}-it_{02}}{\sqrt{3}} & \frac{t_{12}-it_{02}}{\sqrt{6}} & \frac{t_{00}+t_{11}}{2} & \frac{it_{00}-it_{11}+2t_{01}}{2\sqrt{3}} & \frac{-it_{00}+it_{11}-2t_{01}}{\sqrt{6}} \\ \frac{t_{12}-it_{02}}{\sqrt{3}} & 0 & \frac{-t_{02}-it_{12}}{\sqrt{2}} & \frac{-it_{00}+it_{11}+2t_{01}}{2\sqrt{3}} & \frac{t_{00}+t_{11}+4t_{22}}{6} & \frac{-t_{00}-t_{11}+2t_{22}}{3\sqrt{2}} \\ \frac{t_{12}-it_{02}}{\sqrt{6}} & \frac{t_{02}-it_{12}}{\sqrt{2}} & 0 & \frac{it_{00}-it_{11}-2t_{01}}{\sqrt{6}} & \frac{-t_{00}-t_{11}+2t_{22}}{3\sqrt{2}} & \frac{t_{00}+t_{11}+t_{22}}{3} \end{bmatrix}$$

$$\tilde{\Delta} = \begin{bmatrix} \frac{\Delta_0+\Delta_1}{2} & \frac{i\Delta_0-i\Delta_1}{2\sqrt{3}} & \frac{-i\Delta_0+i\Delta_1}{\sqrt{6}} & 0 & 0 & 0 \\ \frac{-i\Delta_0+i\Delta_1}{2\sqrt{3}} & \frac{\Delta_0+\Delta_1+4\Delta_2}{6} & \frac{-\Delta_0-\Delta_1+2\Delta_2}{3\sqrt{2}} & 0 & 0 & 0 \\ \frac{i\Delta_0-i\Delta_1}{\sqrt{6}} & \frac{-\Delta_0-\Delta_1+2\Delta_2}{3\sqrt{2}} & \frac{\Delta_0+\Delta_1+\Delta_2}{3} & 0 & 0 & 0 \\ 0 & 0 & 0 & \frac{\Delta_0+\Delta_1}{2} & \frac{i\Delta_0-i\Delta_1}{2\sqrt{3}} & \frac{-i\Delta_0+i\Delta_1}{\sqrt{6}} \\ 0 & 0 & 0 & \frac{-i\Delta_0+i\Delta_1}{2\sqrt{3}} & \frac{\Delta_0+\Delta_1+4\Delta_2}{6} & \frac{-\Delta_0-\Delta_1+2\Delta_2}{3\sqrt{2}} \\ 0 & 0 & 0 & \frac{i\Delta_0-i\Delta_1}{\sqrt{6}} & \frac{-\Delta_0-\Delta_1+2\Delta_2}{3\sqrt{2}} & \frac{\Delta_0+\Delta_1+\Delta_2}{3} \end{bmatrix}$$

A.2 "Good Basis" for $H_K + H_{SOC}$

In principle we can write the basis in which $H_K + H_{SOC}$ are diagonalized simultaneously. We name these new basis operators as $\tilde{a}_{k,\alpha,s}$; where k is the momentum, α is the band index, and s is the flavour of the particle, i.e., ± 1. Below is the relation between these new basis and $a_{k,j,m}$, where $a_{k,j,m} = (1/\sqrt{L}) \sum_l e^{ilk} a_{l,j,m}$:

$$\tilde{a}^\dagger_{k,0,s} = a^\dagger_{k,\frac{3}{2},\frac{3s}{2}} \,, \tag{2}$$

$$\tilde{a}^\dagger_{k,1,s} = \frac{1}{N_2(k)} a^\dagger_{k,\frac{3}{2},\frac{s}{2}} + \frac{1}{N_1(k)} a^\dagger_{k,\frac{1}{2},\frac{s}{2}} \,, \tag{3}$$

$$\tilde{a}^{\dagger}_{k,2,s} = \frac{(\epsilon_{21}(k) - 9\lambda/2) + 3\sqrt{(\epsilon_{21} - \lambda/2)^2 + 2\lambda^2}}{2\sqrt{2}\epsilon_{21}(k)N_2(k)} a^{\dagger}_{k,\frac{3}{2},\frac{s}{2}} + \frac{(\epsilon_{21}(k) - 9\lambda/2) - 3\sqrt{(\epsilon_{21} - \lambda/2)^2 + 2\lambda^2}}{2\sqrt{2}\epsilon_{21}(k)N_1(k)} a^{\dagger}_{k,\frac{1}{2},\frac{s}{2}} \quad (4)$$

$$N_{\alpha}(k) = \frac{3((\epsilon_{21}(k) - \frac{\lambda}{2})^2 + 2\lambda^2)^{1/4}(\sqrt{(\epsilon_{21}(k) - \frac{\lambda}{2})^2 + 2\lambda^2} + (-1)^{\alpha}(\epsilon_{21}(k)/3 - \frac{3\lambda}{2}))^{1/2}}{2\epsilon_{21}(k)} \quad (5)$$

where in the equations above, $\epsilon_{21}(k) = \epsilon_2(k) - \epsilon_1(k)$.

Using these relations, we calculated the bands for the non-interacting case and the $\lambda_c(U = 0)$ for metal-insulator transition, as discussed in Sec. 2.3.1.

A.3 OSMP in the intermediate and strong U coupling limit

As discussed in Chapter 2 we found the OSMP in the intermediate and strong coupling regions at small λ, by calculating occupation densities in the t_{2g} basis. In the OSMP region the d_{xy} orbital is filled with nearly one electron per site while $d_{xz(yz)}$ have nearly 1.5 filling. As shown in Fig. 1, we noticed that the EXI regime starts appearing at relatively lower values of λ in the strong U coupling region.

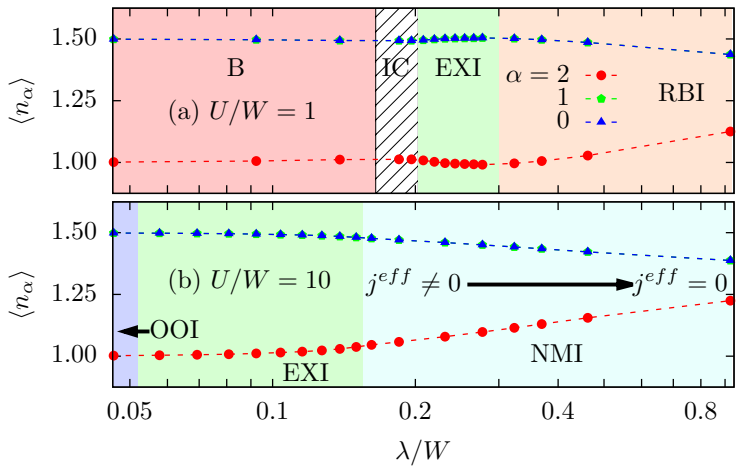

Figure 1: Occupations of the t_{2g} orbital states corresponding to (a) $U/W = 1$ (intermediate coupling) and (b) $U/W = 10$ (strong coupling). To a good approximation, the excitonic condensate phase behaves similarly as the Block (OSMP) phase, namely with one orbital having occupation of approximately one electron.

B Appendix for Chapter 3

B.1 Atomic limit

Before describing our results for chains and planes, we will discuss in detail the atomic limit of our Hamiltonian to introduce to the readers particular aspects of the t_{2g}^4 system. The magnetic properties in the $n = 4$ case with a finite spin-orbit coupling are fascinating because in the atomic limit the ground state is a singlet having $J_{\text{eff}} = 0$ for any finite value of λ/U. Only at $\lambda = 0$, the $J_{\text{eff}} = 0, 1, 2$ states are degenerate in the ground state manifold. Figure 2(a) shows the energies of the excited states relative to the $J_{\text{eff}} = 0$ ground state. The evolution of magnetic moments and occupations in the single-particle spin-orbit (j_{eff}, m) states is displayed in Fig. 2(b). Note that j_{eff} is the effective total angular momentum of the electron and m is the projection along the z-axis. Sometimes the quantum number j_{eff} will be denoted as j, if it appears as subindex.

The jj coupling limit ($\lambda/U >> 1$) can be understood by diagonalizing the spin-orbit coupling term, as discussed in Chapter 2. For $n = 4$ the ground state has all $j_{\text{eff}} = 3/2$ states fully occupied, and all $j_{\text{eff}} = 1/2$ states empty (i.e. $|GS\rangle_{jj} = a^\dagger_{\frac{3}{2},\frac{-3}{2}} a^\dagger_{\frac{3}{2},\frac{3}{2}} a^\dagger_{\frac{3}{2},\frac{-1}{2}} a^\dagger_{\frac{3}{2},\frac{1}{2}} |0\rangle$) leading to a total $J_{\text{eff}} = 0$. The first excited state is located with a gap $3\lambda/2$, as shown in Fig. 2(a). Also it can be checked that $_{jj} < GS|\mathbf{L}^2|GS >_{jj} = _{jj} < GS|\mathbf{S}^2|GS >_{jj} = 4/3$. On the other hand, in the LS coupling limit only one-third fraction of the $(j_{\text{eff}} = 1/2, m)$ states is occupied, with both the magnitudes of S and L being 1.

The information presented above in the atomic limit is relevant for cases with $U/W \ll 1$ and a finite spin-orbit coupling, to find out in which limit the system is located. For example, recently compounds with isolated $RuCl_6$ octahedra exhibited a single-ion physics with a non-magnetic $J_{\text{eff}} = 0$ state [177].

B.2 Spin-orbit exciton operators in the LS coupling limit

Let us discuss first the spin-orbit exciton operators in the LS coupling limit i.e. $(U >> t, \lambda)$. In the atomic limit, at $\lambda = 0$, the low-energy space has $L = 1$ and $S = 1$ with 9-fold

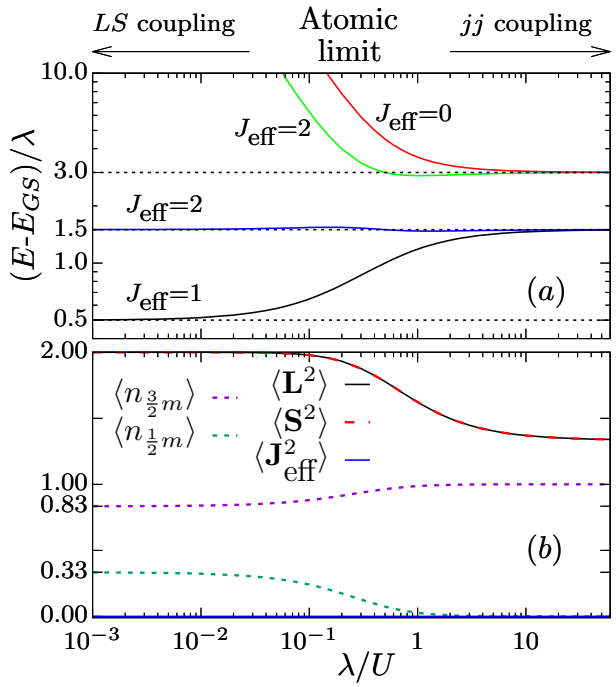

Figure 2: Panel (a) shows the energies of excited states with respect to the ground state energy denoted by E_{GS}. In panel (b), the occupation in the (j, m) states and the local moments are shown. For the plots in this figure, $U = 1$ is fixed and λ varies. The results illustrate the evolution from the LS coupling to the jj coupling regimes.

degeneracy. The $(S = 0, L = 2)$ and $(S = 0, L = 0)$ states form higher energy manifolds located at energies $U/2$ and $5U/2$ (with respect to the ground state). In the limit of $U >> \lambda$, the $(S = 1, L = 1)$ manifold splits into $J_{eff} = 0$, 1, and 2 manifolds with degeneracies 1, 3, and 5. To investigate the action of our exciton operators in the strong coupling limit, below we write these exciton operators ($\Delta^{\dagger\tilde{j},m'}_{j,m}$) as a matrix spanned by the $J_{\rm eff} = 0$, 1, and 2 states of the $(S = 1, L = 1)$ manifold, where the states are denoted as $|m_{J_{\rm eff}}, J_{\rm eff}\rangle$:

$$\Delta^{\dagger\frac{3}{2},\frac{1}{2}}_{\frac{1}{2},\frac{1}{2}} =$$

	$\lvert 0,0\rangle$	$\lvert$-1,1$\rangle$	$\lvert 0,1\rangle$	$\lvert 1,1\rangle$	$\lvert$-2,2$\rangle$	$\lvert$-1,2$\rangle$	$\lvert 0,2\rangle$	$\lvert 1,2\rangle$	$\lvert 2,2\rangle$
$\langle\ 0,0\rvert$	0	0	$-\frac{1}{2\sqrt{3}}$	0	0	0	$\frac{1}{6}$	0	0
$\langle$-1,1$\rvert$	0	0	0	0	0	0	0	0	0
$\langle\ 0,1\rvert$	$-\frac{1}{\sqrt{3}}$	0	0	0	0	0	0	0	0
$\langle\ 1,1\rvert$	0	0	0	0	0	0	0	0	0
$\langle$-2,2$\rvert$	0	0	0	0	$-\frac{\sqrt{2}}{3}$	0	0	0	0
$\langle$-1,2$\rvert$	0	0	0	0	0	0	0	0	0
$\langle\ 0,2\rvert$	$-\frac{1}{3}$	0	$-\frac{1}{\sqrt{6}}$	0	0	0	$\frac{1}{3\sqrt{2}}$	0	0
$\langle\ 1,2\rvert$	0	0	0	$-\frac{1}{\sqrt{2}}$	0	0	0	$\frac{1}{3\sqrt{2}}$	0
$\langle\ 2,2\rvert$	0	0	0	0	0	0	0	0	0

$$\Delta^{\dagger\frac{3}{2},\frac{-1}{2}}_{\frac{1}{2},\frac{-1}{2}} =$$

	$\lvert 0,0\rangle$	$\lvert$-1,1$\rangle$	$\lvert 0,1\rangle$	$\lvert 1,1\rangle$	$\lvert$-2,2$\rangle$	$\lvert$-1,2$\rangle$	$\lvert 0,2\rangle$	$\lvert 1,2\rangle$	$\lvert 2,2\rangle$
$\langle\ 0,0\rvert$	0	0	$\frac{1}{2\sqrt{3}}$	0	0	0	$\frac{1}{6}$	0	0
$\langle$-1,1$\rvert$	0	0	0	0	0	0	0	0	0
$\langle\ 0,1\rvert$	$\frac{1}{\sqrt{3}}$	0	0	0	0	0	0	0	0
$\langle\ 1,1\rvert$	0	0	0	0	0	0	0	0	0
$\langle$-2,2$\rvert$	0	0	0	0	0	0	0	0	0
$\langle$-1,2$\rvert$	0	$\frac{1}{\sqrt{2}}$	0	0	0	$\frac{1}{3\sqrt{2}}$	0	0	0
$\langle\ 0,2\rvert$	$-\frac{1}{3}$	0	$\frac{1}{\sqrt{6}}$	0	0	0	$\frac{1}{3\sqrt{2}}$	0	0
$\langle\ 1,2\rvert$	0	0	0	0	0	0	0	0	0
$\langle\ 2,2\rvert$	0	0	0	0	0	0	0	0	$-\frac{\sqrt{2}}{3}$

$$\Delta^{\dagger\frac{3}{2},\frac{1}{2}}_{\frac{1}{2},\frac{-1}{2}} = \begin{array}{c} \\ \langle\ 0,0| \\ \langle\text{-}1,1| \\ \langle\ 0,1| \\ \langle\ 1,1| \\ \langle\text{-}2,2| \\ \langle\text{-}1,2| \\ \langle\ 0,2| \\ \langle\ 1,2| \\ \langle\ 2,2| \end{array} \begin{array}{c} \begin{array}{ccccccccc} |0,0\rangle & |\text{-}1,1\rangle & |0,1\rangle & |1,1\rangle & |\text{-}2,2\rangle & |\text{-}1,2\rangle & |0,2\rangle & |1,2\rangle & |2,2\rangle \end{array} \\ \begin{bmatrix} 0 & 0 & 0 & \frac{-1}{2\sqrt{6}} & 0 & 0 & 0 & \frac{-1}{2\sqrt{6}} & 0 \\ \frac{-i}{\sqrt{6}} & 0 & 0 & 0 & 0 & 0 & 0 & 0 & 0 \\ 0 & 0 & 0 & 0 & 0 & 0 & 0 & 0 & 0 \\ 0 & 0 & 0 & 0 & 0 & 0 & 0 & 0 & 0 \\ 0 & \frac{i}{\sqrt{2}} & 0 & 0 & 0 & \frac{i}{3\sqrt{2}} & 0 & 0 & 0 \\ \frac{i}{\sqrt{6}} & 0 & 0 & 0 & 0 & 0 & 0 & 0 & 0 \\ 0 & 0 & 0 & \frac{-1}{2\sqrt{3}} & 0 & 0 & 0 & \frac{-1}{2\sqrt{3}} & 0 \\ 0 & 0 & 0 & 0 & 0 & 0 & 0 & 0 & \frac{-2}{3} \\ 0 & 0 & 0 & 0 & 0 & 0 & 0 & 0 & 0 \end{bmatrix} \end{array}$$

$$\Delta^{\dagger\frac{3}{2},\frac{-1}{2}}_{\frac{1}{2},\frac{1}{2}} = \begin{array}{c} \\ \langle\ 0,0| \\ \langle\text{-}1,1| \\ \langle\ 0,1| \\ \langle\ 1,1| \\ \langle\text{-}2,2| \\ \langle\text{-}1,2| \\ \langle\ 0,2| \\ \langle\ 1,2| \\ \langle\ 2,2| \end{array} \begin{array}{c} \begin{array}{ccccccccc} |0,0\rangle & |\text{-}1,1\rangle & |0,1\rangle & |1,1\rangle & |\text{-}2,2\rangle & |\text{-}1,2\rangle & |0,2\rangle & |1,2\rangle & |2,2\rangle \end{array} \\ \begin{bmatrix} 0 & \frac{i}{2\sqrt{6}} & 0 & 0 & 0 & \frac{-i}{2\sqrt{6}} & 0 & 0 & 0 \\ 0 & 0 & 0 & 0 & 0 & 0 & 0 & 0 & 0 \\ 0 & 0 & 0 & 0 & 0 & 0 & 0 & 0 & 0 \\ \frac{-1}{\sqrt{6}} & 0 & 0 & 0 & 0 & 0 & 0 & 0 & 0 \\ 0 & 0 & 0 & 0 & 0 & 0 & 0 & 0 & 0 \\ 0 & 0 & 0 & 0 & \frac{i\sqrt{2}}{3} & 0 & 0 & 0 & 0 \\ 0 & \frac{i}{2\sqrt{3}} & 0 & 0 & 0 & \frac{-i}{2\sqrt{3}} & 0 & 0 & 0 \\ \frac{-1}{\sqrt{6}} & 0 & 0 & 0 & 0 & 0 & 0 & 0 & 0 \\ 0 & 0 & 0 & \frac{-1}{\sqrt{2}} & 0 & 0 & 0 & \frac{1}{3\sqrt{2}} & 0 \end{bmatrix} \end{array}$$

Using the matrices shown above and the definitions of the Triplon operators as $\mathbf{T}^\dagger_n|0,0\rangle=|n,1\rangle$ and the Quintuplon operators as $\mathbf{Q}^\dagger_l|0,0\rangle=|l,2\rangle$, where $n \in \{0,\pm1\}$ and $l \in \{0,\pm1,\pm2\}$, then we can write that $\Delta^{\dagger 3/2,s/2}_{1/2,s/2}|0,0\rangle = (s\frac{\mathbf{T}^\dagger_0}{\sqrt{3}} - \frac{\mathbf{Q}^\dagger_0}{3})|0,0\rangle$, $\Delta^{\dagger 3/2,1/2}_{1/2,-1/2}|0,0\rangle = (-\iota\frac{\mathbf{T}^\dagger_{-1}}{\sqrt{6}} + \iota\frac{\mathbf{Q}^\dagger_{-1}}{\sqrt{6}})|0,0\rangle$, and $\Delta^{\dagger 3/2,-1/2}_{1/2,1/2}|0,0\rangle = (-\frac{\mathbf{T}^\dagger_1}{\sqrt{6}} - \frac{\mathbf{Q}^\dagger_1}{\sqrt{6}})|0,0\rangle$. The above equations show that these conventional electron-hole pair excitation operators when acting on the $|J_{\text{eff}}=0\rangle$

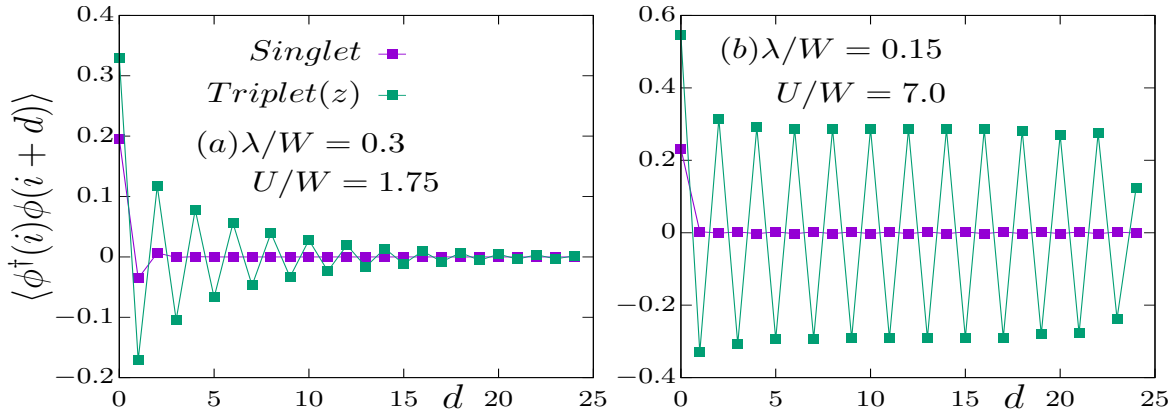

Figure 3: Panels (a) and (b) show the exciton-exciton correlation in the singlet and the z-component of the triplet channels for the cases $(\lambda/W, U/W) = (0.3, 1.75)$ and $(0.15, 7.0)$, respectively. A system size $L = 32$ is used, and site $i = 8$ is fixed.

ground state leads to local Triplon and Quintuplon excitations in the strong coupling limit, and this explains the presence of two bands in the exciton pair-pair susceptibility strong-coupling calculations shown in the main text.

B.3 Condensation of excitons in the triplet channel

For the exciton $\Delta^{\dagger 3/2m'}_{1/2m}$, m and m' can take two values, $\{\pm 1/2\}$, which leads to singlet and triplet channels for the condensation. We define the exciton operators in both channels as follows:

$$\phi_s(i) = \sum_m \Delta^{\dagger 3/2m}_{1/2m}(i), \tag{6}$$

$$\boldsymbol{\phi}_t(i) = \sum_m \Delta^{\dagger 3/2m}_{1/2m'}(i)\boldsymbol{\tau}_{mm'}. \tag{7}$$

Figure 3 displays the excitonic correlation in the channels indicated in the caption, using a $L = 32$ sites chain, for the two $(\lambda/W, U/W)$ points chosen in the DMRG phase diagram corresponding to the BCS $(0.3, 1.75)$ and BEC $(0.15, 7.0)$ regions. The correlations are measured with respect to the 8th-site from the left boundary. It is clear that the excitons condense in the triplet channel in both the BCS and BEC regimes. However, as concluded in the main text using the momentum distribution function of excitons, in the BCS regime the

triplet local-exciton correlation decays fast with distance while it shows nearly long-range order characteristics in the BEC regime.

B.4 Details of $A_{jm}(q,\omega)$ calculations

We used the DMRG-correction vector target method to calculate the single-particle spectral function $A_{jm}(q,\omega-\mu)$. The chemical potential is calculated using $\mu=(E_{N+1}-E_{N-1})/2$, where E_N is ground state energy of the N-particle system. The spectral function below and above μ is calculated using the following formulas, with a fixed broadening $\eta=0.1$ eV:

$$A_{jm}(i,c,\omega<\mu)=-\frac{1}{\pi}Im[\langle\Psi_G|a^{\dagger}_{jm,i}\frac{1}{-\omega-H+E_G+\iota\eta}a_{jm,c}|\Psi_G\rangle], \tag{8}$$

$$A_{jm}(i,c,\omega>\mu)=-\frac{1}{\pi}Im[\langle\Psi_G|a_{jm,i}\frac{1}{\omega-H+E_G+\iota\eta}a^{\dagger}_{jm,c}|\Psi_G\rangle]. \tag{9}$$

In the equations above, i and c are sites. We fixed $c=L/2$ at the center, and calculated $A_{jm}(i,c,\omega)$ for all other sites i's. Then, we employed the following approximation to reduce the computational cost:

$$A_{jm}(q,\omega)=\frac{1}{L}\sum_i e^{\iota(i-c)q}(A_{jm}(i,c,\omega<\mu)+A_{jm}(i,c,\omega>\mu)) \tag{10}$$

To calculate the density of states $\rho_{jm}(\omega)$, we used $\rho_{jm}(\omega)=A_{jm}(c,c,\omega<\mu)+A_{jm}(c,c,\omega>\mu)$.

B.5 Hartree-Fock calculations on two-dimensional lattices and extra results

All the four-fermionic terms in the Hubbard interaction of the Hamiltonian are treated under the Hartree-Fock approximation, where the single-particle density matrix expectation values $\langle c^{\dagger}_{i\alpha\sigma}c_{i\beta\sigma'}\rangle$ serve as order parameters at each site i (α,β are orbitals and σ,σ' are spin projection indexes). We reach self-consistency iteratively in the order parameters while

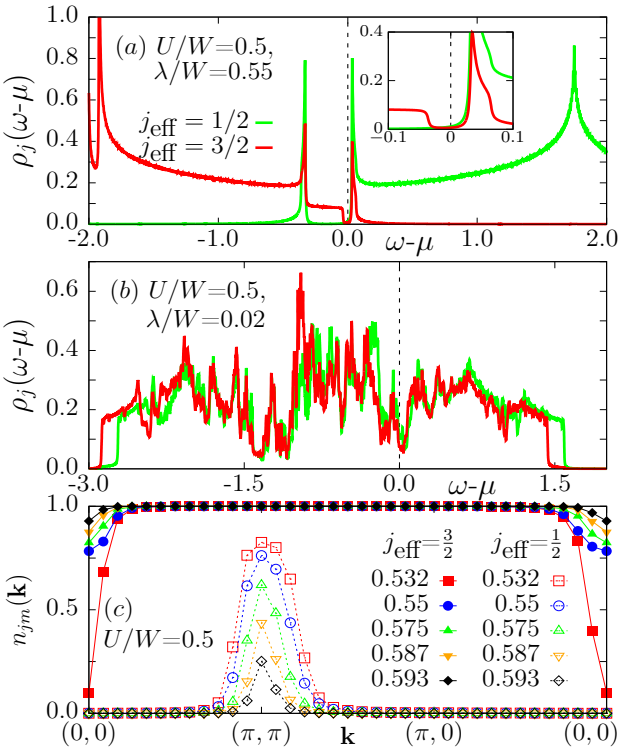

Figure 4: The density of states, $\rho_j(\omega - \mu)$, in the Excitonic Insulator and IC-SDW regions is shown in panels (a) and (b), respectively. Panel (c) contains the momentum distribution funtion for electrons $n_{jm}(\mathbf{k})$ for various values of λ. $U/W = 0.5$ is fixed for all the results in the panels above. In panel (c), a system size 24×24 is used and $m = 1/2$ is fixed.

tuning the chemical potential μ accordingly to attain the required electronic density. Given the many order parameters, converged results often require using 10-20 initial random initial configurations and inspecting the lowest energy achieved after the iterative process, searching for patterns that are then uniformized and test for their energy. Often also converged results at other couplings are used as seeds at new couplings, until a consistent phase diagram emerges. The modified Broyden's method was used to gain fast convergence [178].

The single-particle density of states (DOS) provides further evidence for the existence of the excitonic condensate. Figure 4(a) and (b) show the DOS $\rho_j(\omega - \mu)$, at fixed $U/W = 0.5$. We chose $\lambda/W = 0.02$ and $\lambda/W = 0.55$ corresponding to the IC-SDW and excitonic

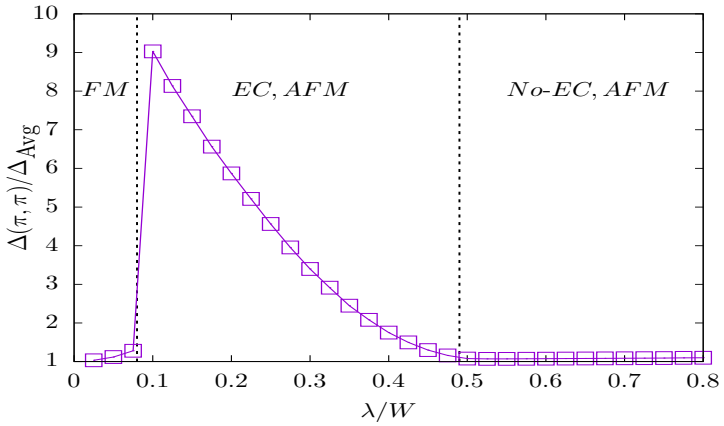

Figure 5: Ratio of excitons number at momentum $\mathbf{q} = (\pi, \pi)$ and number of excitons per momentum point is shown as a indicator of the region where excitonic condensation is present. System size 16×16 is used and $U/W = 2.25$ is fixed.

condensate phases, respectively. As shown in Fig. 4(b), at $\lambda/W = 0.02$ a finite density-of-states at the chemical potential is present for both bands $j_{\rm eff} = 3/2$ and $j_{\rm eff} = 1/2$ indicating that the system is metallic in the IC-SDW phase. In the excitonic condensate phase, a small gap is present near the chemical potential in both the bands due to the condensation of excitons. The continous distribution in eigenenergies was attained by solving 24×24 lattices with 48×48 twisted boundary conditions [179]. Two peaks arising from the small hole pocket of the $j_{\rm eff} = 1/2$ states and electron pocket ot the $j_{\rm eff} = 3/2$ states are also visible. The inset shows the magnified $\rho_j(\omega - \mu)$ near the chemical potential. To discuss the evolution of these hole and electron pockets, as the system crossovers from the BCS to BEC limit, we show the momentum distribution function of electrons $n_{jm}(\mathbf{k})$ in Fig. 4(c). The hole pocket is present at $\mathbf{k} = (0, 0)$ in the $j_{\rm eff} = 3/2$ band and the electron pocket is at $\mathbf{k} = (\pi, \pi)$ in the $j_{\rm eff} = 1/2$ band. The nesting vector between these pockets also explains the ordering momentum of the excitons. As λ increases, we noticed a gradual decrease in both electron and hole pockets which indicates that the number of carriers decreases as the system crossovers from the BCS to BEC limits. In Fig. 5, the ratio of number of excitons at momentum $\mathbf{q} = (\pi, \pi)$ and average number of excitons (i.e. $\Delta_{\rm Avg} = \frac{1}{L^2}\sum_{\mathbf{q}} \Delta(\mathbf{q})$) is shown, fixing U/W to 2.25. It is clear that Excitonic condensation is present only for $\lambda/W \in (0.1, 0.5)$. As discussed in the

main paper the spurious AFM phase present in strong coupling and large λ (i.e. in the upper right corner of the phase diagram) does not have excitonic condensation as shown in Fig. 5. It should be also noticed that $\Delta(\pi,\pi)/\Delta_{\mathrm{Avg}}$ smoothly goes to zero as λ is increased which indicates toward the continuous phase transition between the AFM+EC and AFM+No-EC phases, in our mean field theory calculation.

C Appendix for Chapter 4

C.1 Two sites problem in strong coupling ($\lambda = 0$)

In this section, we discuss the 2-sites three-orbital Hubbard model in the strong coupling limit ($U/t >> 1$) for $n = 3.5$ i.e a total of 7 electrons. Before discussing further details, below we show the Hubbard interaction term of the Hamiltonian in the rotationally invariant form (we have used $U^{'} = U - 2J_H$) which we use to calculate the energy of each atom given the occupation (N), spin moment (S), and orbital moment (L):

$$H_{int} = (U - 3J_H)\frac{N(N-1)}{2} + J_H(\frac{5}{2}N - 2S^2 - \frac{L^2}{2}). \tag{11}$$

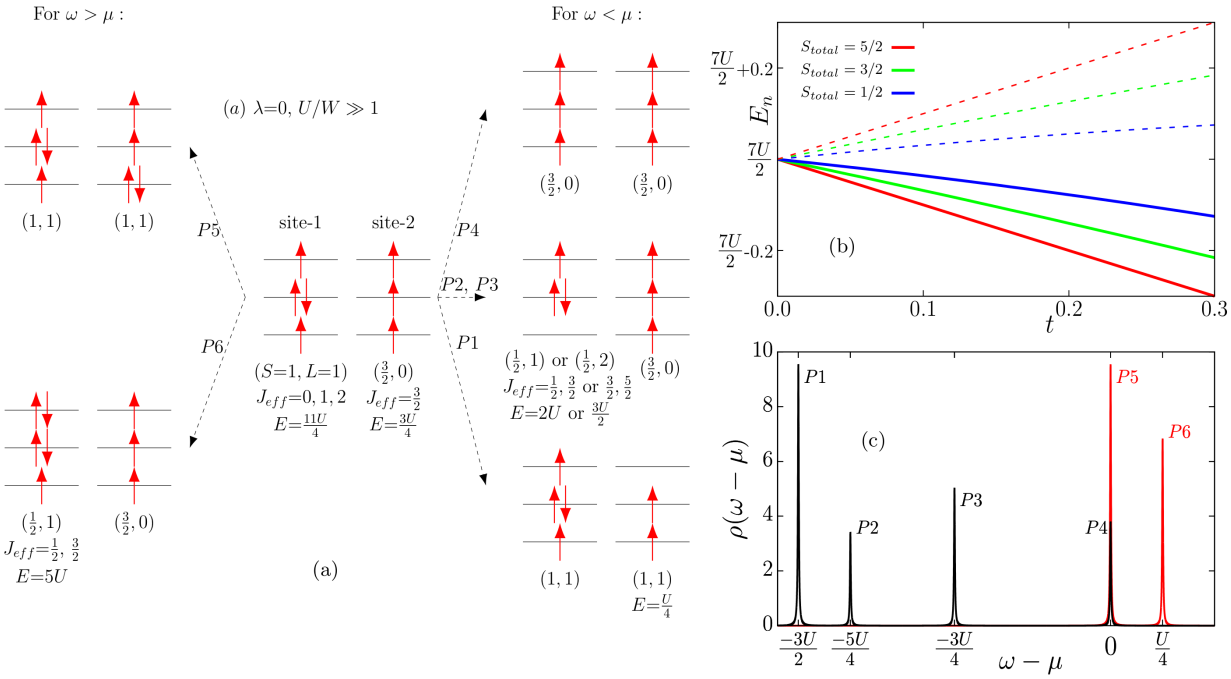

Figure 6: In panel (a), we provide a pictorial representation of the states leading to excitations in the single-particle density-of-states. Panel (b) shows the evolution of the low-energy states as the hopping is increased, for a 2-sites system in the strong coupling limit. In panel (c), $\rho(\omega)$ is shown for a 2-sites system in the strong coupling limit. A broadening $\eta = 0.05$ is used.

If we work at hopping $t = 0$, atomic limit, the ground state (GS) of the 2-sites system consists only of d^3 and d^4 sites which have (S, L)=$(3/2, 0)$ and $(1, 1)$, respectively. Using Eq.(11), the total energy $E = E_1 + E_2$ can be calculated to be $7U/2$. The total spin moment $S_{total} = S_1 + S_2$ of the GS can be $\{1/2, 3/2, 5/2\}$ and the total orbital moment L_{total} is 1.

Now to understand the effect of a nonzero kinetic energy, we perform exact diagonalization of the 2-site clusters with finite hopping. As soon as we turn on the hopping, we noticed the degeneracy in S_{total} breaks, as shown in Fig. 6(b). Interestingly all S_{total} manifolds splits into their high-energy anti-bonding (dashed lines) and low-energy bonding (solid lines) states. The GS for finite hopping has a saturated total spin moment $S_{total} = 5/2$, thus the GS has ferromagnetic ordering. The GS state has a degeneracy $6 \times 3 = 18$ fold, where "6" and "3" arise from $SU(2)$-symmetries in the spin sector of the $S = 5/2$ and $L = 1$ spaces. We also noticed that for $U/t >> 1$, for all S_{total} manifolds, the energies for the bonding (-) and anti-bonding (+) states change linearly with t as $\frac{7U}{2} \pm \tilde{t}$, where the $\tilde{t}$ for $S_{total} = 5/2$, $3/2$, $1/2$ manifolds are t, $\frac{2}{3}t$, and $\frac{1}{3}t$, respectively.

The presence of bands near the chemical potential is indeed confirmed by the density-of-state calculations performed on 4 and 16 sites systems using Lanczos and DMRG techniques, as shown in Chapter 4. We also noticed that the density-of-states of the 2-sites system can explain most of the features present in $\rho(\omega)$ of the 4-site clusters in strong coupling limit. In Fig. 6(c) we show the $\rho(\omega - \mu)$ for the 2-site cluster in the strong coupling limit, and in Fig. 6(a) we show all the "N+1" and "N-1" particle states leading to excitations above and below the chemical potential, respectively. For 4-site clusters, we observed that these peaks are present nearly at the same values $\omega's$ in terms of U, as shown in Chapter 4.

C.2 On-site Interaction in the spin-orbit basis

In this section, we present the on-site Hubbard interaction term of the Hamiltonian written in the spin-orbit basis. We employ the unitary transformation presented in Eq. 2.4 of the Chapter 2 to express the interaction term in the following form

$$H_{\text{int}} = H_{\frac{3}{2}} + H_{\frac{1}{2}} + H_{\frac{1}{2},\frac{3}{2}}, \tag{12}$$

where the $H_{\frac{3}{2}}$ ($H_{\frac{1}{2}}$) term contains the Hubbard interaction in the $j_{\text{eff}} = \frac{3}{2}$ ($j_{\text{eff}} = \frac{1}{2}$) sector, while the $H_{\frac{1}{2},\frac{3}{2}}$ term contains the interaction between electrons of the $j_{\text{eff}} = \frac{3}{2}$ and $j_{\text{eff}} = \frac{1}{2}$ sectors. We calculated the above three terms for general (U, J_H, U') values as shown below:

$$H_{\frac{3}{2}} = (\frac{U+U'}{2}) \sum_{m=\frac{1}{2},\frac{3}{2}} n_{\frac{3}{2},m} n_{\frac{3}{2},-m} + (U' - \frac{J_H}{3}) \sum_{s=\pm 1} n_{\frac{3}{2},\frac{3s}{2}} n_{\frac{3}{2},\frac{-s}{2}} + (\frac{U}{6} - \frac{2J_H}{3} + \frac{5U'}{6}) \sum_{s=\pm 1} n_{\frac{3}{2},\frac{3s}{2}} n_{\frac{3}{2},\frac{s}{2}}$$
$$+ (\frac{U'}{6} - J_H - \frac{U}{6})(a^\dagger_{\frac{3}{2},\frac{-3}{2}} a^\dagger_{\frac{3}{2},\frac{3}{2}} a_{\frac{3}{2},\frac{-1}{2}} a_{\frac{3}{2},\frac{1}{2}} + h.c.) + (\frac{U}{6} - \frac{J_H}{3} - \frac{U'}{6})(a^\dagger_{\frac{3}{2},\frac{3}{2}} a^\dagger_{\frac{3}{2},\frac{1}{2}} a_{\frac{3}{2},\frac{-3}{2}} a_{\frac{3}{2},\frac{-1}{2}} + h.c.), \tag{13}$$

$$H_{\frac{1}{2}} = (\frac{U+2U'}{3}) n_{\frac{1}{2},\frac{1}{2}} n_{\frac{1}{2},\frac{-1}{2}}, \tag{14}$$

$$\begin{aligned}
H_{\frac{1}{2},\frac{3}{2}} = {} & U' \sum_{s=\pm 1} n_{\frac{3}{2},\frac{s}{2}} n_{\frac{1}{2},\frac{s}{2}} + (U' - \frac{2J_H}{3}) \sum_{s=\pm 1} n_{\frac{3}{2},\frac{3s}{2}} n_{\frac{1}{2},\frac{-s}{2}} + (\frac{U}{3} - J_H + \frac{2U'}{3}) \sum_{s=\pm 1} n_{\frac{3}{2},\frac{s}{2}} n_{\frac{1}{2},\frac{-s}{2}} + \\
& (\frac{U}{3} - \frac{J_H}{3} + \frac{2U'}{3}) \sum_{s=\pm 1} n_{\frac{3}{2},\frac{3s}{2}} n_{\frac{1}{2},\frac{s}{2}} + (\frac{U}{3} - \frac{2J_H}{3} - \frac{U'}{3})(a^\dagger_{\frac{3}{2},\frac{-3}{2}} a^\dagger_{\frac{1}{2},\frac{-1}{2}} a_{\frac{3}{2},\frac{3}{2}} a_{\frac{1}{2},\frac{1}{2}} + h.c.) + \\
& (\frac{U-U'}{3})(a^\dagger_{\frac{3}{2},\frac{1}{2}} a^\dagger_{\frac{1}{2},\frac{-1}{2}} a_{\frac{3}{2},\frac{-1}{2}} a_{\frac{1}{2},\frac{1}{2}} + h.c.) + \frac{J_H}{\sqrt{3}} \sum_{s=\pm 1} (i a^\dagger_{\frac{3}{2},\frac{s}{2}} a^\dagger_{\frac{1}{2},\frac{s}{2}} a_{\frac{3}{2},\frac{3s}{2}} a_{\frac{1}{2},\frac{-s}{2}} + h.c.) + \\
& (\frac{U'}{3} - J_H - \frac{U}{3}) \sum_{m=\frac{1}{2},\frac{3}{2}} (a^\dagger_{\frac{3}{2},-m} a^\dagger_{\frac{3}{2},m} a_{\frac{1}{2},\frac{-1}{2}} a_{\frac{1}{2},\frac{1}{2}} + h.c.) \\
& + \frac{J_H\sqrt{2}}{3} \sum_{s=\pm 1} (n_{\frac{3}{2},\frac{3s}{2}} a^\dagger_{\frac{3}{2},\frac{-s}{2}} a_{\frac{1}{2},\frac{-s}{2}} + h.c.) + \\
& (\frac{U' + 2J_H - U}{3\sqrt{2}})(a^\dagger_{\frac{3}{2},\frac{-3}{2}} a^\dagger_{\frac{3}{2},\frac{-1}{2}} a_{\frac{3}{2},\frac{3}{2}} a_{\frac{1}{2},\frac{1}{2}} + a^\dagger_{\frac{3}{2},\frac{-3}{2}} a^\dagger_{\frac{1}{2},\frac{-1}{2}} a_{\frac{3}{2},\frac{3}{2}} a_{\frac{3}{2},\frac{1}{2}} + h.c.) \\
& + (\frac{U' - U - 2J_H}{3\sqrt{2}}) \sum_{s=\pm 1} (n_{\frac{3}{2},\frac{3s}{2}} a^\dagger_{\frac{3}{2},\frac{s}{2}} a_{\frac{1}{2},\frac{s}{2}} + h.c.) + \\
& (\frac{U-U'}{3\sqrt{2}}) \sum_{s=\pm 1} (n_{\frac{3}{2}\frac{s}{2}} a^\dagger_{\frac{1}{2},\frac{-s}{2}} a_{\frac{3}{2},\frac{-s}{2}} + s a^\dagger_{\frac{3}{2},\frac{-3}{2}} a^\dagger_{\frac{3}{2},\frac{3}{2}} a_{\frac{3}{2},\frac{-s}{2}} a_{\frac{1}{2},\frac{s}{2}} + h.c.) \\
& + J_H \sqrt{\frac{2}{3}} \sum_{s=\pm 1} (i a^\dagger_{\frac{3}{2},\frac{s}{2}} a^\dagger_{\frac{1}{2},\frac{s}{2}} a_{\frac{3}{2},\frac{3s}{2}} a_{\frac{3}{2},\frac{-s}{2}} + h.c.).
\end{aligned} \tag{15}$$

The interaction expressed in the form above helps to arrive to interesting conclusions. For example, all the terms with $\Delta J_z^{\rm eff} \neq 0$ have coefficients $\propto (U' - (U - 2J_H))$, which implies $J_z^{\rm eff}$ is a good quantum number *only* if $U' = U - 2J_H$, namely for the rotational invariant case. Another important symmetry which is relevant for the present study is the global $U(1)$ phase symmetries for specific (j, m) sectors, i.e. the invariance of Hamiltonian under the transformation $a_{j,m} \rightarrow e^{i\phi_{j,m}} a_{j,m}$. This symmetry is related to the excitonic condensation because the excitonic order parameter $\langle \Delta^{\dagger \frac{3}{2} m'}_{\frac{1}{2} m}(i) \rangle = \langle a^{\dagger}_{i \frac{1}{2} m} a_{i \frac{3}{2} m'} \rangle$ does not preserve this $U(1)$ symmetry and transforms to $e^{i(\phi_{\frac{3}{2},m'} - \phi_{\frac{1}{2},m})} \langle \Delta^{\dagger \frac{3}{2} m'}_{\frac{1}{2} m}(i) \rangle$. We notice that these $U(1)$ symmetries, which correspond to charge conservation in the (j, m) sectors separately, are explicitly broken and preserved only for the special case $J_H = 0$ and $U = U'$.

C.3 Incommensurate Spin Density Wave

As mentioned in Chapter 4, we also found an Incommensurate Spin Density Wave (IC -SDW) metallic phase. We noticed that in the IC-SDW region, the spin ordering wave vector gradually changes as a function of U and λ. To discuss the evolution of the spin structure factor, in Fig. 7 we show $S(q)$ for three paths chosen in the phase diagram as shown in Fig. 7(d). For $\lambda = 0$, panel (a), we notice that the spin ordering vector in the IC-SDW region gradually decreases up to $q = 0$ (ferromagnetic phase) as we increase U. In panel (b) we choose a path where $U/W = 2.0$ is fixed and λ is varied: along this path we have a transition from IC-SDW to the Block Excitonic phases. For $U/W = 2.0$, the spin ordering vector starts at $q = 3\pi/2$ (at $\lambda = 0$) and decreases to $q = \pi/2$ as we enter into the block phase, and eventually transitions into a paramagnetic phase having $S(q)$ nearly constant.

In the weak coupling limit, namely small values of U/W, we notice a crossover from IC-SDW to a $j_{\rm eff} = 3/2$ metallic phase. To discuss the $S(q)$ along this crossover, we fixed $U/W = 1.0$ and increased λ, as shown in panel (c). For $U/W = 1$, firstly the spin ordering vector increases to $q = \pi$ as λ is increased. On further increasing λ, $S(q = \pi)$ decreases as the system enters into the $j_{\rm eff} = 3/2$ metallic phase.

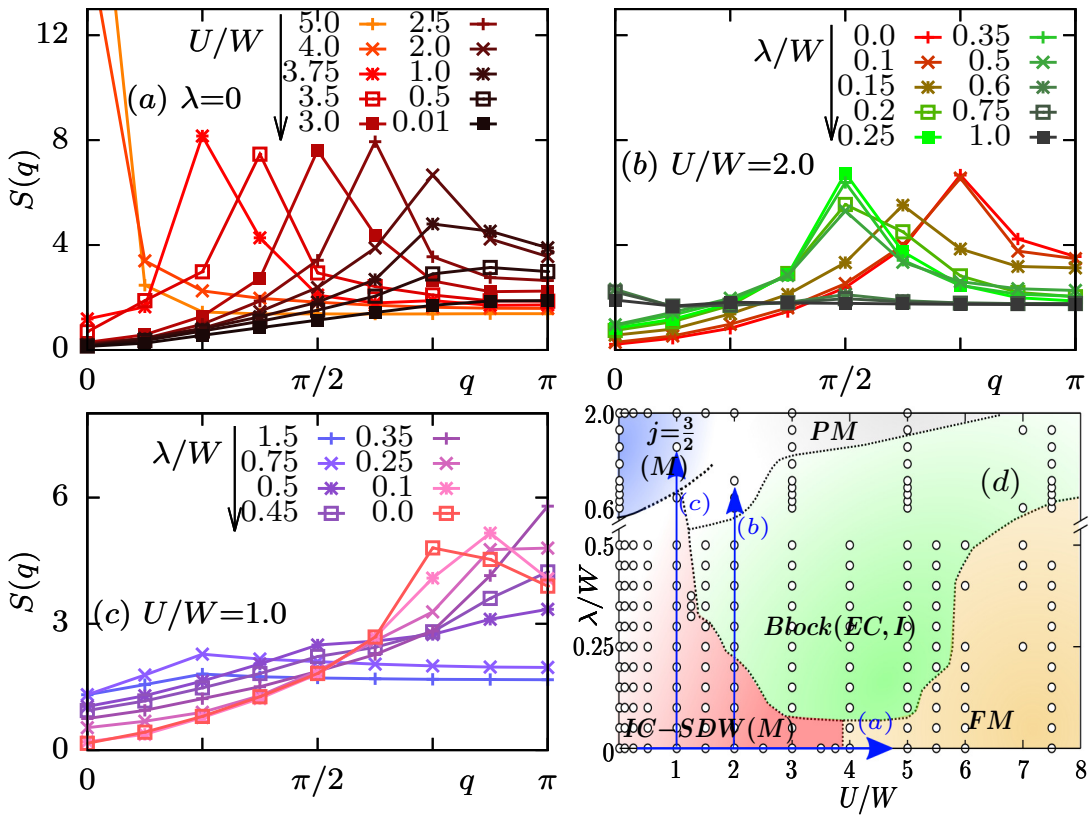

Figure 7: In panels (a,b,c), the spin structure factor ($S(q)$) is shown for three different paths in the phase diagram. The paths are shown in panel (d). All the results above are for $L = 16$ sites system.

C.4 Boundary effects

In the present Chapter 4, we focused on systems with open boundary conditions (OBC) because DMRG performs better with OBC than periodic boundary conditions (PBC). It is well known that in general OBC may induce Friedel oscillations in the local density. To investigate this aspect, we calculated the local density ($\langle n_i \rangle$) inside the block excitonic condensate phase of our focus, using $L = 32$ sites. As shown in Fig. 8(a), in the block excitonic condensate phase, which is an insulator, open boundary effects produce minimal oscillations in the local density that decays quickly approaching the center of the lattice. In other phases, primarily metallic, Friedel oscillations may induce larger oscillations.

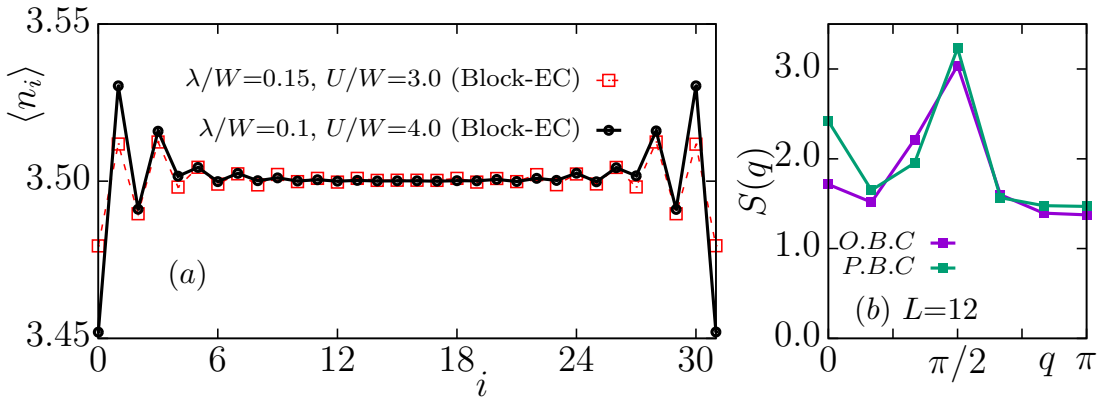

Figure 8: In panel (a), the local density ($\langle n_i \rangle$) is shown for the block excitonic condensate phase, employing a $L = 32$ sites system. Panel (b) shows the spin structure factor at the $\lambda/W = 0.15$ and $U/W = 3$ point, for an $L = 12$ sites system with both OBC and PBC.

To further investigate boundary effects on the block excitonic phase, we solved a $L = 12$ site system with PBC for couplings $\lambda/W = 0.15$ and $U/W = 3.0$. In panel (b) we present the spin structure factor using both PBC and OBC, showing the presence of block ordering using both boundary conditions.

D Appendix for Chapter 5

D.1 Methods

DMRG method. The Hamiltonians discussed in Chapter 5 were studied using primarily the density matrix renormalization group (DMRG) method [76, 180] within the single-center site approach [78], where the dynamical correlation functions are evaluated via the dynamical DMRG [181, 182, 107] i.e. calculating spectral functions directly in frequency space with the correction-vector method [106] with Krylov decomposition [107]. The computer package DMRG++ developed at ORNL was used. For a chain geometry, in both stages of the DMRG algorithm, we keep up to $M = 800$ states. This allow us to simulate accurately system sizes up to $L = 24$ sites for dynamical quantities (truncation $< 10^{-8}$ for all frequencies ω) and $L = 32$ for static quantities (truncation $< 10^{-10}$ for the GS). For the ladder geometry results, we use a standard two-site central block approach with $M = 1000$ states (truncation $< 10^{-3}$, showing that the two-leg ladder two-orbital results are qualitatively correct, because of its close resemble to the rest, but their quantitative accuracy can be further improved in future efforts). In Fig. 10 we present the scaling of our results with system size L, number of states kept M, and broadening η of Eq. (16).

Dynamical SSF. The zero temperature, $T = 0$, total spin structure factor (SSF) $S(q, \omega)$ is defined as:

$$\begin{aligned} S(q,\omega) &= \frac{1}{\pi}\sqrt{\frac{2}{L+1}}\sum_{\ell=1}^{L}\sin(q\ell)\sin(qL/2)\times \\ &\quad \mathrm{Im}\,\langle \mathrm{GS}|\tilde{S}_\ell\,\frac{1}{\omega^- - (H-\epsilon_{\mathrm{GS}})}\,\tilde{S}_{L/2}|\mathrm{GS}\rangle\,, \end{aligned} \tag{16}$$

with $\omega^- = \omega - i\eta$, and $|\mathrm{GS}\rangle$ is the ground state with energy ϵ_{GS}. In the above equation $\tilde{S}_\ell = \sum_\gamma S_{\ell,\gamma}$ is the total spin on site ℓ for the total SSF $S(q,\omega)$, or $\tilde{S}_\ell = S_{\ell,\gamma}$ for the orbital resolved SSF $S_{\gamma\gamma'}(q,\omega)$.

Furthermore, in the above equation we adopted the wave-vector definition appropriate for open boundary conditions (OBC), i.e. $q = k\pi/(L+1)$ with $k = 1, \ldots, L$. As a consequence,

in this work we used approximate (exact in the thermodynamic limit $L \to \infty$) values of the wave-vectors, e.g., $q = \pi \equiv \pi L/(L+1)$.

Localized basis representation. The eigenstates $|\phi\rangle$ of the three orbital system can be written as

$$\begin{aligned} |\phi\rangle &= \sum_{n=1}^{64^L} c_n |n\rangle \\ &= \sum_{n_0=1}^{4^L} \sum_{n_1=1}^{4^L} \sum_{n_2=1}^{4^L} c(n_0, n_1, n_2)\, |n_0\rangle \otimes |n_1\rangle \otimes |n_2\rangle\,, \end{aligned} \tag{17}$$

where $|n\rangle$ represent the orthonormal basis (particle configuration) of all orbitals and $|n_\gamma\rangle$ (with $\gamma = 0, 1, 2$) represents the particle configuration on given orbital γ. Note that $\sum_n c_n^2 = \sum_{n_1,n_2,n_3} c^2(n_1, n_2, n_3) = 1$ and $\langle n_\gamma | n'_{\gamma'} \rangle = \delta_{nn'}\delta_{\gamma\gamma'}$. One can rewrite the above equation as

$$|\phi\rangle = \sum_{j=1}^{4^L} |\tilde{c}_j\rangle \otimes |j\rangle_{\gamma=2}\,, \tag{18}$$

where $j \equiv n_2$ represents - within OSMP - the localized orbital and

$$|\tilde{c}_j\rangle = \sum_{n_0=1}^{4^L} \sum_{n_1=1}^{4^L} c(n_0, n_1, n_2)\, |n_0\rangle \otimes |n_1\rangle \tag{19}$$

are vectors. The set of $\{|\tilde{c}_j\rangle\}$ vectors represent an orthogonal vector-space with $\sum_j \langle \tilde{c}_j | \tilde{c}_j \rangle = 1$. Finally, the weight of the $|j\rangle_{\gamma=2}$ configuration in the $|\phi\rangle$ eigenstate is given by the norm of the $|\tilde{c}_j\rangle$ vector, i.e., $\langle \tilde{c}_j | \tilde{c}_j \rangle = ||\tilde{c}_j|| \equiv \tilde{c}_j^2$.

Energy contribution. In Table 1 we present the expectation values of the several terms present in the Hamiltonian for the ground state and also states which contribute to the acoustic and optical modes.

Two-orbital two-leg ladder Hamiltonian. The symmetric hoppings for the two-orbital two-leg ladder system are defined [24] in orbital space as follows [see sketch in Fig. 5.7(a)]:

$$t_x = \begin{pmatrix} 0.14769 & 0 \\ 0 & 0.27328 \end{pmatrix}, \qquad t_y = \begin{pmatrix} 0.28805 & 0.01152 \\ 0.01152 & 0.00581 \end{pmatrix},$$

Table 1: Energy contributions. Kinetic, intra- and inter-orbital interaction, Hund, and pair-hopping energy contributions to the energy of given eigenstates. The last column shows the difference between $|\mathrm{GS}\rangle$ and states within the acoustic (red color) and optical (green color) modes. Results are obtained for $L = 4$ and $U/W = 0.8$, using the Lanczos method. All numbers in units of eV.

	ϵ_{k}	ϵ_{U}	$\epsilon_{\mathrm{U}'}$	ϵ_{H}	ϵ_{P}	Total	ω_α
$\|\mathrm{GS}\rangle$	-0.027	8.006	15.280	-1.055	-0.010	22.194	
$\|\mathrm{A}\rangle$	0.007	7.993	15.280	-1.065	-0.009	22.206	0.012
$\|\mathrm{O}\rangle$	-0.031	8.081	15.262	-0.946	-0.016	22.350	0.156

$$t_{x\pm y} = \begin{pmatrix} -0.21166 & \mp 0.08430 \\ \mp 0.08430 & -0.18230 \end{pmatrix} ,$$

all expressed in units of eV. The interaction portion of the Hamiltonian is the same as in the 1D system.

D.2 Numerical details

In Fig. 9 we present the parameter dependence of our dynamical DMRG calculations for a fixed frequency $\omega = 0.03\,[\mathrm{eV}]$ (namely, "inside" the acoustic mode) and $L = 16$ sites (48 orbitals). In panel (a) we present the broadening η dependence of our calculations of $S^{zz}(q,\omega)$. It is clear from the figure that all features are properly resolved for the considered $\eta/\delta\omega = 2$. In Fig. 9(b) we present the number of states kept M dependence of our findings. We conclude that at a fixed η and L, the results do not change appreciably for $M \gtrsim 800$.

In Fig. 10(a-d) we present the finite-size analysis at several momenta q cuts through the dynamical SSF. At large $q/\pi \geq 3/4$, the results do not depend on the system size L because for this momentum only the optical mode is present in the spectrum. Since the excitations within this mode are local, the system size (and also dimensionality of the lattice) should not play a crucial role. On the other hand, at $q \leq \pi/2$ the results depend more on the system size with maximal variation at $q/\pi = 1/2$. However, this dependence does not change the

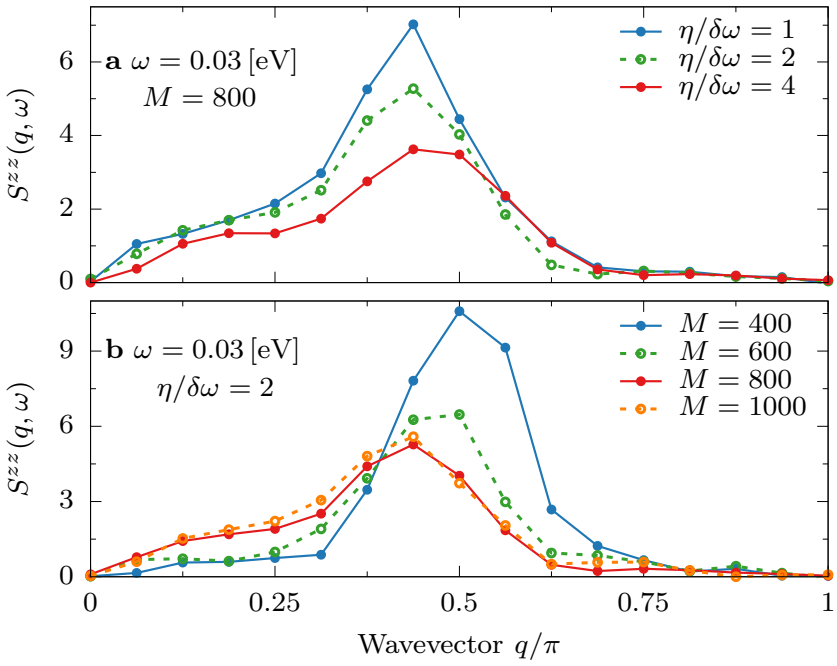

Figure 9: Parameter dependence of dynamical-DMRG simulations. (a) Broadening η and (b) number of states kept M dependence corresponding to $\omega = 0.03\,[\mathrm{eV}]$ and $L = 16$ sites. In all simulations of Chapter 5 we use $\eta/\delta\omega = 2$ and $M = 800$.

main findings of our work and it merely reflects the quasi-long-range nature of the block ordering [5]. This can be understood simply from the L-scaling of the static $S(q = \pi/2)$ shown in the inset of Fig. 10(e). For completeness in Fig. 10(e) we show the L dependence of the full momentum q resolved static SSF.

Let us finally comment on the accuracy of our results for the multi-orbital ladder geometry. Different from the chain setup, where the three orbitals where treated as a single site with a local Hilbert space of 64 states, the ladder results were obtained using a $12 \times 2 \times 2$ (rungs $\times$ legs $\times$ orbitals) lattice with a local Hilbert space of 4 states. Although such a setup have smaller memory requirements, the entanglement area law [183] heavily influences the accuracy of our results. The latter is a consequence of a large number of long-range connections (up to 7 nearest-neighbours). In Fig. 11, we present the system size L and states M scaling of the results presented in Fig. 5.7 of Chapter 5. In panel (a) we present the finite-size analysis of the static SSF in the bonding sector, $q_y/\pi = 0$, for the $M = 1000$

states kept. The system size analysis of the ladder results is consistent with the findings for chains, namely the acoustic mode has size dependence, while the optical mode does not. In summary, while we are confident that our results for ladders capture the essence of the problem, including the existence of acoustic and optical bands and quite different weights in different portions of the Brillouin zone, only further (very demanding) work can achieve the same accuracy as shown here for chains.

D.3 Magnetic moment evolution.

In Fig. 12 we present the evolution of the local magnetic moment $\langle S^2 \rangle$ within the block-orbital selective Mott phase. This local moment can be obtained from the sum-rules of spin-spin correlation functions, i.e.,

$$S(q) = \frac{1}{\pi} \int \mathrm{d}\omega \, S(q,\omega) \,, \quad \langle S^2 \rangle = \frac{1}{L} \int \mathrm{d}q \, S(q) \,. \tag{20}$$

Note that the above equations allow to relate the total spectral weight of INS data with the value of the local spin via $\langle S^2 \rangle = S(S+1)$. The results presented in Fig. 12 are obtained from the integration of the static structure factor $S(q)$. As clearly visible, the magnetic moments start to develop already in the paramagnetic (metallic) phase [5] and are stabilized to its maximal value $\langle S^2 \rangle$ ($S = 1$ for $\overline{n} = 4/3$) in the middle of the block-OSMP.

D.4 Comparison of DMRG results with powder experiment.

Although $BaFe_2Se_3$ is a quasi-1D compound, the finite ω-dependent properties should be dominated by the 1D nature of the ladder lattice (while, e.g., d.c. transport is more subtle). It is therefore appropriate to directly compare our dynamical SSF to experimental findings. Since the latter is obtained using a powder sample, our results presented in Fig. 5.2 have to be averaged over all spherical angles [184]. Furthermore, to qualitatively compare to the inelastic neutron scattering (INS) data we must incorporate in the analysis the momentum

dependent magnetic form factors $F(Q)$ of the spin carriers, namely the Fe^{2+} ions. Here we assume a gyromagnetic ratio $g = 2$ (spin-only scattering). The functional form of the former can be taken from crystallography tables [6]. In Fig. 13(a) we present the powder average of our spectra. Several interesting general features can be inferred: (i) using realistic values [4] for the Fe-Fe distance such as 2.7 Å, remarkably we obtain a nearly perfect agreement for the position of the acoustic mode. The leading INS signal is centered at $Q \simeq 0.7$ (1/Å), followed by peaks at 1.8 (1/Å) to 2.5 (1/Å) with smaller intensity [indicated by vertical red arrows in Fig. 13(b)]. (ii) The neutron spectrum gives three flat (momentum-independent) bands of spin exactions: two of them are centered approximately at $\omega \sim 0.1$ eV ($\omega_1 = 0.0889$ eV and $\omega_2 = 0.1082$ eV, depicted as horizontal red arrows in Fig. 13(b)), while the third one is positioned at $\omega_3 = 0.198$ eV. Our 1D results yield only one optical mode centered at $\omega \simeq 0.105$ eV in accord with the most pronounced peak within the INS spectrum. This qualitative agreement indicates that our model is able to capture the nontrivial nature of the frustrated magnetism of $BaFe_2Se_3$, and that the studied parameter range of our Hamiltonian is valid for the whole 123 family.

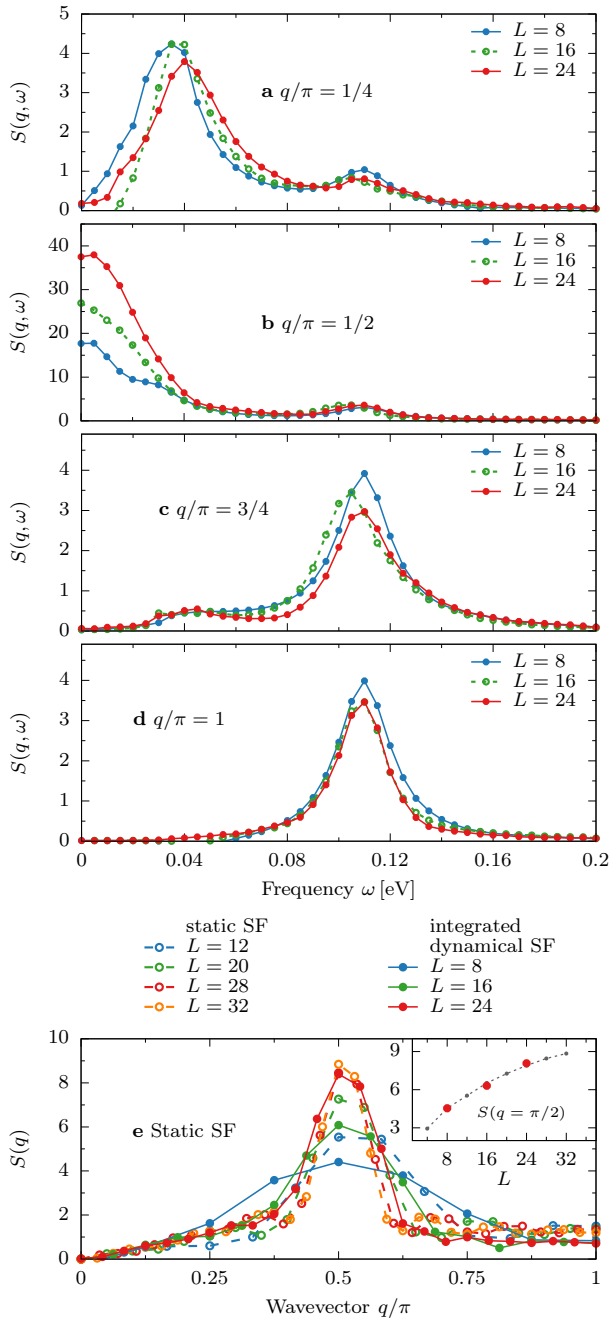

Figure 10: Finite-size analysis. (a-d) Size L dependence of the frequency-resolved dynamical SSF for $q/\pi = 1/4, 1/2, 3/4, 1$, as calculated with $\eta/\delta\omega = 2$ and $M = 800$. (e) L-dependence of the static SSF. Open points represent the results obtained as the expectation value of the GS, while solid points are obtained from the integral over the frequency (see Chapter 5 for details). Inset illustrates the quasi-long-range nature of block $\pi/2$ ordering, with a signal intensity growing with L.

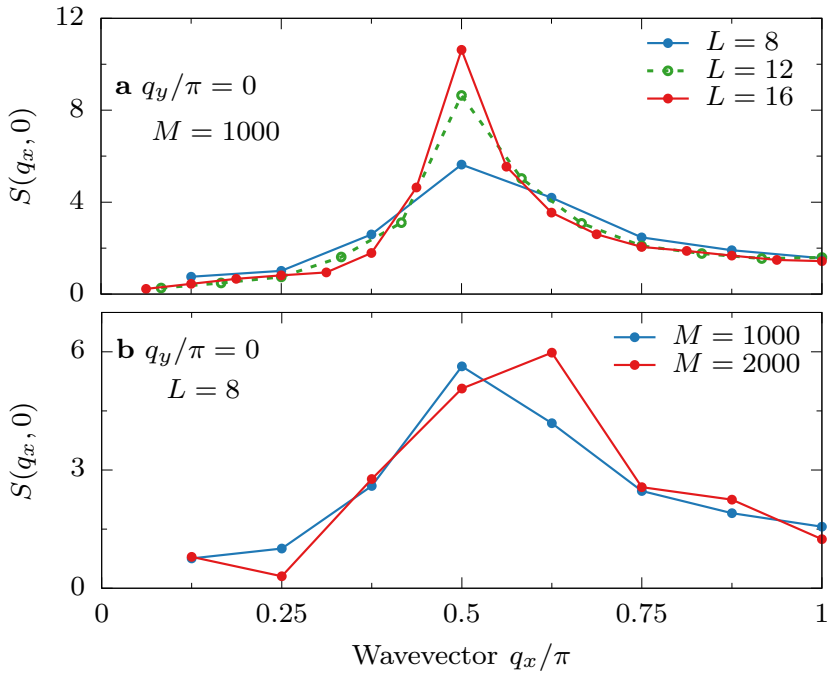

Figure 11: Ladder geometry analysis. (a) Finite size L and (b) number of states kept M scaling of the static SSF in the bonding sector, $q_y/\pi = 0$.

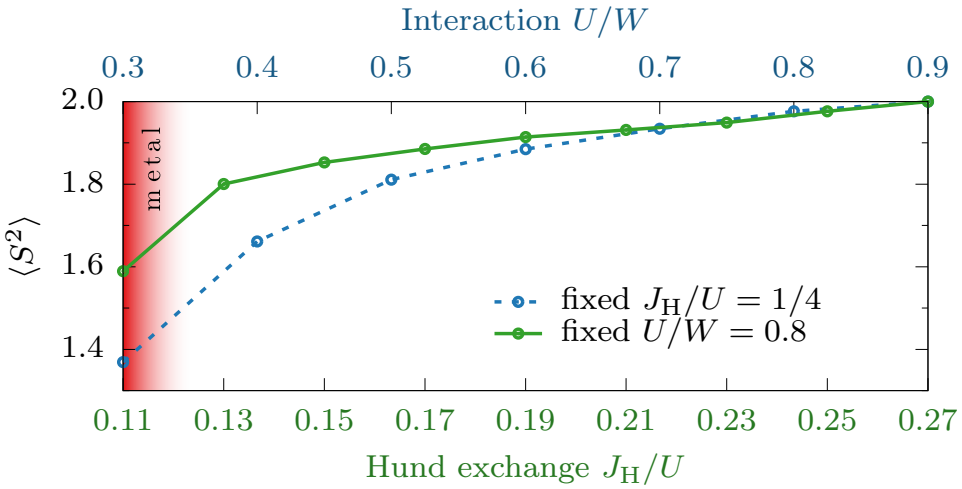

Figure 12: Magnetic moment. Evolution of the local magnetic moment $\langle S^2 \rangle$ within the block-OSMP. The solid line (lower x-axis) represents results for fixed value of interaction $U/W = 0.8$ and various value of J_H/U. The dashed line (upper x-axis) represents results at fixed $J_H/U = 1/4$ and for various values of U/W. The results were obtained using a DMRG method with parameters $L = 16$ (48 orbitals), $M = 800$.

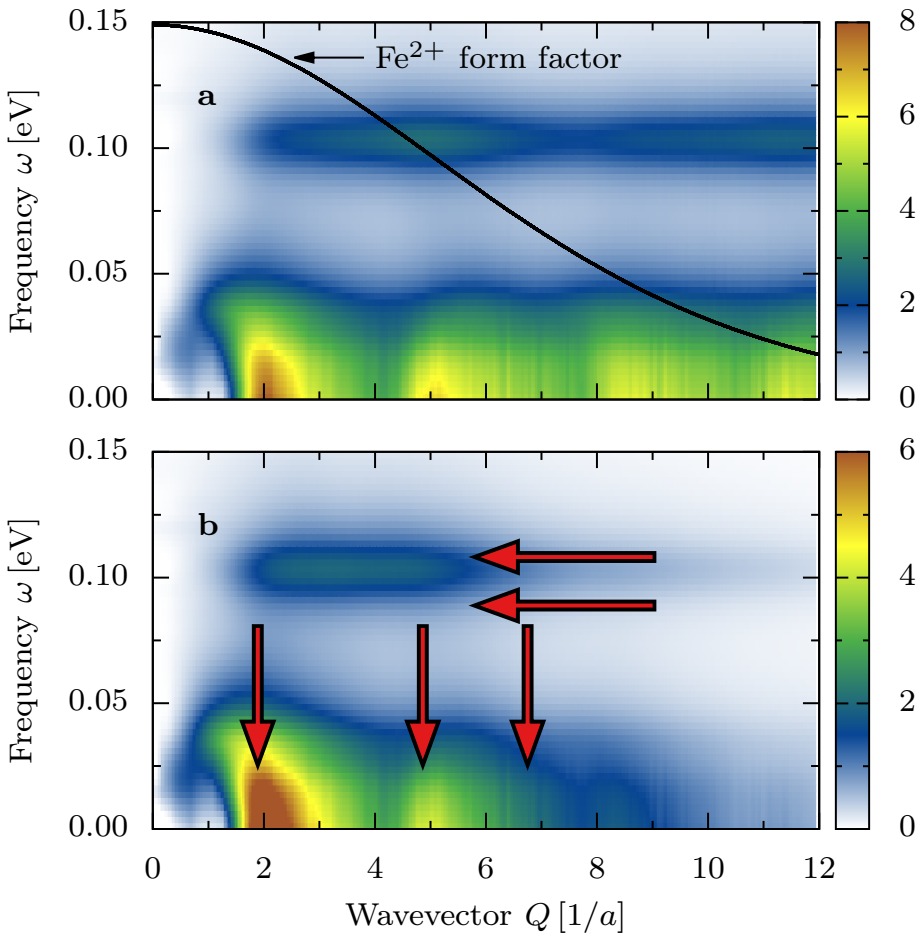

Figure 13: Powder spectrum. (a) Spherical average of the dynamical SSF. The black solid line represents the magnetic form factor $F(Q)^2$ of the Fe^{2+} ions [6]. (b) Spherical average of the dynamical SSF convoluted with the form factor $F(q)$ relevant for a direct comparison with the $BaFe_2Se_3$ INS results [4]. Red arrows indicate the position of maximum intensities in the INS spectrum. See text for details.

Vita

Nitin Kaushal was born in Ambala, India, to parents Ram Kumar Kaushal and Anita Kaushal. As an undergraduate student, he attended the Indian Institute of Science Education and Research Kolkata (IISER-K) from 2008 to 2013, where he earned a Bachelors and Masters dual degree in Physics. After graduation, Nitn Kaushal was accepted to the Doctoral program at the University of Tennessee in Knoxville, Tennessee. While a graduate student, he worked as a Graduate Research Assisteant for Prof. Elbio Dagotto. During this time, he focused on the numerical studies of multi-orbital Hubbard models using density matrix renormalization group, Lanczos, and mean field theory techniques. In his graduate research time, he published fifteen publications and presented talks in three APS march meetings. He defended his Ph.D in July 2020, and is scheduled to move to Oak Ridge National Laboratoty in Fall 2020 to continue his scientific career as Postdoctoral Research Associate.